SUPPRESSION OF THE TOROIDAL DRIFT AND OTHER ASPECTS OF THE POLYTRON PLASMA CONTAINMENT DEVICE

by

Hernan Humberto Chuaqui

This thesis is submitted in partial fulfilment
of the requirements for the Degree of Doctor
of Philosophy in the University of London

1978

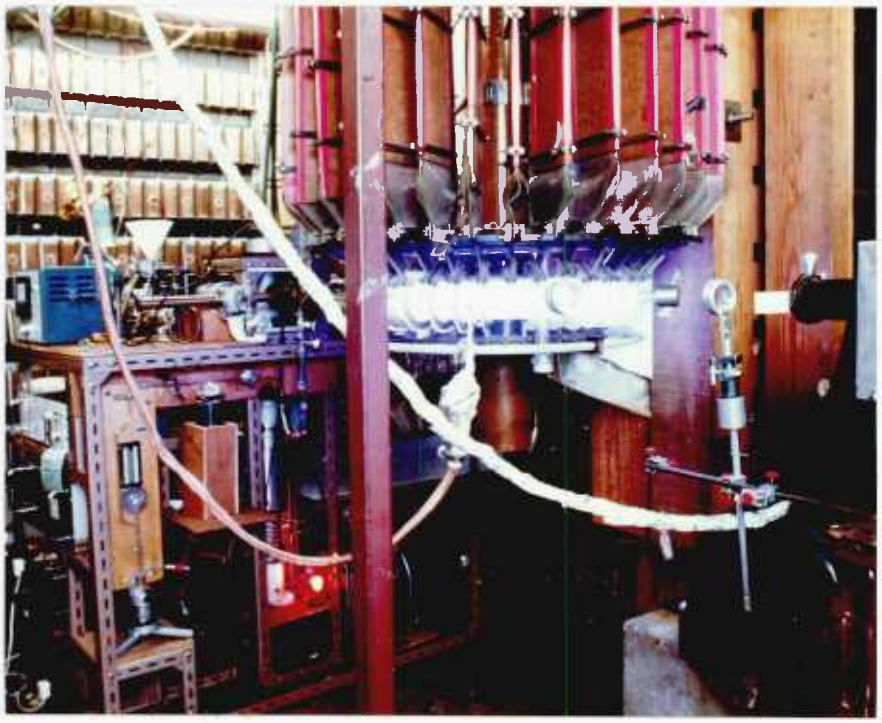

THE POLYTRON

To Ana Maria

ABSTRACT

It is well known that plasma in a cusp magnetic field is stable. However, the containment time is seriously limited by plasma leakage through the ring cusp. In the Polytron this could be suppressed in principle by giving the plasma a centre of mass motion through multiple cusps around a toroidal axis.

Earlier experiments showed that the plasma containment in the Polytron is limited by an overall outward motion of the plasma. In the present work it is shown that this motion can be controlled by applying a vertical magnetic field. This allows the plasma to attain a centre of mass velocity higher than the mean ion thermal velocity, this being an essential condition to be met in order to reduce losses through the ring cusp. This loss has been investigated and results indicate that there is a large initial loss, arising from regions of uncontained particles, becoming small at later times, as expected from centre of mass velocity measurements.

To obtain complete control of the plasma column position we would require a vertical magnetic field capable of changing at the same rate as the plasma current.

Possible ways of suppressing the initial loss of plasma through the ring cusp are discussed.

CONTENTS

cont/

A NOTE ON UNITS

Except where stated rationalized mks units are used. Exceptions to this rule are plasma temperature and filling pressure, which are given in eV and mTorr respectively.

A NOTE ON COORDINATE SYSTEMS

Cylindrical or toroidal coordinates are used. Cylindrical coordinates are r, θ or ϕ and z. Toroidal coordinates are r, ϕ, θ.

Said the Eye one day, "I see beyond these valleys a mountain veiled with blue mist. Is it not beautiful?"

The Ear listened, and after listening intently awhile, said, "But where is any mountain? I do not hear it."

Then the Hand spoke and said, "I am trying in vain to feel it or touch it, and I can find no mountain."

And the Nose said, "There is no mountain, I cannot smell it."

Then the Eye turned the other way, and they all began to talk together about the Eye's strange delusion. And they said, "Something must be the matter with the Eye."

from "The Madman: His Parables and Poems"
by Kahlil Gibran

Chapter 1

INTRODUCTION

The Polytron is a plasma containment device proposed by Haines (1961) as a possible controlled thermonuclear arrangement. Basically it is a toroidal multiple magnetic cusp device in which plasma containment and heating is achieved by Hall acceleration in the toroidal direction. In this thesis successful operation of the Polytron as a containment device is demonstrated for the first time (in argon). It is further shown that a modification of the magnetic cusp geometry would reduce plasma losses, particularly initial losses, and allow operation in deuterium, thus increasing the potential of the Polytron as a controlled nuclear fusion device.

In the present chapter the Polytron is considered in the context of controlled nuclear fusion research. Its basic concept and criteria for operation are given. A summary of earlier work and the author's contribution is presented. A brief description of the apparatus is given. Finally the organisation of this thesis is described.

1.1 The Polytron as a controlled nuclear fusion device

There are two basic conditions which have to be satisfied in order to achieve controlled nuclear fusion: the plasma temperature has to be higher than 10 keV for D-T reaction and the so-called Lawson criterion has to be fulfilled, i.e. the product $n\tau$ of plasma number density n and containment time τ has to exceed 10^{14} cm^{-3} s.

There are two ways in which the required conditions can, in principle, be met: inertial and magnetic confinement. The Polytron is a magnetic confinement device in which inertial effects are essential to reduce plasma losses.

1.1.1 Inertial confinement

In inertial confinement systems a small pellet of D-T fuel is rapidly heated and compressed to temperature and density at which fusion occurs. Laser, electron or ion beams and fast rising magnetic fields

can be used to achieve the required compression. The expansion of the compressed plasma is determined by ion inertia and the plasma potentials (of the order of the electron temperature) available to accelerate the ions. As the plasma expands the Lawson criterion is no longer satisfied. Times under 10^{-10} sec and densities $\sim 10^{23}$ cm^{-3} are typical for current experiments.

1.1.2 Magnetic confinement

There are two types of magnetic confinement devices: closed and open magnetic surfaces. The two types can be further subdivided into stationary and flow type devices, depending on whether the centre of mass velocity of the plasma is smaller or larger than the ion thermal velocity.

1.1.2.1 Closed magnetic field systems

In this class the more important types are tokamaks, stellarators and toroidal diffuse pinches. Tokamaks appear very promising, a substantial effort being dedicated to them. Confinement times have been improved to 50 ms with an $n\tau$ product of 10^{13} cm^{-3} s. It is expected that the next generation of tokamaks (JET, TFTR, T20) will achieve scientific break-even, i.e. as much energy produced by fusion as is fed into the plasma. For "two-component" tokamaks in which a tritium beam is injected into the tokamak filled with a stationary deuterium plasma, the required $n\tau$ product is an order of magnitude smaller than for a stationary tokamak (Furth, 1975).

Recent stellarator experiments (Miyamoto, 1978) have shown that it is possible, with ohmic heating, to reach the same plasma parameters as in tokamaks. Temperatures around 1 keV and $n\tau$ values of 5×10^{11} cm^{-3} s have been obtained.

Toroidal pinch experiments have achieved temperatures of around 2 keV and $n\tau$ values of 10^{12} cm^{-3} s (Bobeldijk et al., 1977). All the experiments of this type are of relatively small size where plasma-wall interaction plays a dominant role.

A recent proposal by Rostoker (1977) describes a closed magnetic field experiment in which plasma flow plays an important role. The proposed device is a multiple magnetic mirror arranged as a torus. A toroidal electric field accelerates ions, while electrons (except those

in the loss cones) are trapped in the mirror fields. Ion acceleration is by Hall effect, as in the Polytron. Eventually accelerated ions will be extracted for use in a compression experiment.

1.1.2.2 Open magnetic field systems

Open systems are generally simpler than closed systems. Their main disadvantage is the loss of plasma and energy through the magnetic field openings. However, plasma loss can be used for efficient direct conversion of plasma energy to electricity (Post, 1969).

Magnetic mirror machines are open magnetic field devices on which considerable interest is centred. The production of a stable, hot plasma (10-20 keV) with densities of up to 10^{14} cm^{-3} for times of 2 ms has been reported (Coensgen et al., 1976). However, plasma losses and particularly energy losses by electron thermal conduction through the ends are too high for a fusion reactor. Nevertheless calculations indicate that this problem may be overcome in the tandem geometry now under construction at Livermore.

Linear flow reactors have been proposed by Morozov (1968), where plasma flow heats and compresses a small volume to thermonuclear conditions.

Linear accelerators, used to produce ion or neutral beams to heat contained plasmas, are widely used. Amongst these Hall accelerators (Morozov et al., 1968; Cole, 1970; Lomas, 1975) are of special interest to us, as they are closely related to the Polytron. Large current ion beams can be obtained. The beams generated have a large divergence, which limits their applicability as beam injection devices. An interesting new development is Pulselac (Humphries, 1977), a linear multistage ion accelerator. Different stages, which consist of an annular drift tube, are separated by a gap with a radial magnetic field. The radial magnetic field allows a strong accelerating field without electron flow. Pulsed lines are to be used to provide the accelerating voltage. Effective acceleration and focussing of an annular ion beam of energy of 300 MeV appears feasible. The device is envisaged as a source of ions for pellet compression.

Amongst other open devices like linear pinches, solenoidal systems and plasma focus, the latter one has the highest $n\tau$ value (10^{12} cm^{-3} s with $T_e \simeq T_i \simeq 1\text{-}3$ keV, and $n = 10^{20}$ cm^{-3}).

The Polytron is an open magnetic field device. Its toroidicity and ion flow should make plasma losses negligible. The main advantages of the Polytron compared to most closed magnetic field devices are the following:

a) Cusp magnetic field geometry has absolute MHD stability.

b) Ion heating is mainly viscous in the Polytron, and therefore increases with ion temperature. In closed magnetic field devices, such as tokamaks, heating is ohmic. Thus it is essential in these devices to provide additional heating. The usual scheme used in present day experiments is neutral beam injection.

c) In the Polytron ions in the ring cusp region are preferentially accelerated. These accelerated ions will flow past a background of stationary ions. The minimum $n\tau$ value should therefore be smaller than 10^{14} cm^{-3} s, as is the case in two-component tokamaks. In the present Polytron the $n\tau$ value of about 10^{9} cm^{-3} s is limited by wall effects.

1.2 The Polytron concept and criteria for Polytron action to occur

For a plasma containment device to be suitable for fusion the following conditions have to be met:

i) The configuration has to be stable for times longer than the minimum time derived from Lawson's criterion. The density is determined by criteria that depend on the particular configuration employed.

ii) Losses have to be a small fraction of the contained plasma during this time.

iii) Ion temperature has to be high enough, so an adequate fusion reaction rate is established.

It is a well known fact that a cusp magnetic field geometry has absolute magnetohydrodynamic stability (Berkowitz et al., 1958). However, large losses occur through the point and ring cusps. The Polytron is a configuration proposed to eliminate these losses. It is a multiple magnetic cusp device, cusps being joined end-to-end into a toroidal

configuration. Ions are accelerated by means of a toroidally induced electric field to velocities much higher than their thermal velocity, thus reducing losses through the ring cusps. Plasma heating is due to resistivity and viscosity. Ion acceleration is due to Hall effect. Thus the Polytron is a toroidal Hall accelerator. However, unlike linear Hall accelerators (Morozov et al., 1969; Cole, 1970; Lomas, 1975) no iron core is present. This facilitates the study of the acceleration mechanism and the plasma.

Haines's proposal was first put forward at the 1961 Salzburg Fusion Conference and again at the 1963 Paris Ionized Gases Conference. An Imperial College report (Haines, 1962) gives a detailed account of the proposal. A review on cusp magnetic field devices recently published (Haines, 1977) gives an account of the present situation and discusses their possible application as fusion devices.

To obtain Polytron action, the following must hold:

(i) The Hall parameter, $\omega\tau$, for electrons must satisfy

$$\omega\tau = \frac{\sigma B_r}{n_e e} > 1 \qquad 1.1$$

where ω is the electron cyclotron frequency, τ the electron-electron collision time, σ the conductivity, B_r the radial magnetic field and n_e the electron density. This condition, obtained from Ohm's law (Haines, 1962), ensures that Hall current flows. In the present device, this condition holds everywhere except near the magnetic axis.

(ii) The ion Larmor radius a_L has to be

$$a_L = \frac{E}{\overline{B}\omega_{ci}} \geqslant \frac{L}{2} \qquad 1.2$$

where L is the cusp separation and $\overline{B}$ the average value of the radial cusp magnetic field. This condition is derived assuming a uniform electric field (Haines, 1962). If 1.2 does not hold, ions will not be able to move from one cusp to the next. In the present device it holds for argon ions but not for hydrogen. This is why the experimental results presented are for argon only.

For electrons inequality 1.2 should be reversed, so they are tied

to the magnetic field lines. This is easily satisfied except near the magnetic axis.

$$\text{(iii)} \quad \mu_o ne \frac{E}{\bar{B}^2} < \frac{2}{L} \qquad 1.3$$

This condition is obtained by requiring that the magnetic field produced by the Hall current $\frac{L}{2}\frac{\mu_o neE}{\bar{B}}$ is smaller than the cusp magnetic field, $\bar{B}$ (Dunnett, 1968). Condition 1.3 applies for all the parameters used in the present experiment.

In order to satisfy Equations 1.2 and 1.3 simultaneously it is necessary for the ion collisionless skin depth $\lambda_i = c/\omega_{pi}$ to be larger than L/2.

Conditions (i) to (iii) are believed to be necessary for Polytron action to occur. The following criteria assume that conditions (i) to (iii) hold.

(iv) For no plasma leakage through ring cusp, the toroidal ion velocity v_ϕ must satisfy

$$v_\phi^2 >> \frac{2kT_i}{m_i} \qquad 1.4$$

where T_i is the ion temperature, m_i is the ion mass and k is Boltzmann constant.

(v) To avoid excitation of two stream instability by the accelerated ions the toroidal ion velocity must satisfy

$$v_\phi^2 << \frac{2kT_e}{m_e} \qquad 1.5$$

where T_e is the electron temperature and m_e is the electron mass. Equations 1.4 and 1.5 have been derived by Haines (1962). They can be easily satisfied simultaneously due to the large difference in mass between ions and electrons.

In the experiment Equation 1.5 certainly holds whereas 1.4 holds provided the inequality is read as larger than instead of very much larger.

(vi) $B_\theta << \bar{B}$ 1.6

where B_θ is the plasma poloidal field. This is to ensure MHD stability (Haines, 1962), and holds for all the conditions studied.

(vii) $\mu_o I_\phi^2 < 8\pi Nk(T_e + T_i)$ 1.7

where I_ϕ is the total plasma current and N is the line density. If 1.7 does not apply the discharge pinches (Bennett relation). For cusp bank charging voltages of .75 kV and higher 1.7 does apply, whereas it does not with no cusp field present, a toroidal pinch being obtained.

Haines (1962) assumed a steady state regime, with $T_e = T_i = T$, in which the toroidal velocity and current are given by

$$v_\phi^2 = \frac{2kT}{(m_e m_i)^{\frac{1}{2}}} \quad , \quad I_\phi = eNv_\phi \qquad 1.8$$

Combining 1.7 and 1.8 gives an upper limit for the line density

$$N < \frac{8\pi(m_e m_i)^{\frac{1}{2}}}{\mu_o e^2} \qquad 1.9$$

For deuterium and argon the limiting N is 4.3×10^{16} m^{-1} and 1.9×10^{17} m^{-1}.

1.3 Summary of earlier work on the Polytron

As already mentioned, the original scheme was proposed by Haines in 1961.

An experiment was set up and initial results can be found in Dangor et al. (1968) with a more detailed account in G J Parkinson's PhD thesis (1968).

Dunnett (1968) extended the MHD calculation to include the effect of the poloidal plasma current, showing that the acceleration mechanism becomes ineffective if the plasma magnetic field becomes comparable with the applied cusp field (Equation 1.4).

Kilkenny (1972) developed the MHD model further and performed a single

particle calculation. This calculation showed that the plasma can be subdivided in two distinct volumes from which contained and uncontained particles originate and that the applied electric field is localized in sheaths in the ring cusp regions. His experimental results show that there is an initial accelerating phase, followed by a plasma loss. An overall outward plasma displacement was also observed, the plasma hitting the outer wall and cooling down.

Watkins (1974) studied the acceleration phase by using a two-dimensional, two fluid computer code. He found that whistler waves seriously limited the time for which the calculation can be performed.

Kilkenny (1976) developed an MHD model including collisional effects to study the formation of the sheath in the ring cusp where the electric field is large.

At present, Brown (1978) is developing a magneto-fluid-dynamic model of a steady state Polytron. A perfectly conducting incompressible fluid is assumed.

1.4 The author's contribution

The objectives of the present work were

(a) To study in a direct way the sheath region at the ring cusp where most of the electric field is localized. This is important as the actual electric field in the sheath region determines the ion Larmor radius, and hence the condition (Equation 1.2) for ion acceleration. A narrower sheath region gives a higher electric field. Thus it becomes possible to satisfy Equation 1.3 with a lower ion mass.

A second aspect to be studied was the possible presence of waves in the sheath region. Electrons have large $\underline{E} \times \underline{B}$ drift velocities in the sheath region in view of the large toroidal electric field and radial magnetic field. Thus if the drift velocity v_D satisfies

$$c_s < v_D < v_{T_e}$$

with $T_e \simeq T_i$, where c_s is the ion sound speed and v_{T_e} the electron thermal speed, which are the normal conditions obtained in the Polytron,

drift and electron cyclotron drift instabilities are likely to occur. Also modified two-stream instability excited by runaway electrons might be present.

(b) To investigate the possibility of preventing the outward horizontal plasma displacement (along major radii) by means of a vertical magnetic field (parallel to major axis).

The first objective has been partially fulfilled and a sheath structure was observed. The electric field in the sheath is found to be larger than the average applied electric field by a factor of 6. No waves within the passband of the measuring system used (12 MHz) have been detected. Thus electron cyclotron drift and drift instabilities are ruled out. The question of higher frequency instabilities remains open.

The second objective has been wholly achieved. It has been shown that the plasma position can be effectively controlled by a vertical magnetic field.

The effect of varying the magnitude of the cusp magnetic field on plasma position has been shown to be small, presumably due to a large electron current. The cusp magnetic fields should act as magnetic lenses, as shown in single particle calculations. This effect is significant when most of the current is carried by ions.

Plasma acceleration is shown to persist for several microseconds, but is then suppressed. This occurs due to the interaction of the wall with the uncontained plasma and the arrival of wall material in the contained plasma region. Ion heating is mainly viscous whereas electron heating is ohmic. Plasma flow is shown to be supersonic although not highly so, as required by Equation 1.4. Nevertheless plasma losses after the initial loss from regions of uncontained particles are found to be small. Up to 95% of the energy supplied to the plasma is lost through heat conduction.

Means of preventing the plasma-wall interaction effect are discussed. In particular a modification of the cusp magnetic field structure is proposed which appears to be very effective in eliminating the plasma losses. An increased Mach number is shown to decrease heat losses.

1.5 A brief description of the apparatus

A detailed description of the device has been given by Parkinson (1968) and in its modified form by Kilkenny (1972). The only change of significance introduced by the author is the modification of the induction rod system to obtain a vertical magnetic field. This will be discussed later.

Fig. 1.1 shows a schematic diagram of the device. Also shown is a time integrated photograph from underneath of the device in operation, where the different components can be identified. The device consists of:

i) A toroidal quartz vessel, major radius 25.4 cm, minor radius 3.6 cm, with several ports for pumping and diagnostics.

ii) A vacuum pumping system (not shown), consisting of a two-stage rotary pump and a mercury diffusion pump with a liquid nitrogen trap. Base pressure is between 1×10^{-6} to 1×10^{-5} Torr, depending on probes or other diagnostics in use.

iii) A set of 36 single turn cusp coils. The cusp magnetic fields are generated by discharing separate capacitors banks of 216 μF, 3.5 kV through each of 24 neighbouring coils. The remaining coils are fed in two groups from sixfold capacitor banks.

iv) A set of from 4 to 8 induction rods through which the main capacitor bank is discharged to induce an accelerating electric field around the torus. The plasma is the secondary of an air core transformer, the induction rods being the primary. The modified induction rod assembly which will be discussed in Chapter 3 also provides the vertical magnetic field.

v) A main capacitor bank, 60 μF, 30 kV, period between 24 and 33 μs, depending on the number and distribution of induction rods.

vi) A preionizing capacitor bank, 2 μF, 20 kV, period 6 μs. The spark gaps are set in such a way that the firing of the preionizer does not trigger the main bank.

The average radial magnetic field in the plasma region produced by the cusp coil system at the ring cusp plane is

$$\overline{B}_r = 1.0\ V_c \quad \text{gauss} \qquad 1.10$$

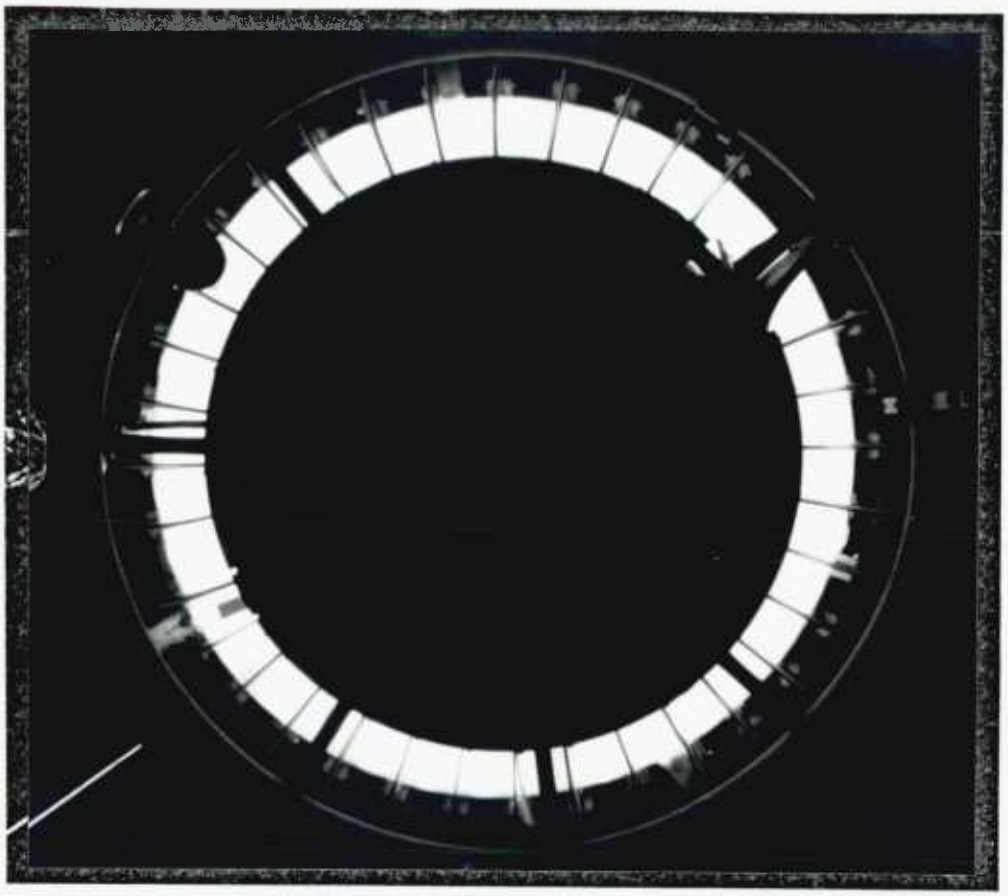

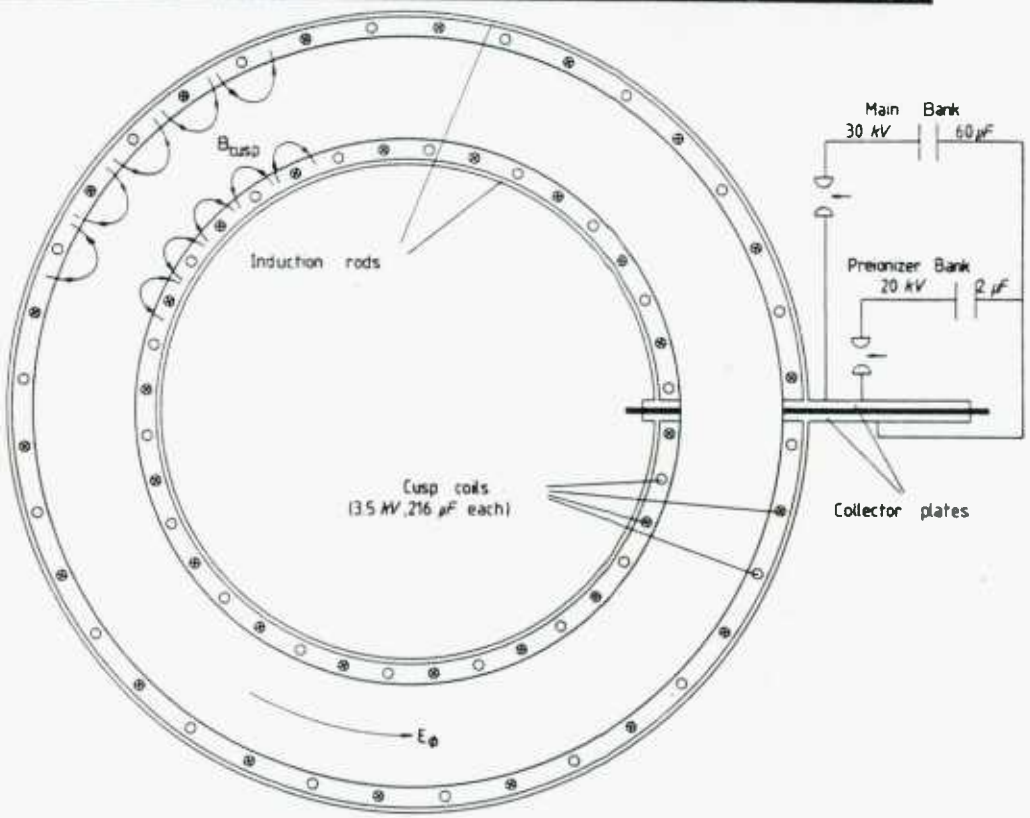

Fig. 1.1 Schematic diagram and time integrated photograph of the Polytron. In the photograph pumping and diagnostics ports and part of the vacuum vessel, induction rods and cusp coils can be seen.

where V_c is the cusp bank charging voltage in volts.

The average axial field in a coil plane is given by

$$\overline{B}_\phi = 1.8\ V_c \quad \text{gauss} \qquad 1.11$$

The values given are for individually fed coils; they are 25% less for grouped cusp coils.

The main bank voltage (V_m) induces an electric field of between 0.5 and 0.6 of the charging voltage at the plasma position.

$$E_\phi = 0.6\ V_m \quad \text{V/m} \qquad 1.12$$

Fig. 1.2 shows the timing sequence for the different capacitor banks. The first to be fired is the preionizer bank and when its discharge current has decayed the cusp banks are fired. The main bank is fired when the cusp magnetic field has reached two thirds of its peak value.

1.6 Structure of the thesis

In Chapter 2 the formation of a double electric sheath is discussed. Results of direct measurements on this sheath with double electric probes are presented. The presence of a high positive plasma potential is investigated with single electric probes and is ascribed to loss of runaway electrons.

In Chapter 3 radial forces produced by the self magnetic field and the externally applied magnetic field are considered. The diagnostic techniques used to assess the effect of these forces are described.

In Chapter 4 the results obtained with the diagnostic techniques described in Chapter 3 are presented.

In Chapter 5 the experimental results presented in Chapter 4 are analysed. The analysis shows that the present device operates in the 'Polytron regime', until gas and impurities from the wall reach the core of the plasma.

In Chapter 6, the final chapter, means of suppressing initial losses

are discussed. A modified cusp magnetic field geometry in which no losses are present is proposed. Heat losses are shown to be strongly dependent on Mach number and can therefore be made negligible for high enough Mach numbers.

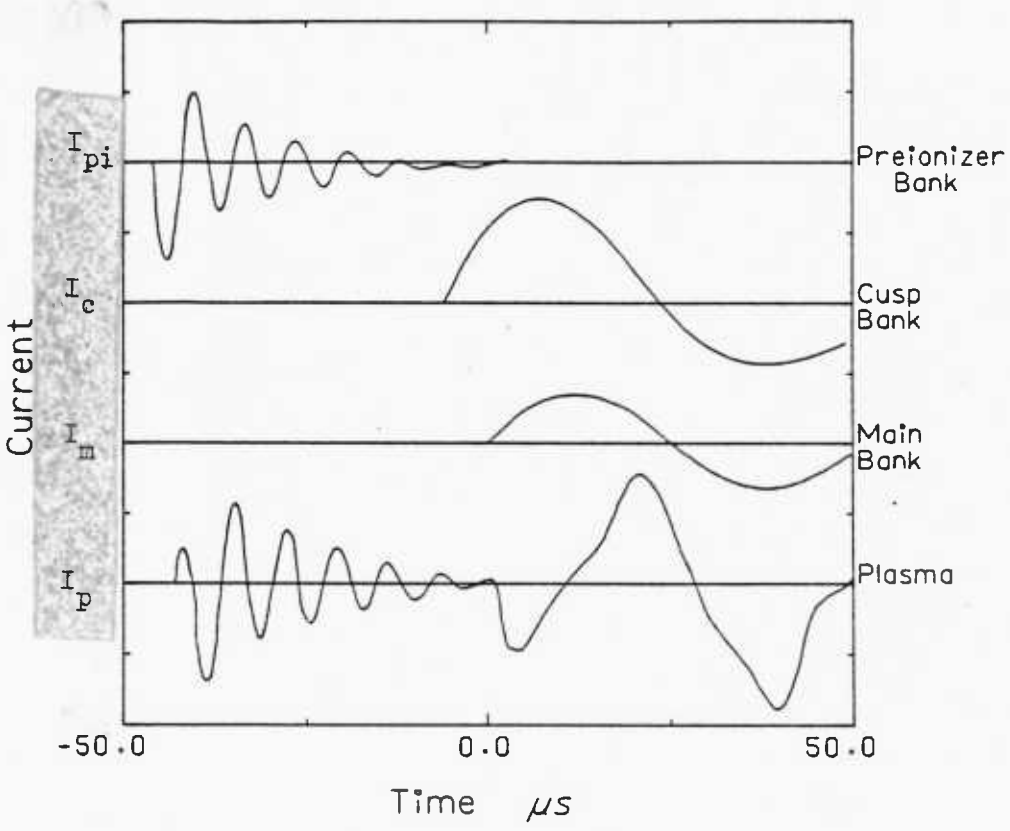

Fig. 1.2 Typical timing sequence. The different peak currents are: $I_m \simeq 100$ kA; $I_c \simeq 45$ kA; $I_{pi} \simeq 25$ kA; $I_p \simeq 10$ kA.

Chapter 2

PLASMA SHEATHS IN THE POLYTRON

2.1 Plasma sheaths

Two types of sheaths occur in plasmas: the ones occurring at the interface between a plasma and a wall or electrode and the sheaths formed in the body of a plasma. The latter type is usually referred to in the literature as "double sheaths". In plasma-wall sheaths a single space charge layer develops, whereas in a double sheath a more complicated structure is present.

There are two types of double sheaths. The first type is formed due to conditions of plasma flow. Examples of this type are the double sheaths described by Carlqvist and Jacobsen (1964) and by Andrews and Allen (1971). In the first example a double sheath is postulated to explain the presence of high energy particles associated with solar flares. In the second example, Andrews and Allen have shown that in a discharge tube with a constriction a double sheath develops to maintain quasi-neutrality and ensure current continuity.

The second type is due to the presence of a magnetic separatrix (Kilkenny, 1976). Magnetic separatrices occur in several plasma devices such as stellarators (Miyamoto, 1978), Hall accelerators and cusp containment devices, in particular in the Polytron. The magnetic field lines for a linear polytron are shown in Fig. 2.1. The magnetic separatrices are indicated by dotted lines.

An electrical double sheath will develop in the separatrix region if the Hall parameter is large and the plasma potential on the two sides of the separatrix is different. For large values of Hall parameter, electron resistivity across magnetic field lines is very much larger than parallel to the lines. In the limit of perfect conductivity magnetic field lines lie in equipotential surfaces (Morozov et al., 1968; Kilkenny et al., 1973). Electric fields will therefore be present only in the separatrix region.

This situation arises in the Polytron. Separatrices are present in the ring cusp regions. The electric field should appear only in

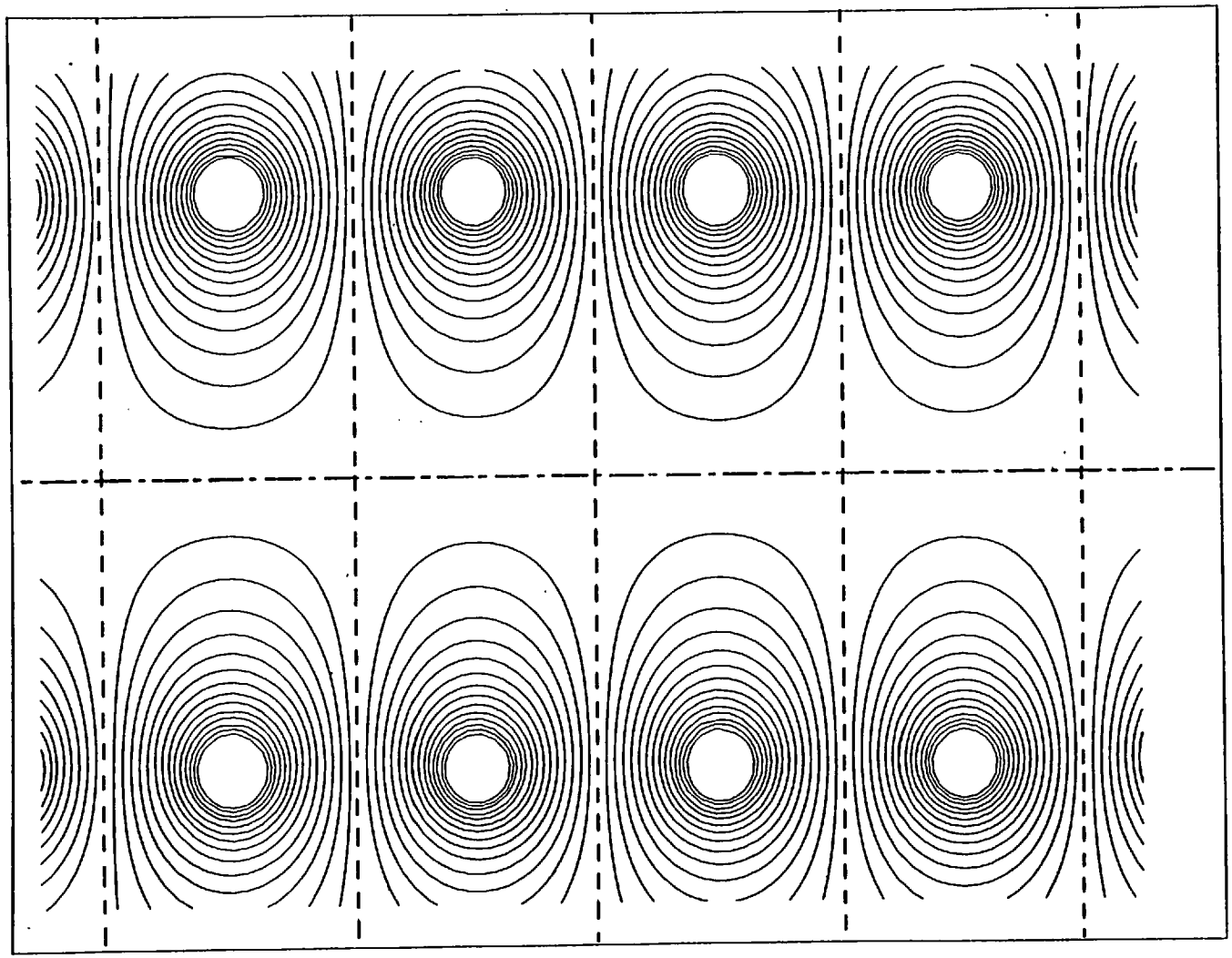

Fig. 2.1 Cusp magnetic field lines. Separatrices are shown by dashed lines.

this region. If there are no collisions present the voltage drop should occur over a distance of twice the electron Larmor radius. For this limiting case, the sheath thickness t_s is

$$\frac{t_s}{2} \geq \frac{E}{B\omega_{ce}} = \frac{U}{t_s}\frac{m}{eB^2} \qquad 2.1$$

$$\therefore \quad t_s \geq \left(\frac{2mU}{eB^2}\right)^{\frac{1}{2}} \qquad 2.2$$

where U is the applied voltage per cusp, m the electron mass, ω_{ce} the electron cyclotron frequency and B the magnetic field.

For the experimental conditions in the Polytron (U~400V, $n \sim 10^{21} m^{-3}$, B~0.2T) the thickness obtained from Equation 2.2 is ~0.5 mm. A sheath thickness was inferred by Kilkenny (1972) from a description of the plasma as an electric circuit. At time t = 0 we have

$$U = L_H \frac{dI_\phi}{dt} = \frac{t_s m_i}{e^2 Z^2 nA}\frac{dI_\phi}{dt} \qquad 2.3$$

where L_H is the Hall inductance, Z the charge number, n the ion density, A the cross-sectional area of the plasma and m_i the ion mass. For the present experimental conditions Kilkenny obtained from Equation 2.3 a sheath thickness of $1.6 \pm .5$ mm, much larger than the value obtained from Equation 2.2.

2.2 Resistive sheath in the Polytron

The discrepancy between experimentally inferred and collisionless sheath thickness values prompted Kilkenny (1976) to develop an MHD calculation including collisions. In this model cylindrical coordinates are used and fixed magnetic field lines in the (r,z) plane are considered.

$$B_r = B_o I_1(kr) \sin kz, \quad B_\theta = 0, \quad B_z = B_o I_o(kr) \cos kz \qquad 2.4$$

where $k = \pi/L$, L is the cusp separation, I_o and I_1 are modified Bessel functions.

Using Ohm's and Faraday's laws

$$\frac{\partial B_\theta}{\partial t} = -(\nabla \times \underline{E})_\theta = -\left[\nabla \times (\underline{j}/\sigma - \underline{v} \times \underline{B} + \underline{j} \times \underline{B}/ne)\right]_\theta \qquad 2.5$$

After a sufficiently long time, longer than the resistive diffusion time, $\frac{\partial B_\theta}{\partial t} = 0$.

In the Polytron a modified resistive diffusion time is obtained from Maxwell equations, Ohm's law and equation of motion (Kilkenny, 1972) given by

$$\tau_d \sim r_b^2 \sigma \mu_o / \omega\tau \qquad 2.6$$

where r_b is the plasma vessel's radius and σ the conductivity.

After this modified diffusion time there is a long period when $|\underline{v}| << |\underline{j}|/ne$, before appreciable plasma acceleration occurs. The θ component of Faraday's law then simplifies to

$$\left[\nabla \times (\underline{j} + \sigma \underline{j} \times \underline{B}/ne)\right]_\theta = 0 \qquad 2.7$$

This and the azimuthal component of Ohm's law reduce to a second order homogeneous partial differential equation which has been integrated.

The results obtained by Kilkenny are formulated in terms of $\omega_o\tau$, the Hall parameter at the centre of a coil ($r = 0$, $z = 0$). When $\omega_o\tau << 1$, the magnetic field has little effect and the current flows uniformly over the discharge cross section. As $\omega_o\tau$ is increased the current tends to follow the magnetic field lines, except at the ring cusp separatrix. A large electric field is needed to drive the current across magnetic field lines in this region. Fig. 2.2 is reproduced from Kilkenny (1976).

The following values have been deduced empirically by Kilkenny from his calculation for the magnetic field configuration in the Polytron. The half-width r_o of the axial current profile in the plane of a cusp coil is given by

$$r_o = \frac{23 \pm 1}{\omega_o\tau} \text{ mm} \qquad 2.8$$

and the full half-width t_s of the sheath electric field by

$$t_s(r) = \frac{42 \pm 4}{\omega_o\tau \, I_1(kr)} \text{ mm} \qquad 2.9$$

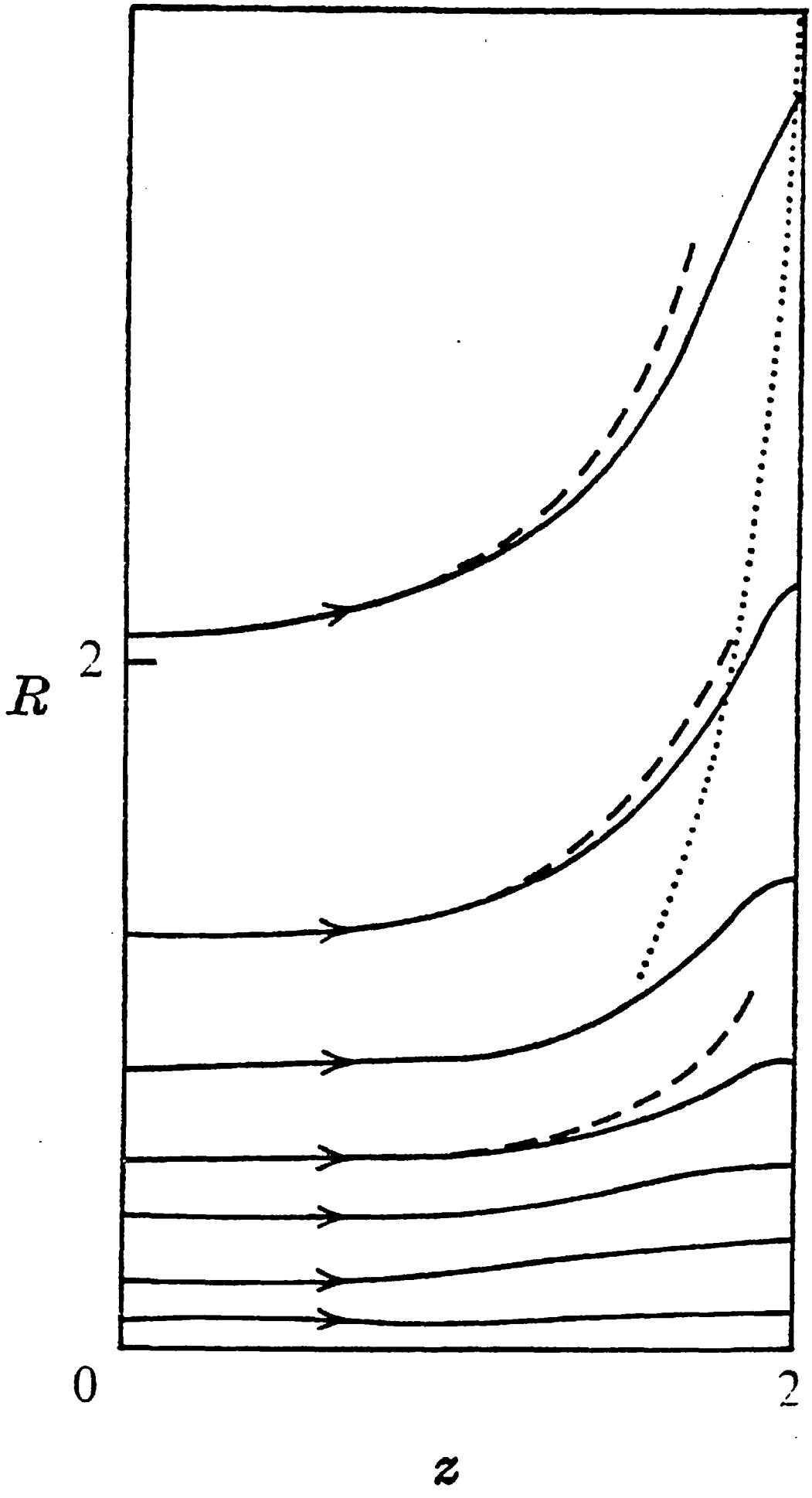

Fig. 2.2 Current field lines and magnetic field lines (----) for $\omega_c\tau = 10$. .... Edge of the sheath. Dimensions in centimetres. From Kilkenny[9] (1976).

and R the plasma resistance given by

$$R = \frac{L}{\sigma\pi\, r_b^2 (1 + 1.6\, \omega_o\tau)}\ \Omega \qquad 2.10$$

An average of the sheath thickness can be obtained from Equation 2.9.

$$\bar{t}_s = \frac{40}{\omega_o\tau}\ \text{mm} \qquad 2.11$$

This gives 5 mm to be compared with the value of $1.6 \pm .5$ mm inferred from experiment.

This model assumes a classical collision frequency. In the experiment for which values have been quoted the electron mean free path becomes comparable or larger than the sheath thickness 0.5 μs after the beginning of the discharge. This suggests that the model should not apply at later times. The observed thickness should then become smaller, closer to the value obtained from Equation 2.2.

2.3 Turbulence in the plasma sheath

Electrons in the sheath region have a large drift velocity $\underline{v_d}$ given by

$$\underline{v_d} = \frac{\underline{E} \times \underline{B}}{B^2} \qquad 2.12$$

For typical experimental conditions (U ~400V, B ~0.2T, t ~6 mm) a drift velocity of $\sim 10^5$ m/s is obtained. The ion-sound velocity $c_s = \left[k(T_e + T_i)/m_i\right]^{\frac{1}{2}} \sim 10^4$ m/s, and the electron thermal velocity $v_{T_e} = (k T_e/m_e)^{\frac{1}{2}} \sim 2 \times 10^6$ m/s. Thus $c_s < v_d < v_{T_e}$ and under these conditions it seems likely that microinstabilities could develop. The result would be to limit the drift velocity or give an effective collision frequency (Haines, 1977). Such effects would tend to broaden the sheath.

A detailed discussion of the instabilities that are likely to be present is given by Haines (1977). The cases to consider are ion-acoustic, modified two-stream, drift and electron cyclotron drift instabilities

Ion-acoustic instability is unlikely to occur, as it requires

$T_e >> T_i$, which does not hold in the Polytron.

Modified two-stream instability, considered by Buneman (1959, 1962), occurs at frequencies around $\omega^* = \frac{1}{2}(m_e/m_i)^{1/3}\omega_{pe}$, where ω_{pe} is the electron plasma frequency, provided

$$v_d > (c_s^2 + v_{T_i}^2)^{\frac{1}{2}} \qquad 2.13$$

and $v_d \geq \frac{k_{||}}{k_\perp} v_{T_e}$

and irrespective of the T_e/T_i ratio. c_s is the ion sound, v_{T_i} the ion thermal and v_{T_e} the electron thermal velocity. $k_{||}$ and $k_\perp$ are the parallel and perpendicular wavenumbers. For the experimental conditions quoted this instability is unlikely to occur except for the contribution of runaway electrons. For the case with $\Omega_e << \omega_{pe}$, where Ω_e is the electron cyclotron frequency, frequencies around ω_{pe} would be observed (Fainberg, 1962; Seidl and Sunka, 1967).

Drift instabilities can be demonstrated from the inclusion of gradients of magnetic field, density and temperature into the dispersion equation (Krall and Liewer, 1971). The gradient drift velocity v_Δ is given by

$$v_\Delta = -\frac{T_e}{m\omega_{ce}}\left[\frac{1}{n_e}\frac{dn_e}{dx} - \frac{1}{B}\frac{dB}{dx} - \frac{k^2 a_e^2}{2}\frac{1}{T_e}\frac{dT_e}{dx}\right] \qquad 2.14$$

where a_e is the electron Larmor radius and k the wavenumber. Drift instabilities can occur for arbitrary T_e/T_i and $k_{||} = \underline{k}.\underline{B}/B = 0$, provided $v_d v_\Delta > 0$, $v_d > c_s$ and $v_d > v_{T_i}$. The frequency and wavenumber for maximum growth rate are given by

$$\omega = \omega_{pi}\left(1 + \frac{\omega_{pe}^2}{\Omega_e^2}\right)^{-\frac{1}{2}}$$

$$k\lambda_D = \frac{c_s}{v_d}\left(1 + \frac{\omega_{pe}^2}{\Omega_e^2}\right)^{-\frac{1}{2}} \qquad 2.15$$

where ω_{pe} and ω_{pi} are the electron and ion plasma frequencies and Ω_e is the electron gyrofrequency.

For the experimental conditions the corresponding frequency and wavenumber are 3.7×10^8 rad/sec and 3.9×10^4 m^{-1}.

Electron cyclotron drift instabilities which arise from coupling of electron Bernstein waves with Doppler-shifted ion waves are possible

for $T_i \sim T_e$. In this case the dispersion relation is given by (Gary, 1971)

$$\frac{\omega}{k} = \sqrt{2}\, v_{T_i} \qquad 2.16$$

Instabilities that may occur in the present experiment are drift, electron cyclotron drift and runaway electron excited modified two-stream instabilities.

In experiments there exists an upper frequency limit of observability. In the present experiment the overall frequency response of the system is limited by the optical coupler (to be described in Section 2.6) used to 12 MHz. In view of this frequency limitation drift and modified two-stream instabilities would not be detectable. However, in an experiment by Hamberger and Jancarik (1970) excitation of Buneman type instability was seen to have a wide frequency spectrum. Frequency components at the predicted $\omega^* = \frac{1}{2}\left(\frac{m_e}{m_i}\right)^{1/3}\omega_{pe}$ and lower were observed. The low frequency components are well below the ion plasma frequency and should be observable in the present experiment.

2.4 Direct observation of the sheath: discussion of techniques

A diagnostic technique used to measure the sheath thickness should satisfy the following criteria:

(a) little plasma perturbation.
(b) good spatial resolution (of the order of or better than 1 mm) to be able to resolve the sheath structure.
(c) good temporal resolution (50 ns); ability to respond as fast as the applied electric field.
(d) ability to investigate the whole plasma volume of interest.
(e) ability to investigate over the time interval of interest (about 8 μs).
(f) capability of detecting waves due to microinstabilities, if present.

Criteria (a)-(e) are essential, whereas (f) is desirable as it would give additional information on the processes in the sheath region. The two methods considered were Thomson scattering and double electric probes.

2.4.1 Thomson scattering

This method allows determining electron density and velocity

distribution (Evans and Katzenstein, 1969). Thus, if there is a net drift of the electrons, the scattered profile should show this, provided the drift velocity is not too small relative to the electron thermal speeds. The value of drift velocity and magnetic field can be used to determine electric field from Equation 2.12.

This method satisfies conditions (a) to (c). However because of the geometry of the present device it is possible to obtain results only in the region near the centre of the discharge. Scattering from other regions would have intolerably high parasitic scattering levels. A second disadvantage is that in order to obtain the variation of the electric field at one point in space for the whole time of interest, a large number of discharges are required and the discharge reproducibility is not good, because of wall effects.

The last point to be considered is the capability of detecting waves in the sheath region. Thomson scattering gives information about electrons but not ions if $\alpha << 1$, α being defined as

$$\alpha = \frac{1}{k\lambda_D} \qquad 2.17$$

where k is the scattering wave number and λ_D the Debye length. Any instability in which ions play an important role would not be detected with $\alpha << 1$. To be able to do this it becomes necessary to use high α ($\alpha > 1$) scattering. In this case collective effects play a significant role and it is possible to obtain the ion velocity distribution. To achieve this it is necessary to use small scattering angles (less than 10°). This poses a new set of experimental problems, extremely difficult to solve in view of the constraints on plasma vessel geometry and high level of plasma light.

2.4.2 Double electric probe

For successful operation, a double probe has to satisfy certain basic conditions:

(i) Probe dimensions have to be very much larger than the Debye length, so that any plasma perturbation by the probe is localized in its immediate vicinity. The smallest probe dimension is the electrode diameter (in the probes used between 0.1 to 0.35 mm). This condition is easily satisfied, as the Debye length is less than 2×10^{-3} mm for all conditions studied.

(ii) The probe collecting area should be large enough, such that the

total current drawn by the probe is below the ion saturation current I_s. The ion saturation current has been obtained by Bohm, Burhop and Massey (1949) for a spherical probe and monoenergetic ions of 0.01 to 0.5 electron energy. The ion saturation current is given by

$$I_s = \tfrac{1}{2}\, e\, n\, A \left(\frac{kT_e}{m_i}\right)^{\frac{1}{2}} \qquad 2.18$$

where A is the probe collecting area.

The value given by Equation 2.18 has been found to apply for other geometries and even in the presence of a magnetic field (Chen, 1965).

The double probe is discussed now in terms of the criteria given in Section 2.4.

(a) The minimum probe electrode area can be determined from initial plasma parameters ($n \sim 4 \times 10^{20} m^{-3}$, $T_e \sim T_i \sim 2eV$, $E \sim 20$ kV/m) and probe electrode spacing. For a 1 mm electrode separation and a probe impedance of 100 Ohm the probe ion saturation current is 200 mA. From Equation 2.18 a minimum area of 2.8 mm^2 is obtained. At later times during the discharge the plasma temperature increases relaxing this requirement. The probe electrode area used is 2.85 mm^2.

(b) Spatial resolution, given by the probe electrode separation can be 1 mm. This is adequate to investigate the sheath structure.

(c) The time resolution of a double probe is limited by the sheath capacitance and probe impedance. The sheath thickness is of the order of the Debye length (2×10^{-3} mm). For the probe electrode dimensions used a capacitance of 8 pF is obtained. The probe sheath time constant is then 0.8 ns. The rise time of the external circuit is the limiting factor. The best risetime of the optical coupler used is 20 ns.

(d) A plasma region extending from nearly under a cusp coil to past the ring cusp region is accessible from the ports available for probe diagnostics.

(e) The potential difference at a particular point is followed over

the duration of the discharge.

(f) The presence of microinstabilities could be established. The minimum and maximum wavelengths are determined by electrode diameter (0.1 to 0.35 mm) and separation (1 to 2.5 mm). The highest frequency is determined by the overall risetime of the probe system of 20 ns. The equivalent frequency of 10^7 Hz is above the ion cyclotron frequency (5×10^5 Hz), slightly lower than the lower hybrid frequency (2×10^7 Hz) and well below plasma and electron cyclotron frequencies. Thus the only instabilities with an accessible frequency range are the drift and electron cyclotron drift instabilities.

The advantages of the double probe method over Thomson scattering make the decision to use a double probe quite clear cut.

2.5 Single and double probe description

Single and double probes are described here. A single electric probe was used to investigate a large common mode signal present in the double probe measurement.

A schematic diagram of a double probe is shown in Fig. 2.3. It consists of two 50 Ohm semirigid coaxial cables (type UT85, outer diameter .085") joined together side by side. Electrodes are of 0.1 or 0.35 mm diameter platinum wire, 2.5 mm long. Platinum is used because it does not oxidize, so there is no need to condition the probe before use. This is usually required for other electrode materials, electrodes being bombarded under vac uum to destroy any oxide layer present. The probe, except for electrode surfaces,is coated with an insulating layer of epoxy (Araldite CIBA) on top of which a ceramic coating (Ceramacoat) is applied. The ceramic coating lasts for 30 to 50 discharges, after which the probe has to be withdrawn from the system and recoated. Electrode separation used was from 1 to 2.5 mm.

The single probes used, also shown in schematic form in Fig. 2.3, consist of a single coaxial cable, at the end of which there is a resistor to which the electrode is attached. The purpose of this resistor (1 to 100 kΩ) is to increase the probe impedance from what would be obtained with the coaxial cable (50 Ω) only.

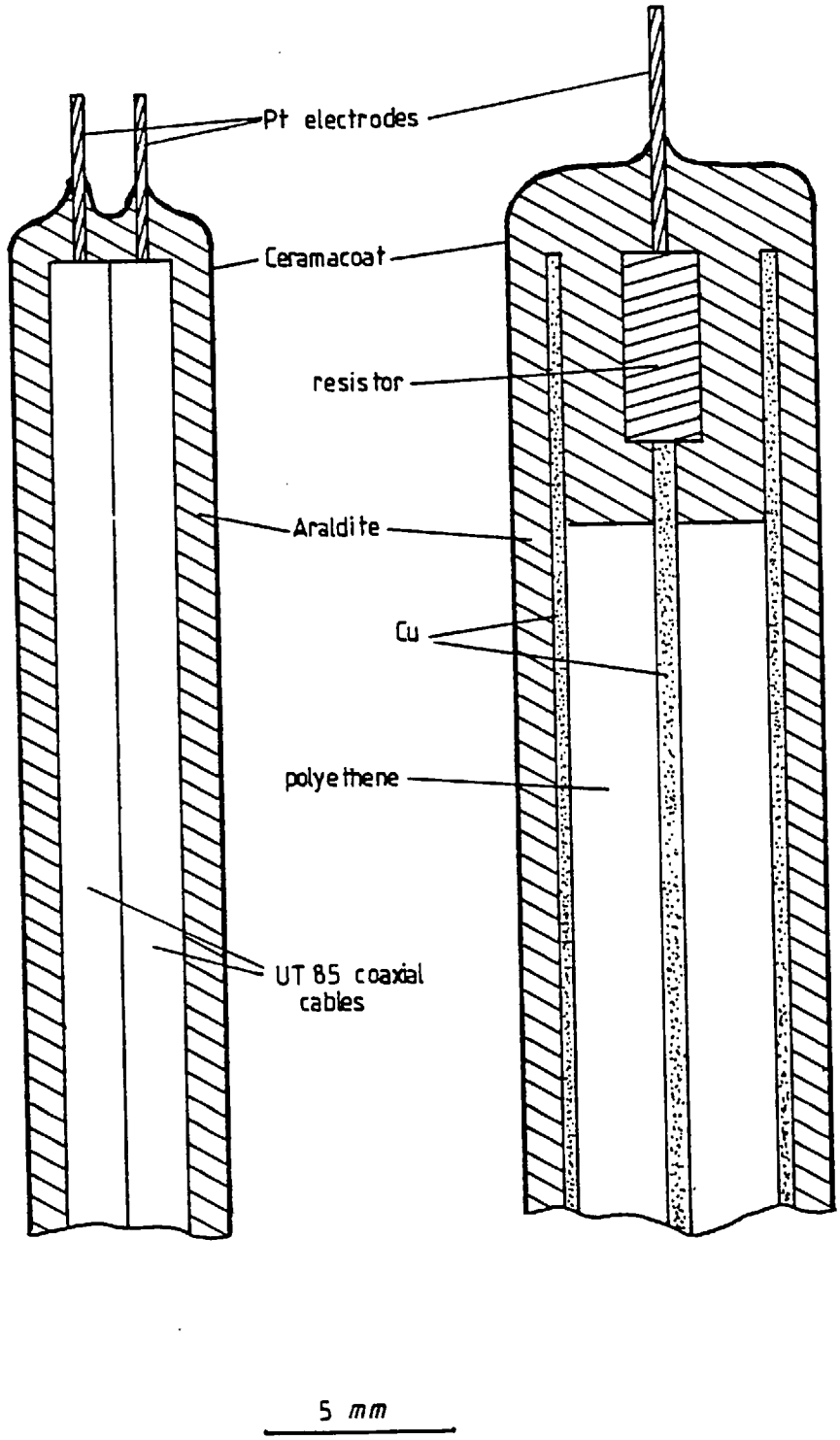

Fig. 2.3 Schematic drawings of single and double electric probes

2.6 Signal detection

Initially the probe output was fed into a balanced to unbalanced pulse transformer (ANZAC TP101) of wide bandwidth (100 kHz - 1 GHz). The common mode rejection ratio (CMRR) for this transformer over its bandwidth is 40 db (100:1). It became apparent that a large common mode voltage of up to 3 kV (the origin of which will be discussed in Section 2.8) was present. The smallest potential difference of interest is 3 V with a probe of 1 mm separation between electrodes. Clearly then, the CMRR of this pulse transformer is not adequate. An optically coupled system was designed to obtain the required CMRR. It consists of an emitter, where the voltage signal is converted to light signal, a light transmitting medium, in this case a fibre bundle, and a receiver which converts the light signal back to an electric signal. Fast high voltage optical couplers were not commercially available at the time.

The system is shown in schematic form in Fig. 2.4. The probe was connected to a 100 Ω load resistor. This ensured that the cables which form part of the probe were correctly terminated. In parallel with this load there are two resistors R_s in series with two DC blocking capacitors C and a fast (1 ns risetime) red emitting diode (LED). The LED is forward biased by a set of batteries in series with biasing resistors R_b. This is to ensure that

$$2R_s >> R_d \qquad 2.19$$

where R_d is the LED forward resistance. In practice this means that the LED is emitting at constant level in absence of input signal. The LED used (Monsanto MV55) has a linear light output to current input dependence. Hence, an approximately linear relationship between probe voltage and light emitted will result provided inequality 2.19 holds.

As a reverse voltage protection for the LED, another LED is connected back to back. To avoid frequency dependence the blocking capacitors should present an impedance such that

$$R_s >> \frac{1}{\omega_o C} \qquad 2.20$$

where ω_o is the lowest frequency of interest (10 kHz, the ringing frequency of the main bank). Biasing resistors have to be chosen so that

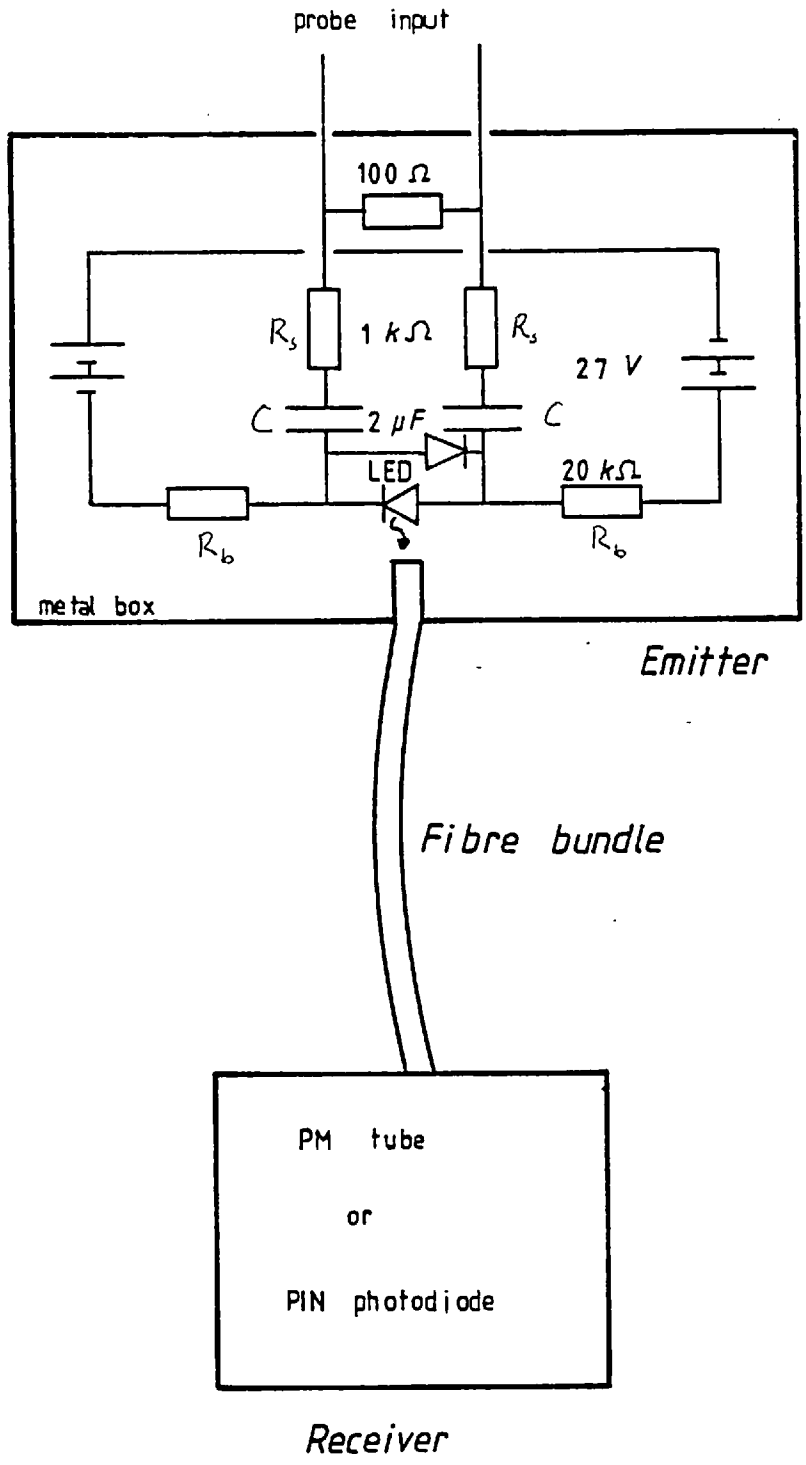

Fig. 2.4 Schematic diagram of the optical coupler system

$$R_b >> R_d \qquad 2.21$$

otherwise part of the signal is diverted through the batteries.

The light emitted by the LED goes through a 3 mm diameter, 1.2 m long fibre bundle to a photomultiplier tube (PM tube, RCA 7265) which has an adequate red response and fast risetime (10 ns with the dynode chain biasing circuit used). The main disadvantage of PM tubes is that the DC anode current must not exceed a fairly low level, otherwise the long-term performance of the tube is degraded. The maximum DC anode current allowed in this case is 1 μA (RCA 7265 data sheet). This means that useful operation with good signal to noise ratio is only possible for single signal polarity corresponding to increases in light flux.

The overall risetime of the system, including probe and oscilloscope, is 20 ns. The measured CMRR is better than 60 db (1000:1), with an input pulse risetime of less than one nanosecond. This is at least two orders of magnitude better than obtained with the pulse transformer, as the CMRR of the latter is very poor for signals outside its passband. The CMRR of the system is very sensitive to lay-out, due to stray capacities.

To be able to record voltages in which a polarity reversal occurs the system was modified, the PM tube replaced by a PIN photodiode amplifier combination (Bell & Howell 509-0015) and the red LED by an infrared one (ME60) to match the PIN photodiode response. This combination allows a high DC level, limited by dissipation in the PIN photodiode amplifier. The output peak to peak voltage obtained is 0.5 volts.

2.7 Induced electric field

A measurement of the total induced emf is required in order to compare it with the local electric fields measured by double probes in the plasma. This is done by placing a high resistance wire (25 kΩ/m) around the torus, in close contact with the quartz vessel wall and at the same major radius as the plasma. The total resistance of the measuring loop is 46.6 kΩ. For the highest main bank operating voltage (25 kV) the maximum current through the loop is 500 mA. The presence of this loop does not interfere with preionization nor main discharge, and can therefore be

left permanently in position.

Fig. 2.5 is an equivalent circuit for measuring loop, plasma and induction rod system. The induction rod system is represented by a single inductance and single mutual inductances.

The circuit equations for measuring loop and plasma are

$$L_m \frac{di_m}{dt} + R_m i_m + M_{im} \frac{di_i}{dt} - M_{pm} \frac{di_p}{dt} = 0$$

$$(L_{PL} + L_H)\frac{di_p}{dt} + R_p i_p + M_{ip} \frac{di_i}{dt} - M_{mp} \frac{di_m}{dt} = 0 \qquad 2.22$$

where subindices m denote measuring loop, p plasma, i induction rod, PL plasma loop and H Hall plasma inductance.

Terms involving $\frac{di_m}{dt}$ can be neglected as i_m is very much smaller than all other currents. Also $M_{im} \simeq M_{ip}$ as plasma and measuring loop are close together and the plasma-measuring loop mutual inductance (M_{mp}) is about 20% of the total plasma inductance ($L_{PL} + L_H$) and can be neglected. With these approximations Equation 2.22 becomes

$$V_m = R_m i_m \simeq (L_G + L_H) \frac{di_p}{dt} + R_p i_p \qquad 2.23$$

The right-hand side of equation 2.23 is the applied voltage to the plasma. The optical coupler used with the probe is used to measure a fraction of V_m. The risetime of the system is limited by the optical coupler.

2.8 Single probe measurements

The results obtained from single probe measurements are given and dicussed in this section.

Fig. 2.6 shows a typical signal obtained with a single probe together with the induced electric field in the absence of plasma. The voltage at the probe end is 2 to 3 kV with respect to the screened room earth or the nearest cusp coil earth. The main features of this signal are:

i) It is always positive.

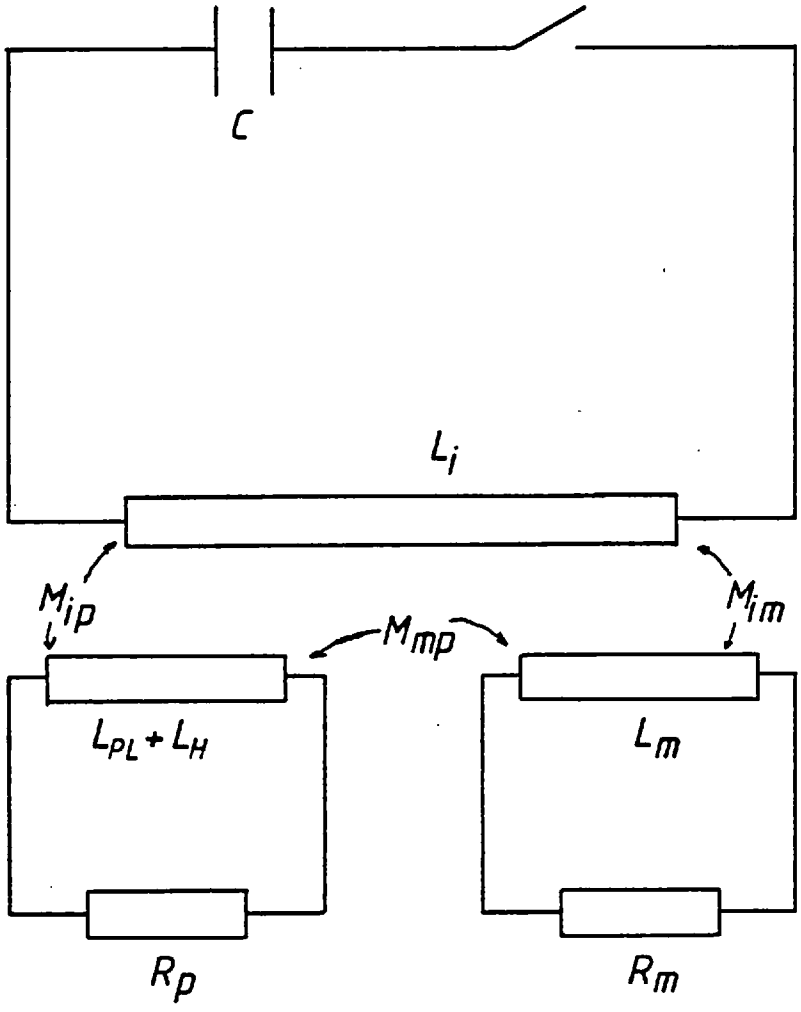

Fig. 2.5 Schematic circuit diagram of the induced electric field measuring loop

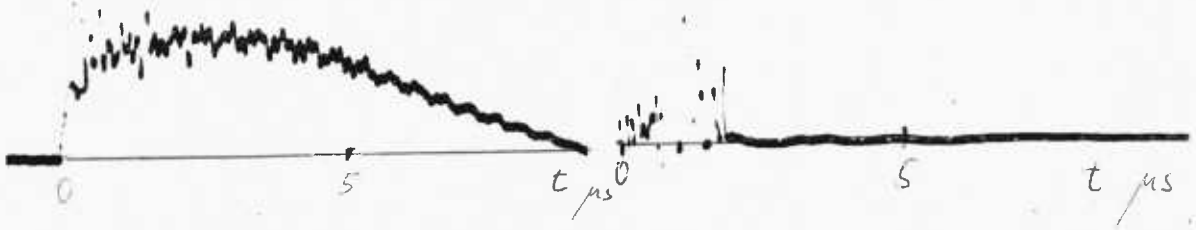

Fig. 2.6 Typical signal obtained with a single probe (right) shown alongside the vacuum induced electric field.

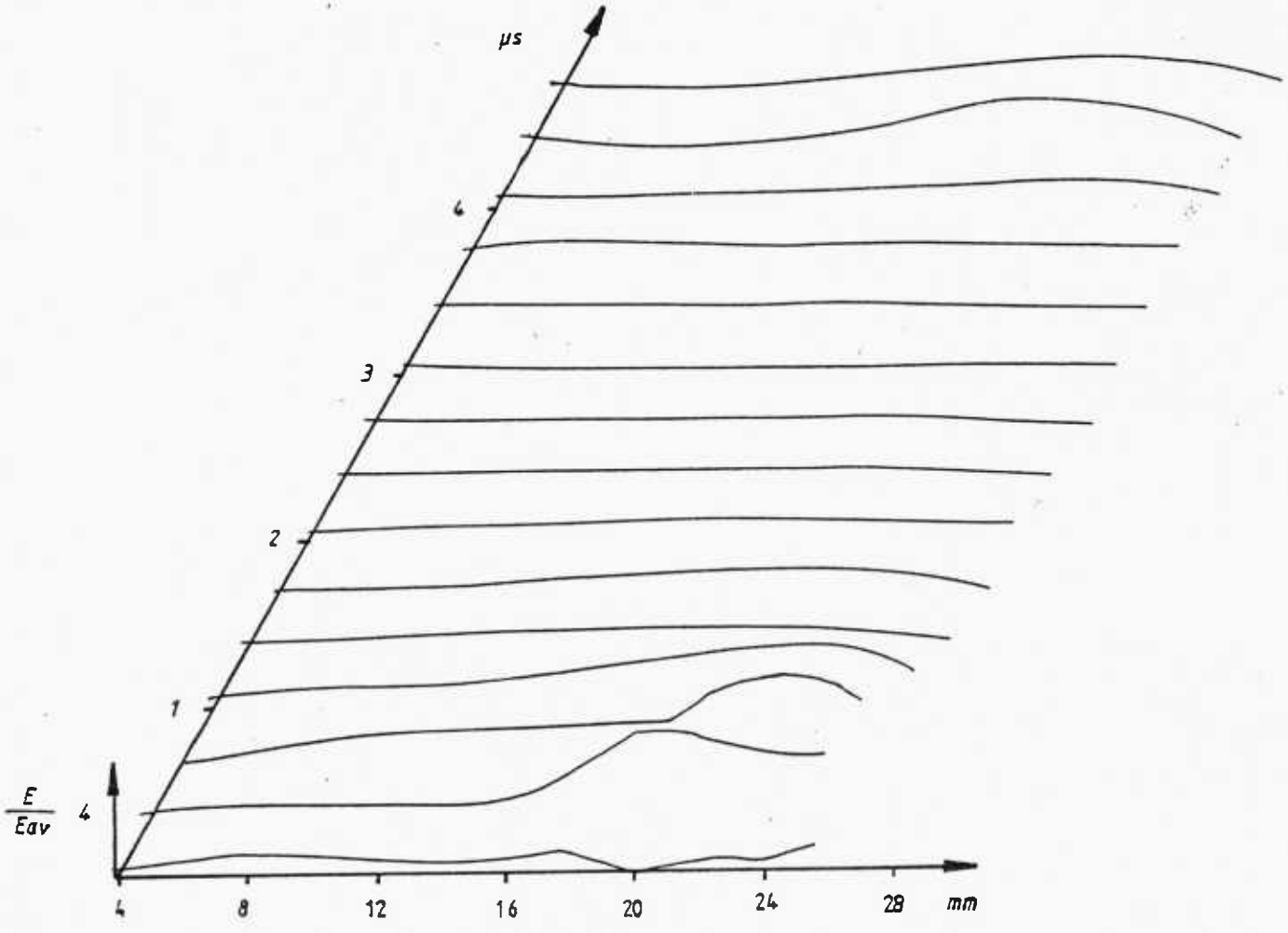

Fig. 2.7 Double electric probe results showing normalized electric field as a function of time and position. V_m = 15 kV, V_c = 1.5 kV, p = 3.5 mTorr, no vertical magnetic field.

ii) It does not depend on the main bank polarity.

iii) It increases with main bank voltage.

iv) It is not present in the absence of plasma.

v) The presence of the cusp magnetic field does not change it significantly.

vi) The time over which this signal is present is slightly shorter than the duration of the linearly rising phase of the plasma current.

vii) The FWHM of the spikes in the signal is density dependent, decreasing with increasing density.

viii) The magnitude depends only slightly on the radial position of probe relative to the minor axis.

ix) The magnitude is independent of density.

x) This signal is present before the main bank switch-on, at the time when the main bank triggering circuit is fired. This is clearly seen in Fig. 2.6.

xi) The observed frequency of the signal is of the order of 5 MHz.

This is similar to frequencies generated by the main bank. These high frequency components appear as a result of reflections of the triggering pulse. The main bank is of multiple spark gap design. Different elements are interconnected by cables. The spark gaps are triggered by a 60 kV voltage pulse from a pulse line generator using coaxial cables. The triggering pulse is delivered to the spark gaps through a 9 m long, 50 Ohm coaxial cable. The main bank capacitors are connected to the induction rods via four parallel 5.3 m lengths of 50Ω coaxial cables. The double transit time of the two cables (trigger and induction rod) in series is equal to half the period of the observed high frequency components in the induced voltage.

The high voltage signals observed with the single probe could be explained as generated either by instabilities, or induced voltage from the main bank being picked up by the probe or loss of runaway electrons.

For an instability to grow, an energy source is required. If this energy source is ion or electron energy the maximum amplitude of the instability will be limited by non-linear effects. The maximum amplitude will be of the same order as the plasma particle energy, a few tens of eV in this case. This is several orders of magnitude lower than the observed voltage. A further point against the possibility of

instabilities being responsible for the observed voltage is the fact that this voltage is asymmetric, i.e. is always positive. None of the instabilities described would show this type of behaviour.

Because of difficulty associated with the sealing of the probe into the discharge vessel, there is an uninsulated region on the stem of the probe, some 10 cm back from the tip. The exposed part of the loop formed between the tip and the back of the probe has an area of at most 10 cm^2. The area of the loop defined by the induction rods is 2000 cm^2. The expected induced voltage in the loop formed around the probe should be 200 times smaller than the applied induced voltage. The voltage obtained in this case would be less than 150 V for any of the charging voltages used. The observed voltage cannot be explained by this mechanism.

The other mechanism capable of generating high enough voltages is generation of runaway electrons (Dreicer, 1959). A loss of runaway electrons to the discharge vessel walls would account for the high positive plasma potential. The potential drop occurs in this case in the immediate vicinity of the wall. The number γ_r of runaway electrons generated per electron and per unit time is given by

$$\gamma_r = 0.35\ \nu_{ee}\left(\frac{E_r}{E}\right)^{3/8} \exp\left\{-\left[\left(\frac{2E_r}{E}\right)^{\frac{1}{2}} + \left(\frac{E_r}{4E}\right)\right]\right\} \qquad 2.24$$

where ν_{ee} is the electron-electron collision frequency, $E_r = \frac{m \nu_{ei} v_{T_e}}{e}$ is the runaway critical field and E is the applied electric field (Kulsrud et al., 1973), $\nu_{ei} = \frac{n Z^2 e^4 \ln\Lambda}{4\pi \varepsilon_o^2 v_{T_e}^3}$ is the electron-ion collision frequency, Z the charge number and $\ln\Lambda$ the coulomb logarithm.

The number n_r of runaways per unit volume per unit time is obtained from

$$n_r = n\gamma_r \qquad 2.25$$

n_r has been calculated for two different main bank voltages at two different times. The calculation is done using the measured plasma parameters in Equations 2.24 and 2.25. The results are given in Table 2.1.

Runaway electrons can escape when their Larmor radius is of the same order or larger than the plasma container. In the presence of the

Table 2.1

Number of runaways per cm^3 per sec 1.5 kV cusp bank charging voltage, 3.5 mTorr filling pressure.

Time \ Main bank voltage	10 kV	20 kV
0.5 μs	9.4×10^{24} $m^{-3}s^{-1}$	6.2×10^{26} $m^{-3}s^{-1}$
1.5	1.4×10^{24}	1.5×10^{26}

cusp magnetic field the electron Larmor radius is much smaller than the container. However, the magnetic field lines are not closed so runaway electrons can be lost to the container's walls. The poloidal magnetic field generated by the plasma current can become large enough to prevent electron runaway loss. For a 1 kA plasma current, electrons with a 3 keV energy have a Larmor radius of the same order as the container's walls' radius. The single probe signal is seen to disappear when the plasma current is 4 to 5 kA.

The capacitance of the plasma container to ground is approximately

$$C = (2\pi)^2 R \frac{\varepsilon_o}{\cosh^{-1}(h/a)} \qquad 2.26$$

where R is the major radius, h the distance from ground, a the minor radius.

The number of electrons required to charge this capacitance to 3 kV is 4×10^{11}. The plasma volume is 0.008 m^3 and the half-width of the high voltage spikes of the order of 50 ns. With these values and the smallest figure in Table 2.1 a total number of runaway electrons in 50 ns is 5.6×10^{14}. This is three orders of magnitude higher than the number of electrons required to generate the observed voltage.

The loss of runaway electrons seems to be consistent with the behaviour of the single probe signals obtained. It should be possible to detect experimentally the existence of runaway electrons. At the time the electric probe results were obtained it was felt that as this high plasma potential is not specifically a Polytron effect, a further investigation of it should be left to a later date.

2.9 Double probe measurements

Early on in our double probe measurements, it became apparent that the jitter on the cusp bank spark gaps would be too large to obtain a good estimate of the sheath thickness. The jitter between spark gaps is 400 ns, which gives a shift of the ring cusp region of 2 mm. This is of the same order as the desired resolution. To overcome this problem, several cusp coils and capacitors (two groups of six each) were connected in parallel, the total capacitance being 1296 μF (216 μF previously), six (one previously) coils connected to it. This gives a slightly lower peak magnetic field (25% lower) and correspondingly longer cusp bank period. This is partly compensated by firing the cusp bank earlier. The magnetic field in any cusp region is to a good approximation determined by four cusp coils on either side of the cusp under consideraton. Two groups of six were modified. The lifetime of the spark gaps was about 50 discharges against several hundred for the previous scheme.

Fig. 2.7 gives the electric field in the sheath region as function of position and time for one of the conditions studied. Each point is an average of at least three shots. The total number of discharges to obtain this is 50 or so, being limited by the probe coating lifetime. Normalized peak electric field versus time is shown in Fig. 2.8 for the same conditions. Results obtained in two different runs are shown. The normalization is carried out using the average applied electric field, measured by the induced voltage loop. The sheath structure develops in times slightly under a microsecond. It disappears during the initial loss (first described by Kilkenny, 1972) and sometimes reappears later in the discharge.

Sheath thickness as a function of radius is given in Fig. 2.9. The solid line is obtained from Kilkenny's (1976) resistive calculation. Fig. 2.10 shows the measured sheath thickness as a function of pressure. The measured sheath thickness is in good agreement with Kilkenny's collisional model, even at times when the mean free path is of the same order or larger than the sheath thickness. This could be due to the presence of microinstabilities. No instabilities with frequencies lower than 10 MHz and wavelengths between 0.35 to 3 mm were detected. It is possible that other instabilities, like modified two-stream type, were present. Their frequency is much higher than the limit imposed by the optical coupler used. This instability could be excited by runaway

Fig. 2.8 Peak normalized electric field as a function of time for V_m = 15 kV, V_c = 1.5 kV, p = 3.5 mTorr, no vertical magnetic field. Two different results for the same plasma conditions are shown.

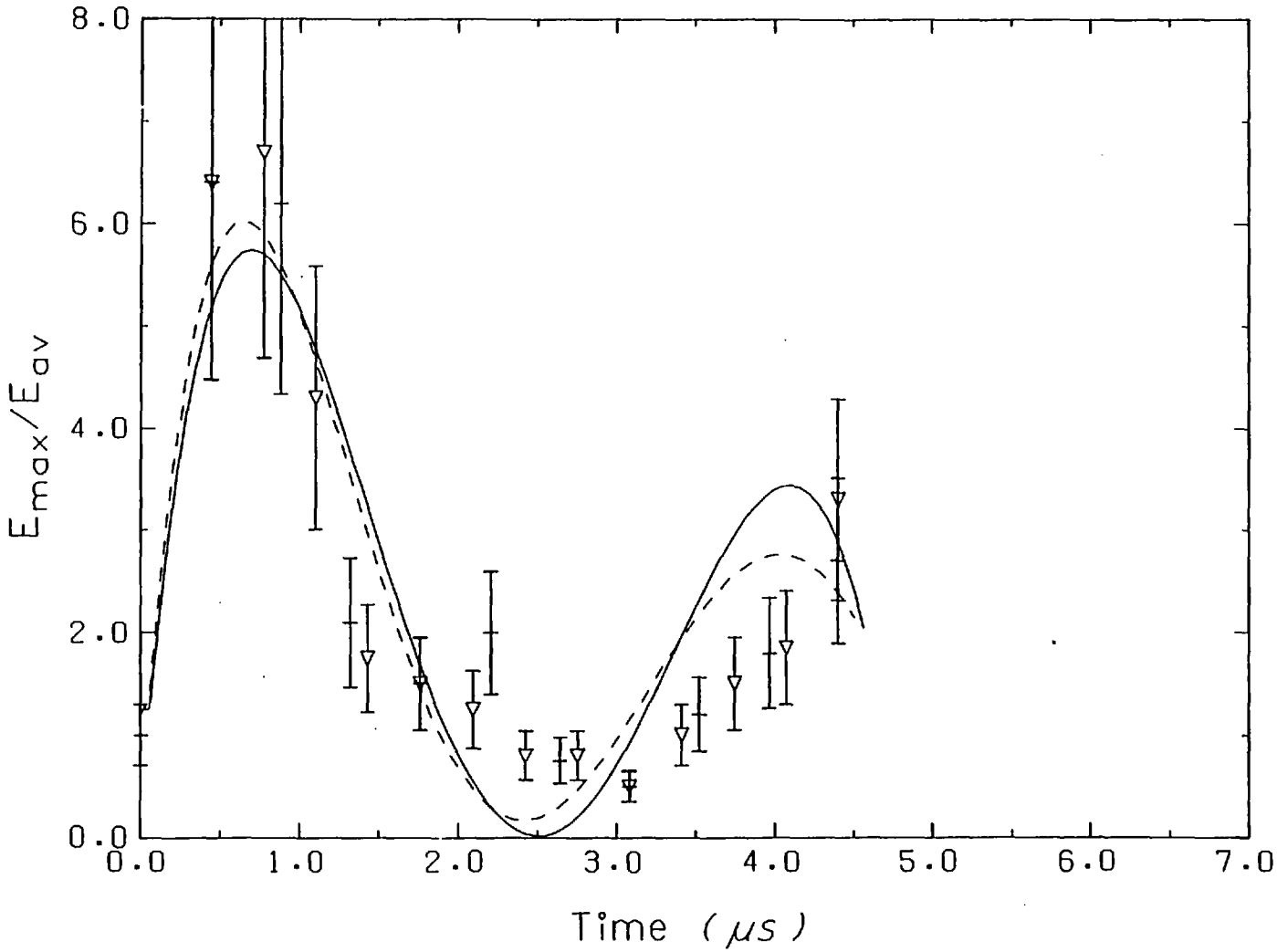

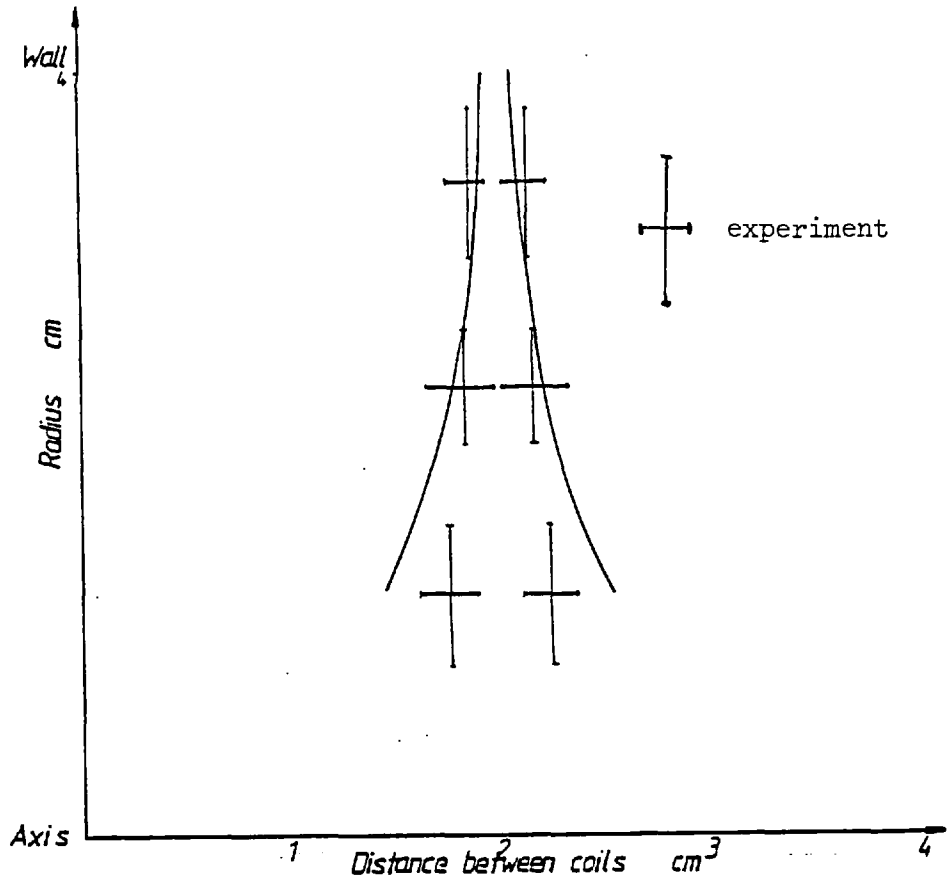

Fig. 2.9 Sheath thickness as a function of radius from Kilkenny (1976) and measured values for V_m = 15 kV, V_c = 1.5 kV, p = 3.5 mTorr.

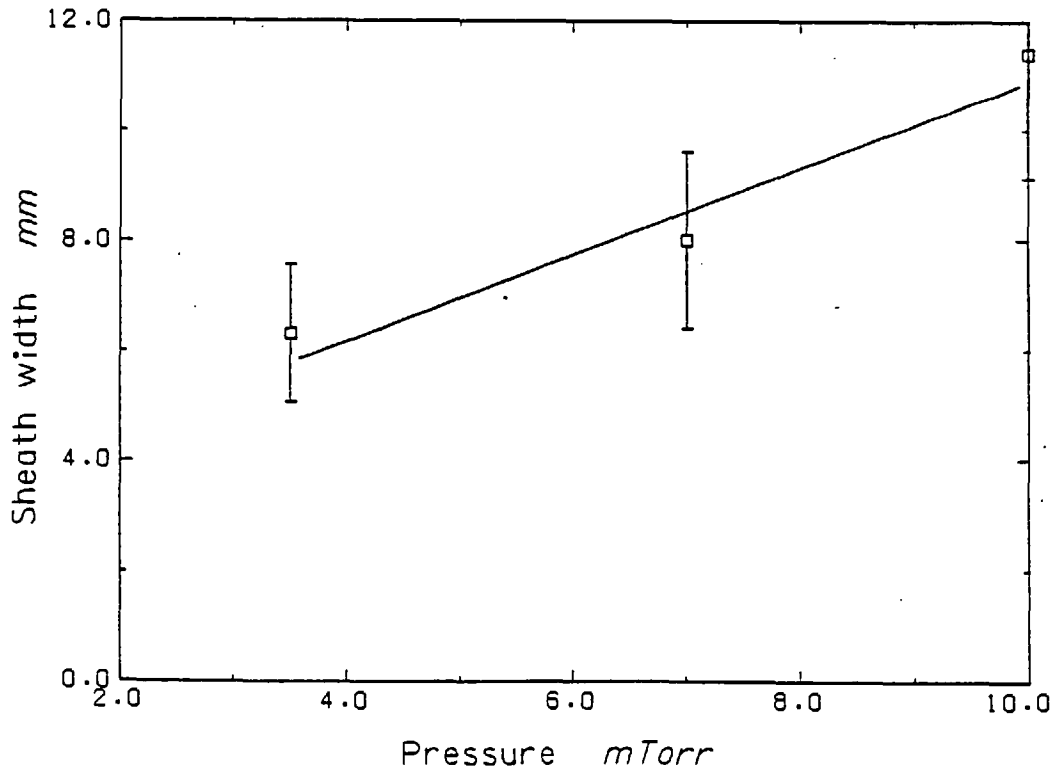

Fig. 2.10 Sheath thickness as a function of pressure, at a radius of 3 cm, for V_m = 15 kV, V_c = 1.5 kV, t = 1.0 μs, no vertical magnetic field.

electrons.

2.10 Radial electric field

In the Polytron ions are contained by having an axial velocity much larger than their thermal velocity, whereas electrons, which are free to move along magnetic field lines, are contained by a radial electric field. An estimate of this electric field can be made for a steady state situation. Using Ohm's law

$$\frac{1}{\sigma}\underline{j} = \underline{E} + \underline{v} \times \underline{B} - \frac{\underline{j} \times \underline{B}}{ne} + \frac{\nabla p_e}{ne} \qquad 2.27$$

where σ is the plasma conductivity and $p_e = nkT_e$, the electron plasma pressure.

The radial component in cylindrical coordinates is

$$\frac{1}{\sigma}j_r = E_r + v_\theta B_z - v_z B_\theta - \frac{j_\theta B_z}{ne} + \frac{j_z B_\theta}{ne} + \frac{\frac{\partial(nkT_e)}{\partial r}}{ne} \qquad 2.28$$

and from Maxwell's equations

$$\mu_o j_r = -\frac{\partial B_\theta}{\partial z} \qquad 2.29$$

In the ring cusp region $B_z \simeq 0$. The radial electric field can then be obtained from Equations 2.28 and 2.29:

$$E_r = v_z B_\theta - \frac{j_z B_\theta}{ne} - \frac{1}{\mu_o \sigma}\frac{\partial B_\theta}{\partial z} - \frac{\frac{\partial(nkT_e)}{\partial r}}{ne} \qquad 2.30$$

Assuming that $\frac{\partial}{\partial r} \sim \frac{\partial}{\partial z} \sim \frac{2}{L}$, where L is the cusp separation, $T_e \sim 2eV$, $j_z \sim .25 \times 10^7 \frac{A}{m^2}$, $B_\theta \sim 3 \times 10^{-2} T$, $v_z \sim 2 \times 10^4 m/s$, which are typical experimental values, a radial electric field of $E_r \sim -2 \times 10^3 V/m$ is obtained.

An attempt to measure this electric field was made with a double probe in which the electrodes are at different radial positions. The electrode separation used is 3.5 mm. The minimum detectable electric field is determined by probe pick-up. Probe pick-up limits the minimum

detectable voltage to 10 volts, equivalent to 3 kV/m, and no such signals were observed.

In a situation with no cusp magnetic field present, a toroidal z-pinch develops. For this case the magnitude of the electric field can be calculated from Ohm's law and Maxwell's equations. Assuming that the velocity is negligible in Ohm's law, that the only magnetic field component is B_θ and that there is no radial current, the r and z components are

$$\sigma E_r = -\frac{j_z B_\theta}{ne}$$

$$\sigma E_z = j_z \qquad 2.31$$

At the plasma surface, the magnetic field is given by

$$B_\theta = \frac{\mu_o I_z}{2\pi r}$$

$$B_\theta = \frac{\mu_o j_z}{(2\pi r)^2 \delta} \qquad 2.32$$

where δ is the thickness over which the current is flowing.

From Equations 2.31 and 2.32 the radial field is

$$E_r = \frac{\mu_o \sigma E_z^2}{ne(2\pi r)^2 \delta} \qquad 2.33$$

The radial electric field was measured for this case with $n \sim 4 \times 10^{20} m^{-3}$, $T_e \sim 2eV$, $E_z \sim 3 \times 10^3$ V/m. The value of δ is obtained from the velocity of shock front and the duration of the E_r signal. In this case $\delta \simeq 1$ cm, giving a calculated value of E_r of 5.6×10^4 V/m. The measured value is 4.5×10^4 V/m.

2.11 Conclusion

The results obtained indicate that there is a region of enhanced electric field near the ring cups region where most of the voltage drop occurs. This is in good agreement with Kilkenny's MHD collisional calculation. This is so even at late times during the discharge when the mean

free path is of the same order as the discharge vessel radius. Micro-instabilities giving an effective collision frequency might be responsible for this.

No low frequency instabilities have been detected. This rules out the presence of ion-acoustic, magnetoacoustic and gradient drift instabilites. Instabilities that are beyond the frequency detection capability of the probes used are those associated with runaway electron production.

A high positive plasma potential has been observed, apparently due to the loss of runaway electrons.

Chapter 3

FORCES ON A PLASMA LOOP AND DIAGNOSTICS EMPLOYED

In this chapter the effects of self and externally applied magnetic fields on a single plasma current loop are analysed. A description of the diagnostic techniques used to assess the effect of an externally applied vertical magnetic field on the Polytron plasma is given.. Results obtained from these measurements will be given in the following chapter.

3.1 Self-force on a single circular current loop

The force on a circular current loop generated by its own magnetic field can be calculated by two methods:

(i) dividing the circular current loop of finite cross-section into a set of elementary loops of infinitesimal cross-section and evaluating the magnetic field on an elementary loop produced by all other elements. The force acting on a length $d\underline{l}$ of an elementary loop carrying a current I is

$$d\underline{f} = I\, d\underline{l} \times \underline{B} \qquad 3.1$$

where $\underline{B}$ is the magnetic field produced by all other elementary loops.

(ii) using the virtual work principle.

The method used here is the second one. For a circular current loop (see Fig. 3.1) of major radius R and minor radius a, the work required to change the major radius by δR is

$$\delta W = \frac{\partial W}{\partial R}\,\delta R \qquad 3.2$$

where W is the total magnetic field energy and is given by

$$W = \tfrac{1}{2} L I^2 \qquad 3.3$$

L being the loop inductance and I the current.

Fig. 3.1 Schematic diagram of a circular current of major radius R, minor radius a.

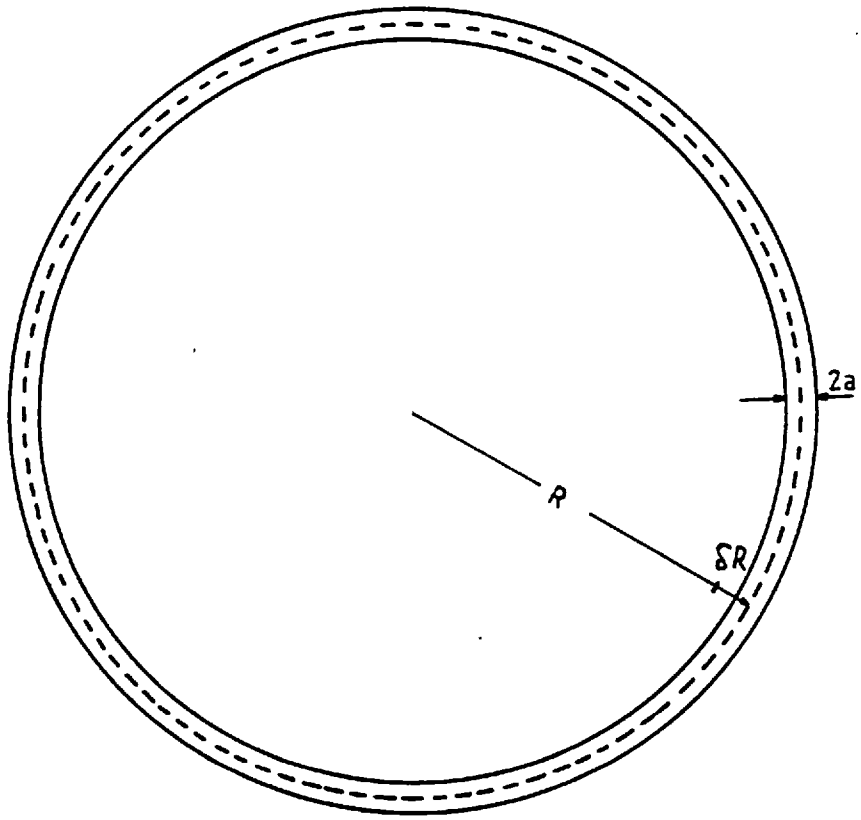

A force f_s per unit length acting uniformly outward generates, for a displacement δR, a total work of

$$\delta W = 2\pi R f_s \delta R \qquad 3.4$$

From 3.2 and 3.4 the outward force per unit length becomes

$$f_s = \frac{1}{2\pi R} \frac{\partial W}{\partial R} \qquad 3.5$$

assuming that the loop current does not change; from 3.3 and 3.5

$$f_s = \frac{I^2}{4\pi R} \frac{\partial L}{\partial R} \qquad 3.6$$

Assuming uniform current distribution the inductance of a circular loop is given by

$$L = \mu_o R\left[\ln \frac{8R}{a} - 1.75\right] \qquad 3.7$$

The outward force per unit length on the current loop is obtained from 3.6 and 3.7:

$$f_s = \frac{\mu_o I^2}{4\pi R}\left[\ln\frac{8R}{a} - 0.75\right] \qquad 3.8$$

3.2 Force on a toroidal plasma

In a toroidal plasma, if there are no mechanical constraints, self-force given by Equation 3.8 will give rise to an outward radial motion causing the plasma to hit the container walls. This can be prevented by having a restraining magnetic field or a conductive liner (Leontovich, 1951). In the latter scheme any plasma motion will induce currents in the liner which interact with the plasma current to prevent the outward drift. In order to apply this scheme the timescales of the induced electric field and the plasma motion have to be of different orders of magnitude. Otherwise the electric field is shorted out by the conducting wall. In the present Polytron device both timescales are of the same order of magnitude. This scheme is therefore not applicable.

The alternative method is to apply an external magnetic field perpendicular to the plane of the torus using a set of current-carrying conductors. The force per unit length on a thin conductor in a perpendicular magnetic field is given by

$$f_a = IB_z \qquad 3.9$$

where I is the total current flowing through the conductor and B_z is the applied magnetic field. This force will be inwards if the applied magnetic field is anti-parallel to the magnetic field produced by the loop at its centre. Equilibrium is obtained, assuming no other forces are present, if

$$f_s = f_a \qquad 3.10$$

at all times. The required magnetic field in terms of the total current flowing is obtained from 3.8, 3.9, 3.10:

$$B_z = \frac{\mu_o I}{4\pi R}\left[\ln\frac{8R}{a} - 0.75\right] \qquad 3.11$$

For a typical plasma current (10 kA) in the Polytron the required vertical magnetic field is 0.018T.

3.3 Vertical magnetic field generation

It is clear from results of the previous section that the required magnetic field should have the same time dependence as the plasma current. The application of a vertical magnetic field will change the plasma position. As a consequence of this the plasma current changes, the plasma being in a different cusp magnetic field region. Ideally the magnetic field generated should follow these changes by sensing the current magnitude and plasma position. This, although possible in principle, is very difficult to achieve and extremely expensive, as it requires high voltage, high power feedback amplifiers, with fast response (less than a microsecond), and was beyond our resources. An alternative, and very much simpler, scheme can be implemented in the form of a preprogrammed vertical magnetic field, the problem being that this field will change the plasma current. A successive approximation scheme must be used to obtain an optimum situation for each set of plasma and electric and magnetic field conditions. A fairly broad range of magnetic field values can be obtained by adding or removing induction rods, in particular if they are connected to separate capacitor banks.

A computer program, originally developed by Kilkenny (1972), was modified to calculate the magnetic field produced by the induction rod system. The calculation assumes that the plasma is a single conductor of finite size and uniform current distribution.

The magnetic vector potential for a single circular current element in cylindrical coordinates is given by (Durand, 1968)

$$A_\phi = \frac{\mu_o I}{k\pi}\sqrt{\frac{a}{r}}\left[\left(1 - \frac{k^2}{2}\right)K - E\right] \qquad 3.12$$

$$A_r = A_z = 0$$

where a is the current element radius and

$$k = \sqrt{\frac{4ar}{(a + r)^2 + z^2}}$$

$$K = \int_0^{\pi/2} \frac{d\psi}{\sqrt{1 - k^2 \sin^2 \psi}}$$

$$E = \int_0^{\pi/2} \sqrt{1 - k^2 \sin^2 \psi}\ d\psi \qquad 3.13$$

K and E are the complete elliptic integrals of first and second kind.

The magnetic field components are obtained from 3.12:

$$B_r = -\frac{\partial A_\phi}{\partial z}$$

$$B_\phi = 0 \qquad 3.14$$

$$B_z = \frac{1}{r}\frac{\partial}{\partial r}(r A_\phi)$$

Magnetic field lines can be defined as

$$\frac{dr}{B_r} = \frac{dz}{B_z} \qquad 3.15$$

Combining 3.14 and 3.15:

$$d(r A_\phi) = 0 \qquad 3.16$$

Hence $r A_\phi$ = constant defines a field line. This was used to calculate the magnetic field lines.

A fairly large number of induction rod configurations were studied, in which rods were connected in parallel and driven by the existing main bank. This was the only scheme considered in view of its greater flexibility and the fact that it allowed reversion to the previous configuration. This was required for comparison purposes, and in the event of a negative result being obtained of the application of the vertical magnetic field.

Figs. 3.2 and 3.3 show the results of this calculation for two configurations, the low magnetic field design of Kilkenny's and one of the vertical magnetic field cases used. The values of magnetic field quoted are peak values, i.e. a quarter period after the beginning of the main discharge. The peak field is higher than that required to balance the

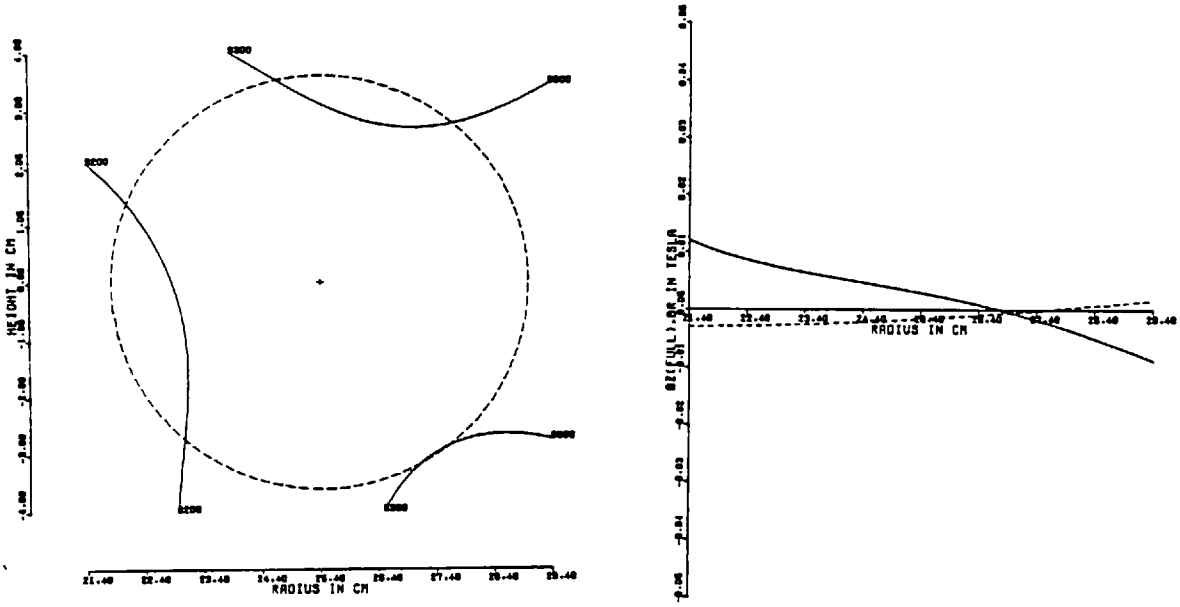

Fig 3.2

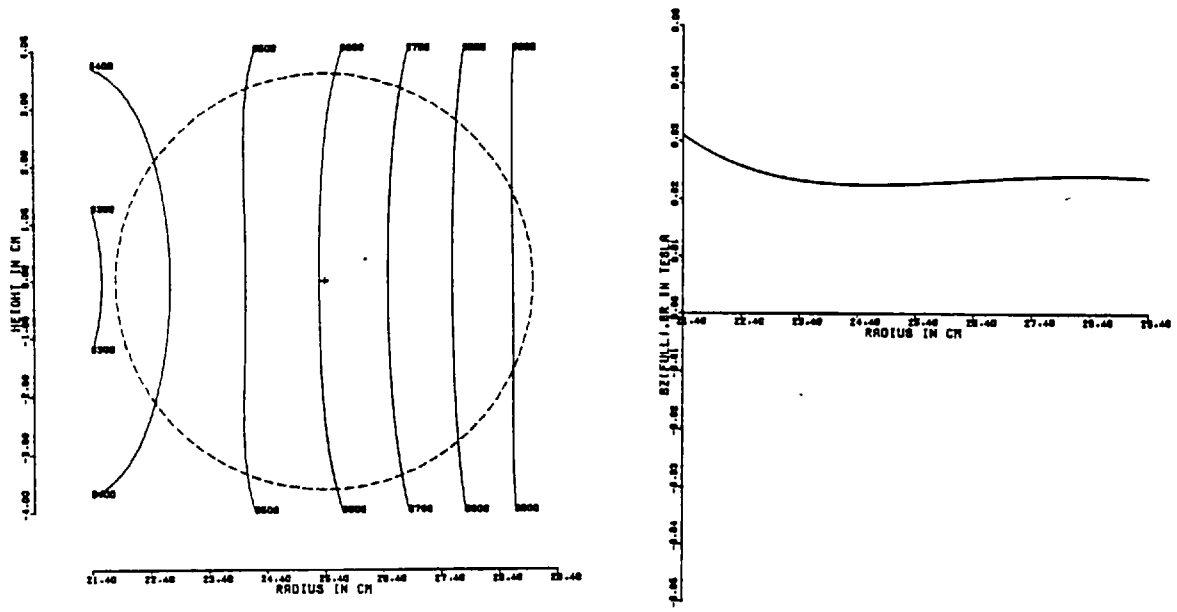

Fig 3.3

Fig. 3.2 Magnetic field generated by the initial rod configuration. This configuration is referred to as "no magnetic field case".

Fig. 3.3 Magnetic field generated by a four induction rod configuration used. The induction rods have major radii of 20.5 and 30.4 and distance from the horizontal plane of $\pm$ 9.6 cm.

field due to plasma current at the corresponding time. This is necessary so as to have a value closer to the required one during the initial stage. The magnetic field has a sinusoidal dependence whereas the plasma current has a fast risetime followed by a constant or nearly constant phase (see Chapter 4).

3.4 Vertical magnetic field produced by an independent capacitor bank

Initially, an independent auxiliary capacitor bank of 20 μF, 20 kV was used, connected to two additional separate induction rods of 34 cm radius, 5 cm either side of the horizontal plane of symmetry , the peak magnetic field at the plasma position being 0.08T. Some results were obtained, which are presented in the next chapter. The scheme was rapidly abandoned, as one of the capacitors on the auxiliary bank became short-circuited, presumably due to induced voltages from the main bank. The coupling between banks is quite high, the coefficient of coupling being approximately 0.60. Apart from this, to obtain the required vertical magnetic fields, the capacity and voltage of the auxiliary bank would have had to be increased, becoming very similar to those of the main bank. The difficulty of doing this, and the problem of three capacitor banks (preionizer, main and auxiliary banks) closely coupled together, making the operation of the Polytron less reliable, led us to abandon this scheme.

3.5 Diagnostic techniques used

A description of the different diagnostic techniques used to study the plasma is given. Electric probes, induced electric field and plasma current measurements are not included. The first two have already been described in the previous chapter. The plasma current was measured by a compensated Rogowski coil, whose risetime was less than 100 ns (Kilkenny, 1972).

3.5.1 Toroidal ion velocity

The method used measures Doppler shifts in emission lines from the plasma ions. The ion velocity v is obtained from

$$\frac{v}{c} = \frac{\Delta\lambda}{\lambda_o} \qquad 3.17$$

where c is the speed of light, $\Delta\lambda$ the wavelength shift and λ_o the emission wavelength of an ion at rest.

The wavelength shift can be obtained by splitting the emitted spectral line and comparing the two parts obtained. The method was originally described by Berezin (1963) and was used by Kilkenny (1972) in the Polytron. If the ratio of the difference to the sum of the signals is taken, it can be shown that this ratio depends solely on the line shift, provided the line width is determined by the instrument. In particular, for the case of a Gaussian profile this ratio can be calculated. Fig. 3.4 shows a Gaussian profile being split at a wavelength λ. The amplitude as a function of the shift $\Delta\lambda$ is given by

$$A(\Delta\lambda) = A_o\, e^{-\left(\frac{\Delta\lambda}{w}\right)^2} \qquad \Delta\lambda = \lambda - \lambda_o \qquad 3.18$$

where w is the line width.

The total line emission is given by

$$I = A_o \int_{-\infty}^{\infty} e^{-\left(\frac{\Delta\lambda}{w}\right)^2} d(\Delta\lambda) \qquad 3.19$$

The difference between signals corresponds to the shaded area under the curve. The ratio is given by

$$\text{Ratio} = \frac{I_A - I_B}{I_A + I_B} = \frac{\int_{-\Delta\lambda_s}^{\Delta\lambda_s} e^{-\left(\frac{\Delta\lambda}{w}\right)^2} d(\Delta\lambda)}{\int_{-\infty}^{\infty} e^{-\left(\frac{\Delta\lambda}{w}\right)^2} d(\Delta\lambda)} \qquad 3.20$$

where $\Delta\lambda_s$ is the value of the shift under consideration. Equation 3.20 represents the normalized error function. It is plotted in Fig. 3.4. It is very linear for displacements of up to 0.5 w. This was confirmed on calibration of the system with a known line.

The usual scheme, adopted by Kilkenny (1972) for his previous measurement on the Polytron, is to pass the plasma light through a monochromator. A silvered knife edge prism is placed in the output slit of the monochromator to split the line in two. The alignment of this

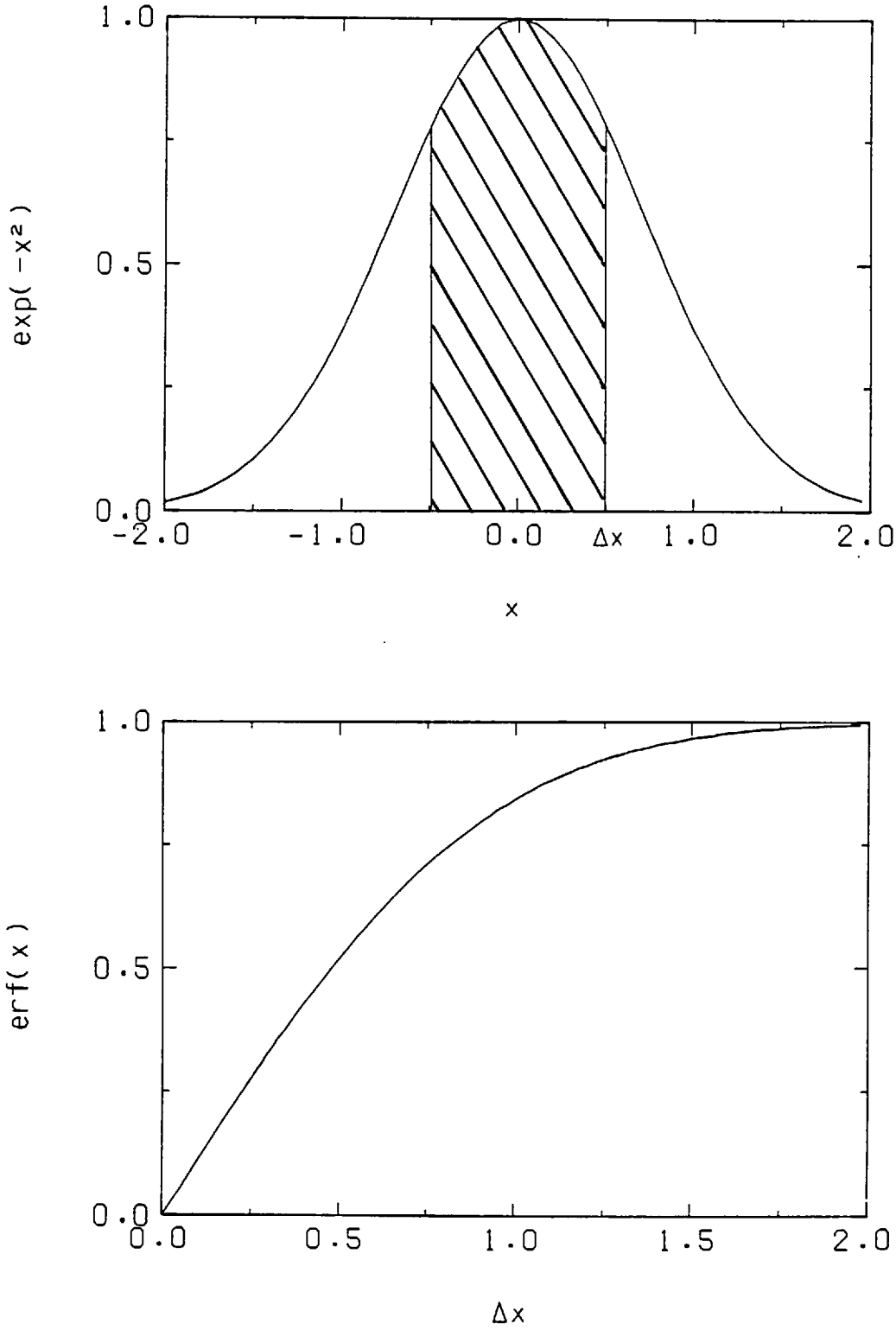

Fig. 3.4 Gaussian line profile and error function. For a gaussian profile the ratio given by Equation 3.20 is an error function.

system in which the silvered faces of the prism reflect light on to PM tubes is difficult.

The system used by the present author is shown in schematic form in Fig. 3.5. A transmitting spectrosil A knife-edge prism is used to split the spectral line. Transmission, rather than reflection, facilitates alignment, as the two rays are not widely divergent; but it can only be used if the aperture of the monochromator is sufficiently small. Otherwise reflection losses render the instrument non-linear.

A 50 mm focal length quartz lens is fitted at the back of the knife-edge prism to focus the split line onto the photocathodes of two miniature PM tubes (13 mm dia. side-on, Hamamatsu type R828). The whole assembly fits into a box 100 x 100 x 75 mm and is attached to the output slit of the monochromator. The prism is mounted on a fine adjustment slide carrier.

The monochromator used for this and other spectroscopic measurements is a 2 m Czerny-Turner type. It was built at Imperial College and was partly designed by the author. It has an f24 (with a grating 82 x 101 mm, 2160 lines/mm) aperture, Hilger-Watts input and output slits. The instrumental width is 0.07 Å.

Fig. 3.6 shows the arrangement used to collect light from the plasma along a tangential line of sight. A small front silvered mirror placed outside the quartz vessel reflects the light into the input slit. The nonuniformity of the quartz vessel walls is not a problem as the f-number is very large (f24).

The output from the PM tubes is taken into type CA plug-in units on a Tektronix 551 double-beam scope. The sum and difference signals are displayed on the two separate scope traces. The ratio is calculated manually.

3.5.2 Plasma position by optical means

The plasma position was obtained using (i) streak and framing photography; (ii) PIN photodiode array, and (iii) spectroscopic techniques.

(i) The image converter camera used for those experiments where an independent capacitor bank generated the vertical magnetic field

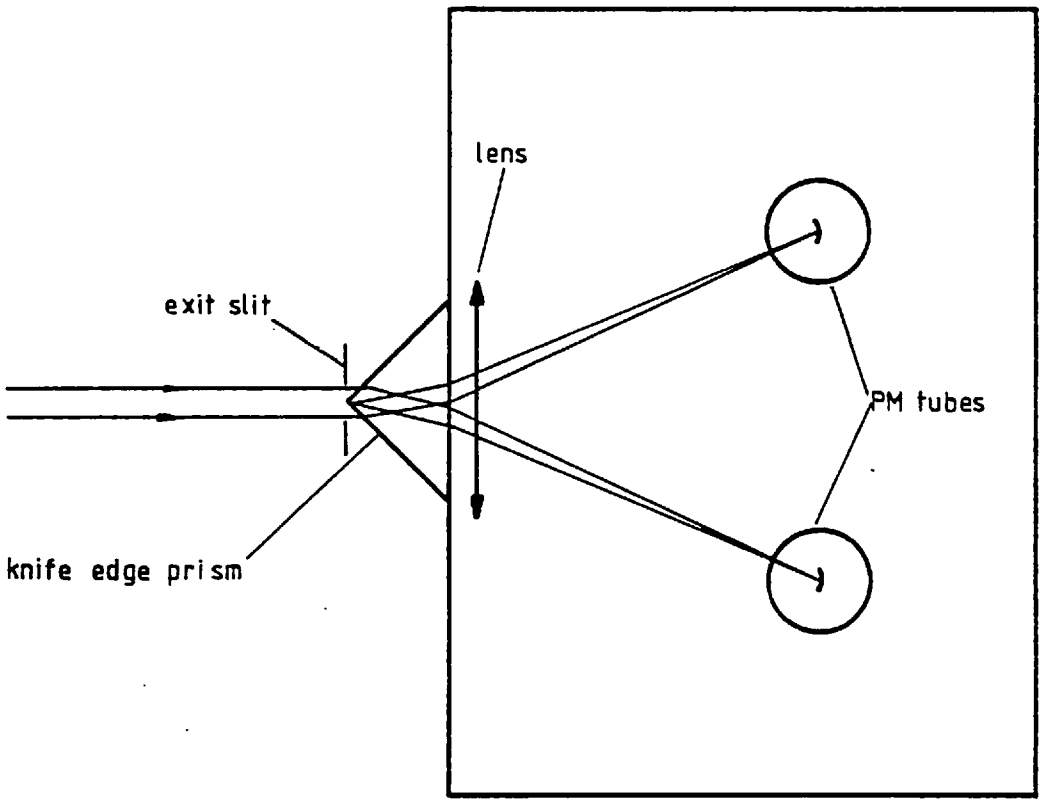

Fig. 3.5 Schematic drawing of the knife-edge prism and PM tube box used to split the spectral line emission. Ray tracing of the light from the monochromator is shown in thin lines.

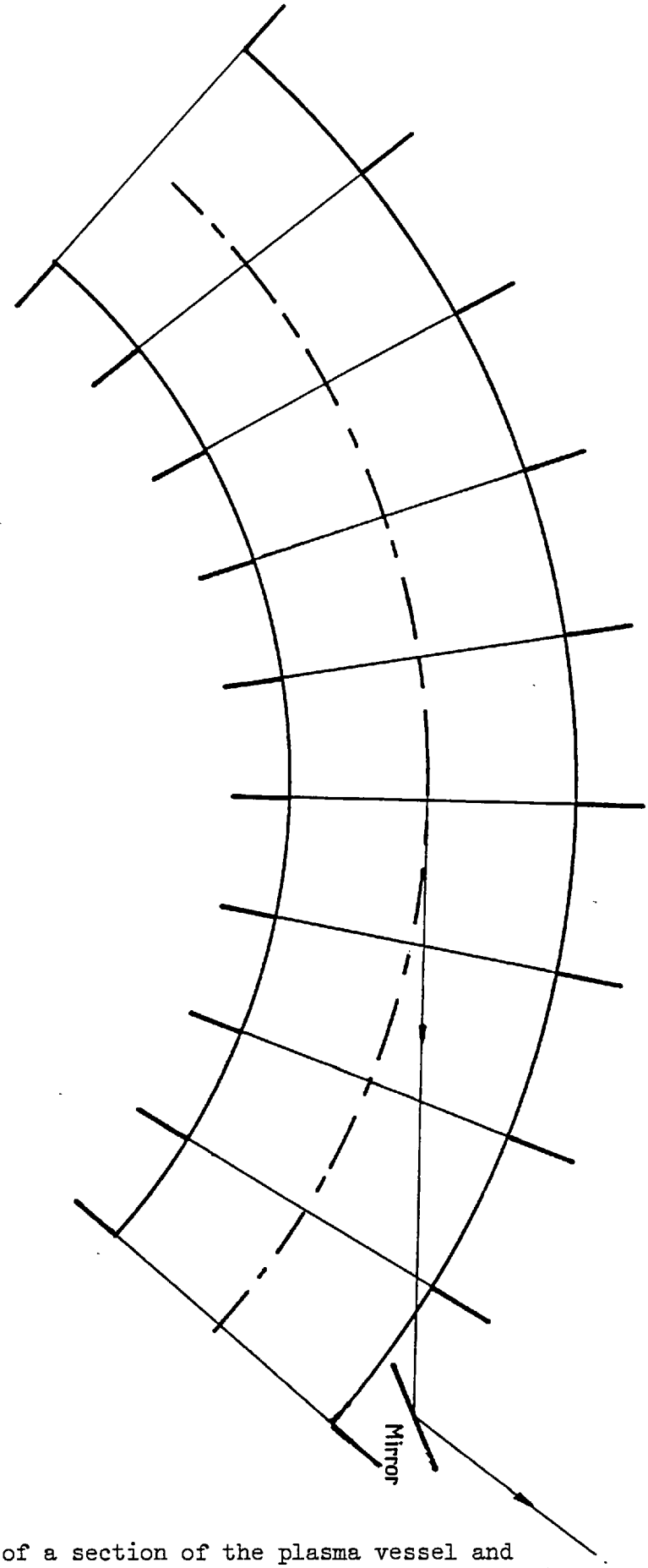

Fig. 3.6 Schematic diagram of a section of the plasma vessel and position of the external mirror used to obtain tangential line of sight view.

was an STL camera, lent by Culham Laboratory. The one used for the other case is a Hadland Ima-Con camera, lent by the Applied Optics Group at Imperial College. Image converter cameras have a restricted dynamic range, particularly if used with fast Polaroid film. The spectral response of the cameras used was very limited, having no UV sensitivity. The argon plasma in the Polytron emits mainly in the UV region of the spectrum. The information about plasma motion obtained with image converter cameras is limited to large scale motion.

(ii) In order to improve this situation a linear PIN photodiode array was built. The photodiodes used (Monsanto MD2) have a limited UV response (10% of peak sensitivity) and are very linear. Their dynamic range extends over seven orders of magnitude. The array consists of eight photodiodes, 5 mm between centres. The output from each photodiode is fed into a 500 series Tektronix scope channel. A quartz lens is used to image the plasma onto the array. This allows determination of plasma position for each shot.

(iii) Position was also determined by looking at line emission from the plasma. The main advantage of this method is that it allows determining the position of regions in the plasma with a large proportion of higher ionization states. The line emission from these higher ionization states is in the UV region of the spectrum which cannot be detected by the other two methods described. The main disadvantage of this method is that it is a multiple shot technique and is dependent on reproducibility of the discharge. In the results to be presented an average over a large number of shots was taken to overcome this problem.

3.5.3 Plasma position determined by magnetic coils

The position of a current carrying conductor can be determined by measuring the magnetic field produced by the current at a distant point. A more sensitive scheme is to measure the magnetic field at either side of the conductor and take the difference. The method devised is essentially that, but instead of having two separate coils a single one is used equivalent to a pair. Fig. 3.7 shows a schematic drawing of one of the coils used. It is wound in such a way as to be equivalent to a rectangle coplanar with the plasma channel. The total flux through the coil produced by the plasma is the difference of the fluxes at either

side of the plasma channel. Two such coils at 90° to each other are used to determine horizontal and vertical plasma position.

For the coil used to measure the horizontal position, the total flux linked is given by

$$\phi_c = \frac{\mu_o w_c I}{\pi k_1}\sqrt{\frac{a_1}{R}}\left[(1-\frac{k_1^2}{2})K - E\right] - \frac{\mu_o w_c I}{\pi k_2}\sqrt{\frac{a_2}{R}}\left[(1-\frac{k_2^2}{2})K - E\right] \qquad 3.22$$

where $k_i = \sqrt{\frac{4a_i R}{(a_i + R)^2}}$, the plasma radius is R, the radii of the coil-sides parallel to the plasma are a_1 and a_2, w_c is the coil width and I the plasma current.

Fig. 3.8 shows the ratio ϕ_c/I for horizontal and vertical position coils. An experimental check on this calculation was made using a conductor of the same diameter as the plasma threaded through the coils. A small capacitor bank was discharged through this conductor. The position determined with the coils agrees well with position measured directly. It is within the experimental error (5%). The horizontal coil is fairly insensitive to vertical displacement. A 3 cm vertical displacement produces a change of 5% on the ratio ϕ_c/I.

The horizontal coil links flux produced by the induction rods. The plasma signal is up to 30% of the vacuum signal. To obtain plasma position the difference of signals with and without the plasma is used.

3.5.4 Line intensity and broadening

These measurements were done using the monochromator already described, on AI (5650 Å), AII (4426 Å), AIII (3336 Å) and AIV (2809 Å). Higher ionization levels emit in the VUV region of the spectrum and are thus inaccessible with the monochromator available.

Spatial distributions of the total intensities of the different spectral lines give information about plasma position, density and electron temperature.

Broadening on the other hand can give information about ion temperature or electron density, depending on the dominant mechanism involved. Natural line width, Stark and Doppler broadening should be considered. The natural line width is small compared with the widths due

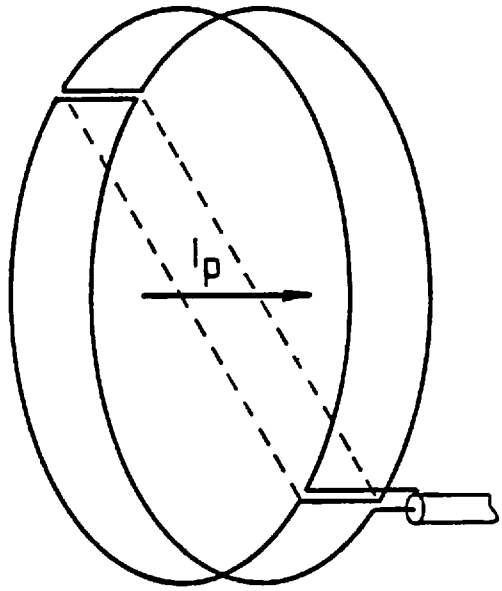

Fig. 3.7 Schematic diagram of a coil used to determine plasma position. The plane P for which the coil is most sensitive to plasma displacement is shown. Also shown is the plasma current position relative to the coil.

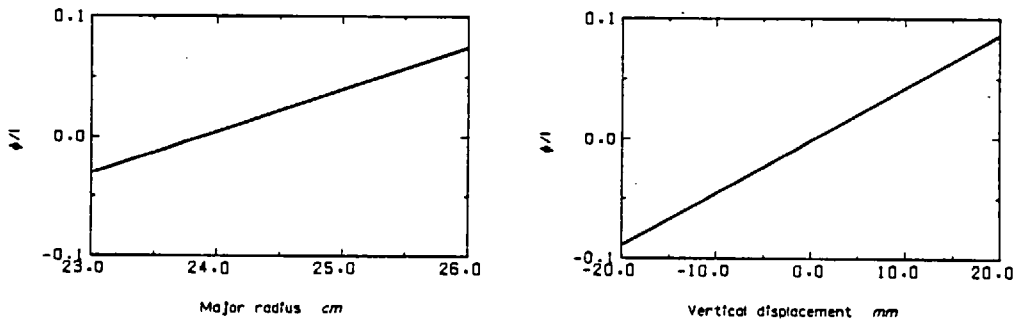

Fig. 3.8 Calibration of coils used to determine plasma position

to these two broadening processes. The value of AII Stark broadening has been calculated by Griem (1964) and the value given for the AII line used and $n_e \sim 4 \times 10^{20} m^{-3}$ is 2.5×10^{-4} Å with an electron temperature of 8 eV. According to Griem Stark broadening of higher ionization levels should be smaller than the values obtained for AII. Most of the broadening measurements were done in AIV. In order to make sure that Doppler broadening is the dominant mechanism, the line profiles at two densities were obtained. The results in Fig. 3.9 show that the higher density gives the narrower profile. Stark broadening is strongly dependent on density, increasing with density. The results obtained have therefore been interpreted as Doppler broadening, with higher density giving lower particle energy.

The minimum temperature that can be obtained from the measurement is limited by the instrumental width of 0.07 Å. The minimum temperature for AIV ions (λ = 2809 Å) is 4 eV obtained from

$$kT = \frac{mc^2}{4 \ln 2} \left(\frac{w_\lambda}{\lambda_o} \right)^2 \qquad 3.23$$

where m is the ion mass, w_λ the measured width and λ_o is the centre line wavelength, T in ^oK.

3.5.5 The accelerating force on the plasma

The azimuthal and toroidal components of Ohm's law are

$$\begin{aligned} j_\theta &= \sigma(E_\theta + v_\phi B_r - j_\phi B_r/ne) \\ j_\phi &= \sigma(E_\phi - v_\theta B_r + j_\theta B_r/ne) \end{aligned} \qquad 3.24$$

where j_r, v_r, B_θ and ∇p have been assumed equal to zero. E_ϕ is the applied electric field and E_θ is the field induced by the Hall currents, the cusp field being essentially constant.

Equation 3.22 can be expressed as

$$\begin{aligned} j_\theta &= \frac{\sigma}{1 + \omega^2\tau^2} (E_\theta - \omega\tau E_\phi + v_\phi B_r + \omega\tau v_\theta B_r) \\ j_\phi &= \frac{\sigma}{1 + \omega^2\tau^2} (E_\phi + \omega\tau v_\phi B_r - v_\theta B_r + \omega\tau E_\theta) \end{aligned} \qquad 3.25$$

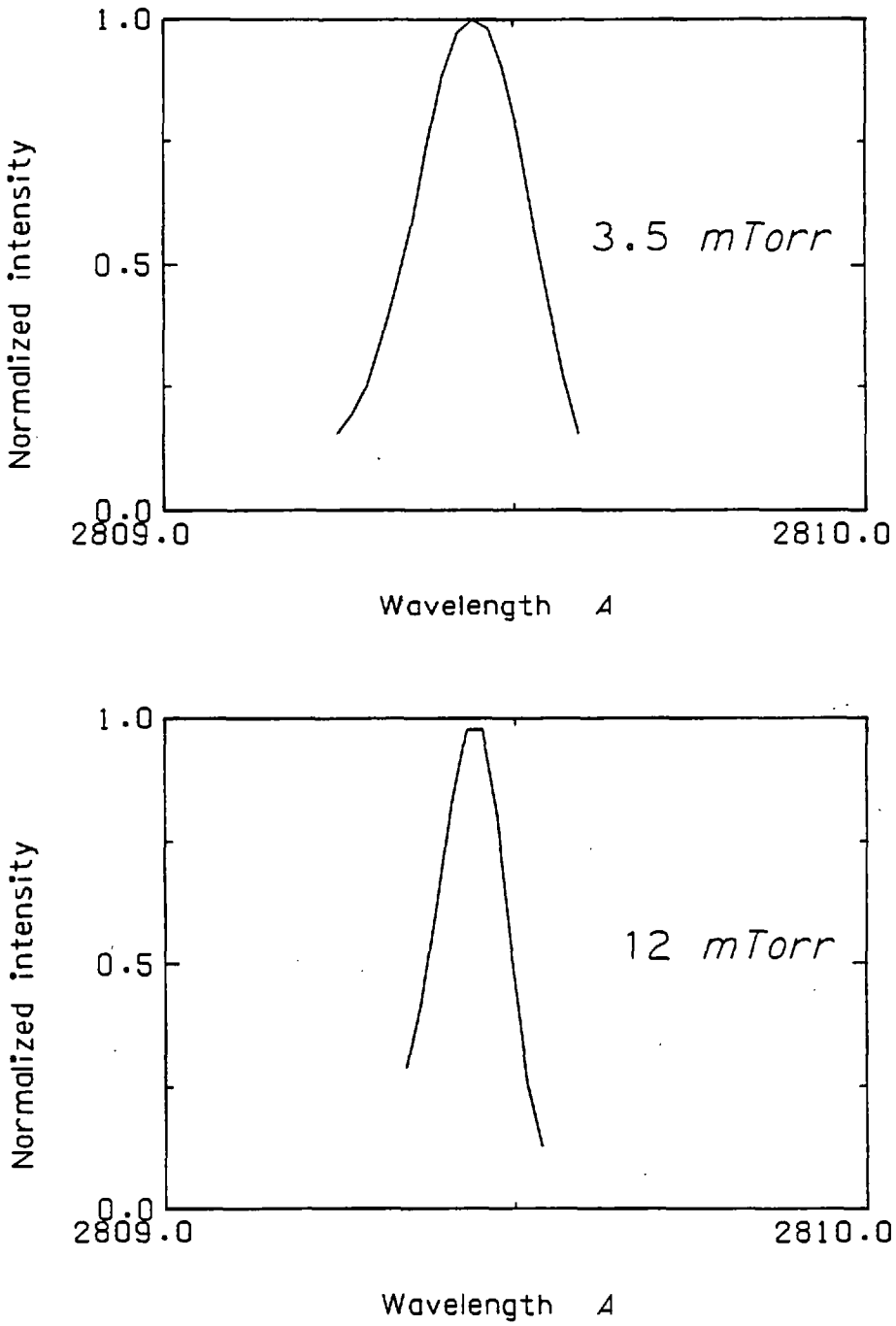

Fig. 3.9 AIV line profiles for 3.5 and 12 mTorr filling pressure, V_m = 10 kV, V_c = 1.5 kV, at t = 2 μs.

where $\omega\tau = \frac{\sigma B_r}{ne}$ is the Hall parameter and n the electron number density. Initially v_θ and v_ϕ are small, and assuming that E_θ is small compared to $\omega\tau E_\phi$, which is valid for large $\omega\tau$, we have

$$j_\theta = - \frac{\omega\tau}{1 + (\omega\tau)^2} \sigma E_\phi \qquad 3.26$$

For large Hall parameter

$$j_\theta = ne \frac{E_\phi}{B_r} \qquad 3.27$$

The accelerating force per unit volume on the plasma is then

$$F_\phi = j_\theta B_r = - ne E_\phi \qquad 3.28$$

An equal and opposite reaction force is exerted on the cusp coils. Thus a measurement of this reaction force makes possible a determination of the accelerating force. The reaction force can be obtained by measuring the magnetic field components over a surface enclosing the plasma and calculating the Maxwell stress tensor. Etherington (1965) has done this in a linear Hall accelerator. In the Polytron, because of symmetry this needs to be done only along a line equal in length to the cusp separation (Kilkenny, 1972), requiring at least two simultaneous magnetic field measurements.

An alternative approach, used in the present work, is to obtain the magnetic field produced by the plasma on a cusp coil and the current flowing through it. The force on the cusp coil is the product of the two. The force exerted on a closed conductor by a magnetic field is given by

$$\underline{F} = \oint I \, d\underline{l} \times \underline{B} \qquad 3.29$$

where I is the current flowing through the conductor, $\underline{B}$ the magnetic field and $d\underline{l}$ a vector length element along the conductor considered. On a cusp coil Equation 3.29 becomes

$$F_\phi = I \oint b_r \, dl \qquad 3.30$$

where b_r is the radial magnetic field produced by the Hall currents.

The cusp coil current is not affected by the plasma, as the plasma currents are much smaller than the currents in the coils. Thus to obtain the force a measurement of the integrated radial magnetic field at the

cusp coil position is required. This was done using the coil illustrated in Fig. 3.10. This coil is positioned underneath a cusp coil in such a way as to give null signal with no plasma present.

The output signal from this coil after integration is given by

$$V_o = \frac{w \oint b_r dl}{RC} \qquad 3.31$$

where w is the coil width, R and C the integrating resistance and capacitance. Equation 3.31 holds provided RC is much longer than times of interest.

The cusp coil current has to be measured once for each cusp bank charging voltage. After that it becomes possible to determine the force on a cusp coil and hence the accelerating force on the plasma with one measurement. This is a clear advantage over other methods used. A further advantage is that the result does not depend on the spatial distribution of Hall current.

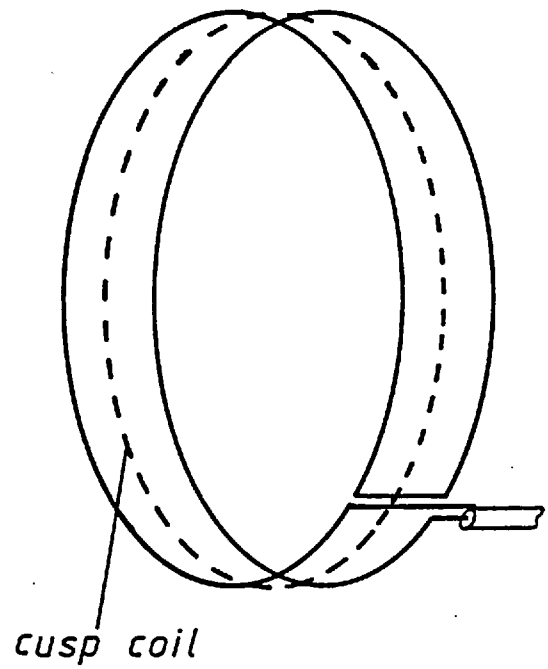

Fig. 3.10 Coil used to obtain $\oint b_r dl$ from which the accelerating force is calculated.

3.5.6 Faraday cup probe

A Faraday cup collector probe was used to study plasma losses. A Faraday cage structure decreases secondary emission (Simpson, 1961). A schematic diagram of the probe is shown in Fig. 3.11. The collector electrode and outer casing are made out of stainless steel. The front is a Ni foil with a 50 μm pinhole in the centre. The distance between the front electrode and the collector is kept to a minimum (0.3 mm) to avoid secondary ionization of the background gas inside the probe (Bakulin et al., 1969). The product pressure times electrode separation has to be smaller than a given constant. The electrode spacing used allows satisfactory operation at 3.5 mTorr filling pressure, ceasing to operate at pressures above 6 mTorr. The front electrode can be biased positive or negative to collect electrons or ions.

3.5.7 Internal magnetic probes

Attempts were made to measure magnetic fields with internal magnetic probes. The probes designed by Parkinson (1968) were used. It became apparent that the results obtained were probably due to surface effects on the probe. This can be expected, as the vertical magnetic field allows a higher plasma temperature for longer times. Coating the probe with ceramic coating (Ceramacoat) did not improve the situation. This type of measurement was therefore abandoned.

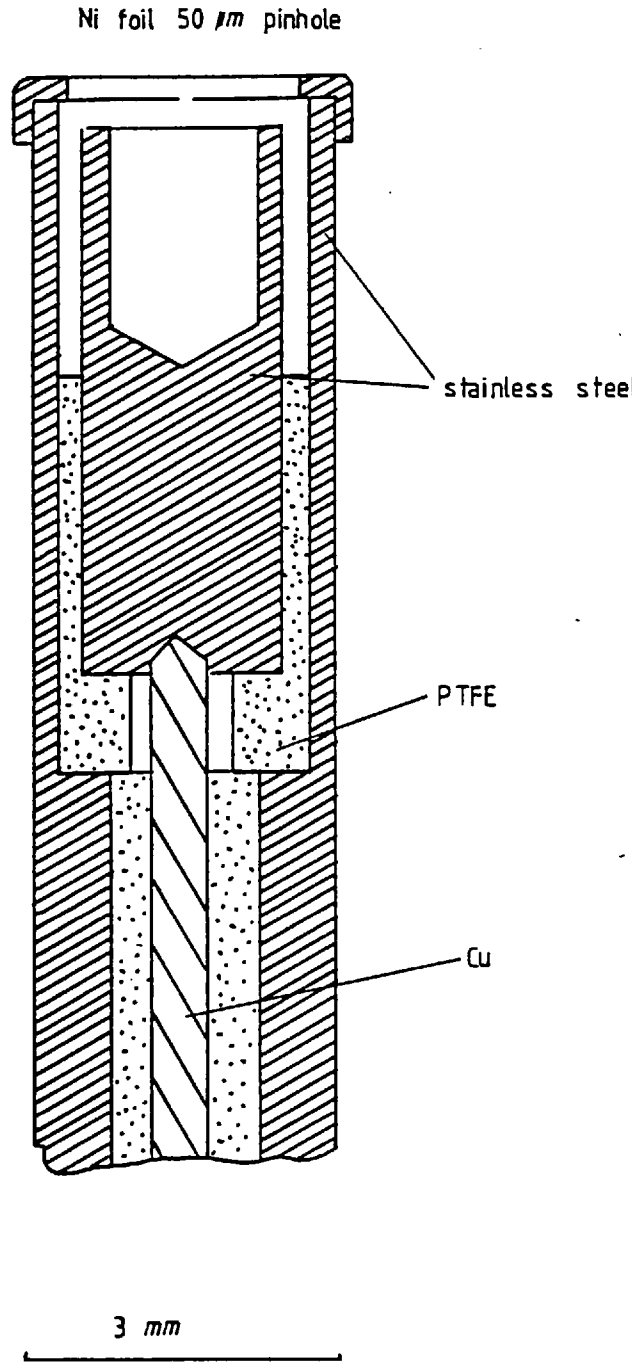

Fig. 3.11 Schematic diagram of the Faraday cup probe.

Chapter 4

EXPERIMENTAL OBSERVATIONS

In this chapter the results obtained with the diagnostic techniques described in the previous chapter are presented. These results are analysed in the following chapter. All measurements are in Argon, and unless otherwise stated they are at 3.5 mTorr filling pressure, 1.5 kV cusp bank charging voltage.

4.1 Diagnostics on independently driven vertical magnetic field

The diagnostics used in this configuration were plasma current recording and image converter camera photography. The vertical magnetic field was generated in this case by an auxiliary capacitor bank, as described in Section 3.4.

Fig. 4.1 shows streak photographs and plasma current traces with and without vertical magnetic field. In this case the auxiliary bank is fired simultaneously with the main bank. Streak photographs are obtained with a slit next to a cusp coil looking vertically up from under the plasma vessel. Major radius increases to the left. The vertical magnetic field prevents significant wall interaction as can be seen in the streak photographs. The peak plasma current is seen to increase. This is probably due to larger Hall acceleration and electron current as the plasma remains near the magnetic axis.

Fig. 4.2 shows framing camera photographs and plasma current for a situation where the auxiliary bank was fired earlier than the main bank. This was required because the magnetic field obtained initially was not large enough to prevent the outward radial drift. Firing the auxiliary bank earlier than the main bank ensured that the vertical magnetic field was large enough when the main bank was discharged. Framing camera photographs show that there was no large scale wall interaction in this case. The plasma current obtained indicated that the auxiliary bank induces a small plasma current (about 10% of the peak plasma current). The plasma current induced by the main bank discharge shows no indication of the usual 'shoulder' associated with the initial loss. This initial

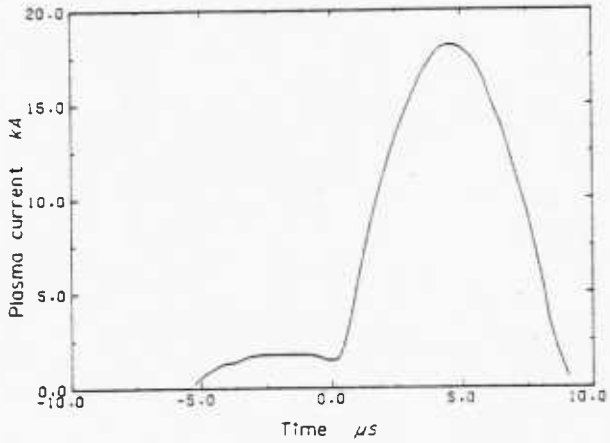

Fig. 4.2 Framing camera photographs and plasma current with vertical magnetic field generated by auxiliary capacitor bank fired 6 μs earlier than the main bank. No major plasma wall interaction is observed. V_m = 10 kV, V_c = 1.5 kV, p = 3.5 mTorr, STL image converter camera.

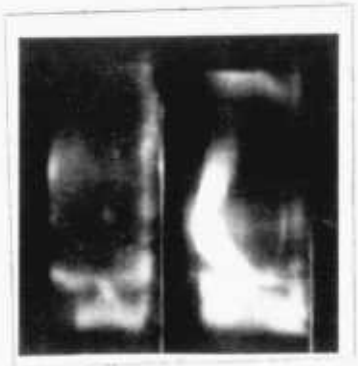

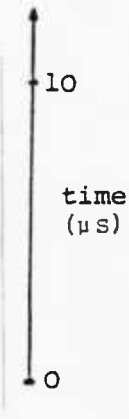

vertical magnetic field on off

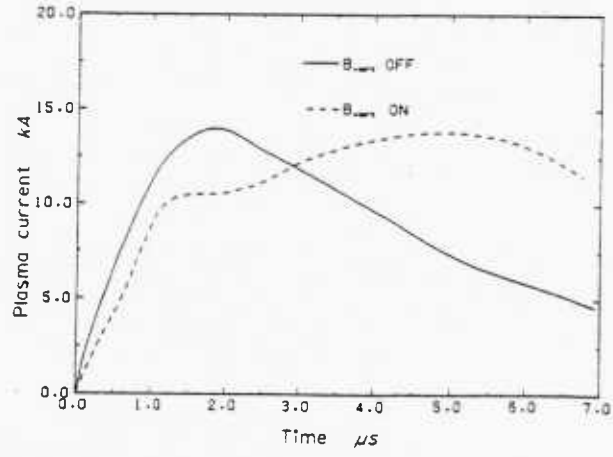

Fig. 4.1 Streak photographs and plasma current with and without vertical magnetic field generated by an auxiliary capacitor bank triggered at the same time as the main bank. The outer vessel wall is to the left, the peak vertical magnetic field is 0.02T, V_m = 20 kV, V_c = 1.5 kV, p = 3.5 mTorr. Intense light emission from the wall is observed for the case with no vertical magnetic field. (STL image converter camera)

loss has been described by Kilkenny (1972). He showed that the initial loss volume, the plasma region from which lost ions originate, decreases with increasing electric field. In this case a small electric field is induced by the auxiliary bank, several microseconds before the main accelerating field is applied. During this time the particles in the initial loss volume for the small field are lost. At the time the main accelerating field is applied there are no particles left in the loss region for this value of electric field.

4.2 Plasma current and induced voltage

A wide range of conditions has been investigated: cusp bank voltages 1.0 to 2.5 kV; main bank voltages 10 to 25 kV; and filling pressures 2 to 25 mTorr. The vertical magnetic field is obtained from additional induction rods driven by the main bank. Fig. 4.3 shows current and voltage traces for typical conditions. Current traces have fairly fast risetime, a 'shoulder' associated with the initial loss and a later stage with a final decay. The total timescale is of the order of 8 μs. The peak plasma current is higher with a vertical magnetic field applied.

The induced voltage has a very fast initial risetime, a slower increase associated with the fast current risetime, becoming very close to a cosine dependence at later times. The induced voltage at later times is very similar to the vacuum induced voltage.

Fig. 4.4 shows a plot of the ratio of initial to vacuum voltage as a function of pressure.

4.3 Accelerating force

The vertical magnetic field has a marked effect on the accelerating force, as is demonstrated in Fig. 4.5. The force has a fairly fast risetime (~ 100 ns), followed by a nearly constant phase and then during the initial loss the force decreases or vanishes; it reappears for a few microseconds for lower pressures only, if B_{vert} is zero.

The force has been determined for a wide range of conditions. Its value at t = 0.5 μs, before the initial loss, is given in Fig. 4.6 for different conditions. For low filling density the force is seen to be

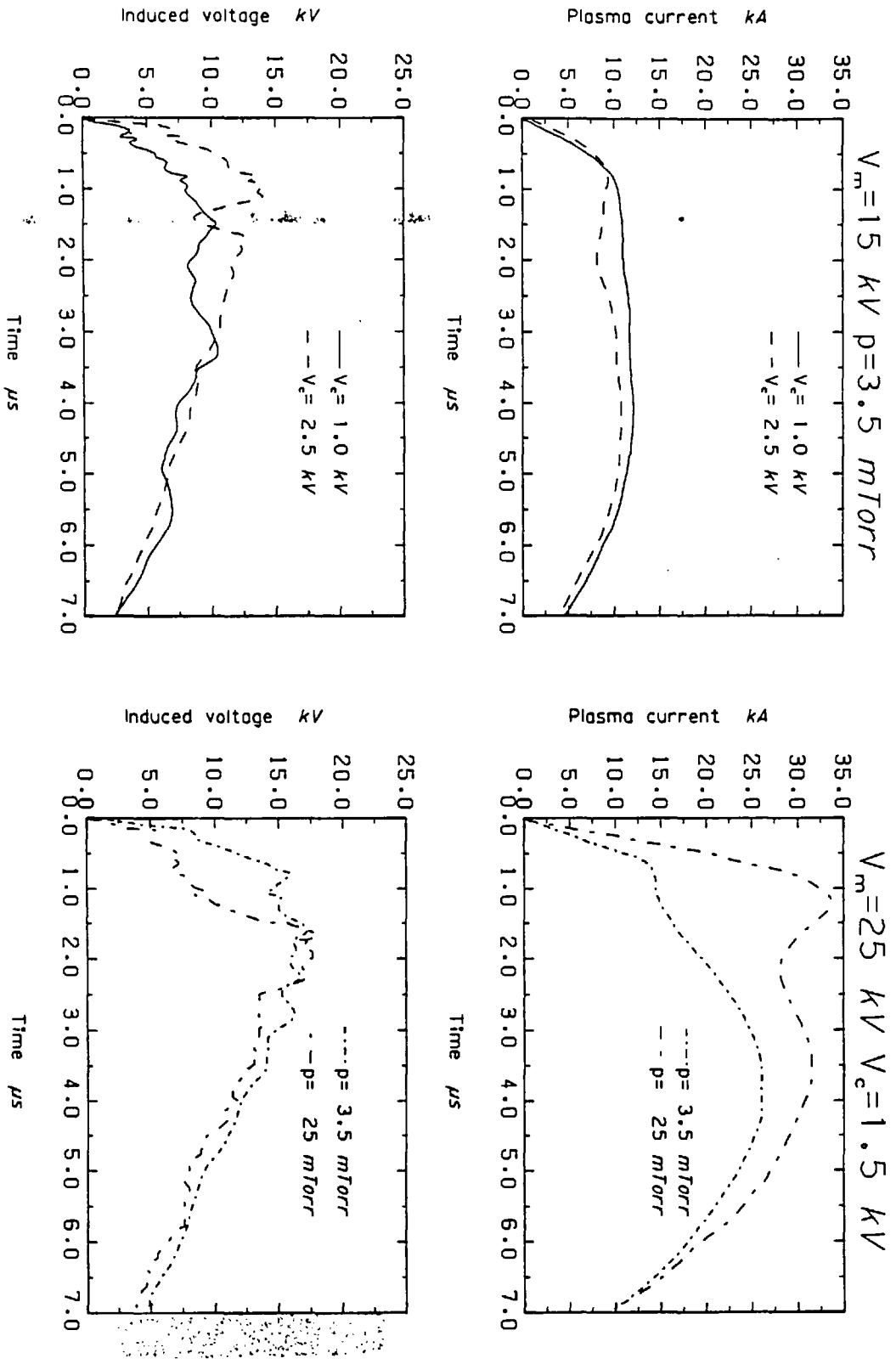

Fig. 4.3 Induced voltage and plasma current for different conditions.

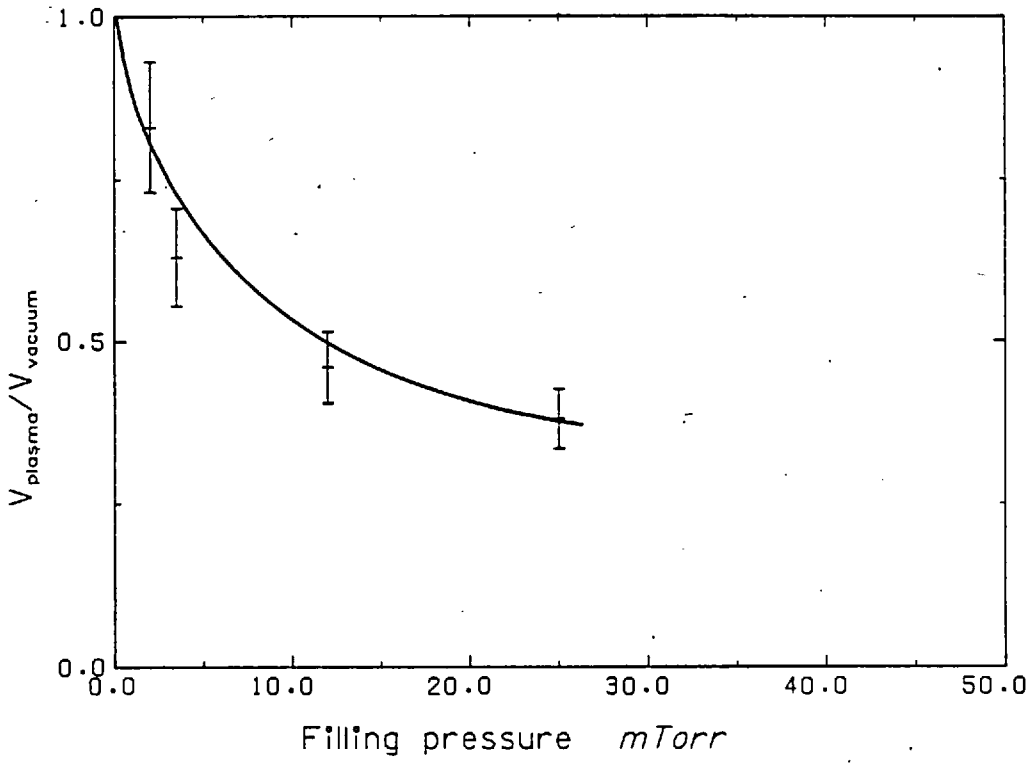

Fig. 4.4 Ratio of initial induced voltage (t = 200 ns) to vacuum induced voltage as a function of filling pressure. V_m = 20 kV, V_c = 1.5 kV.

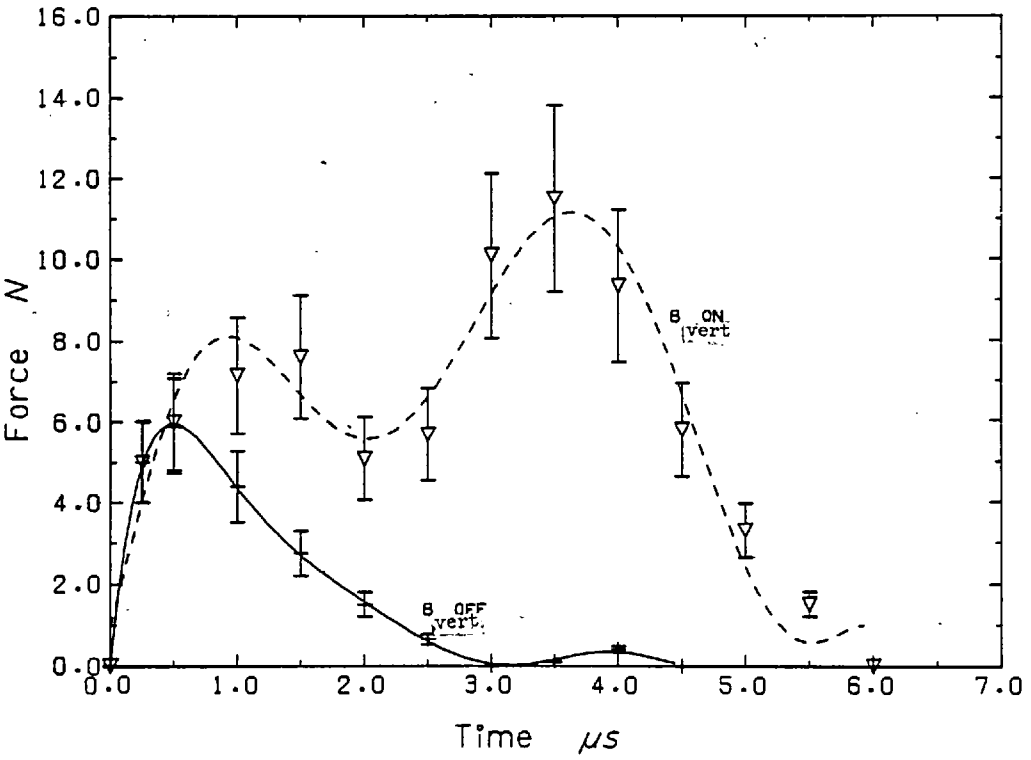

Fig. 4.5 Plasma accelerating force as a function of time, V_m = 10 kV, V_c = 1.5 kV, p = 3.5 mTorr. B_{vert} on and off.

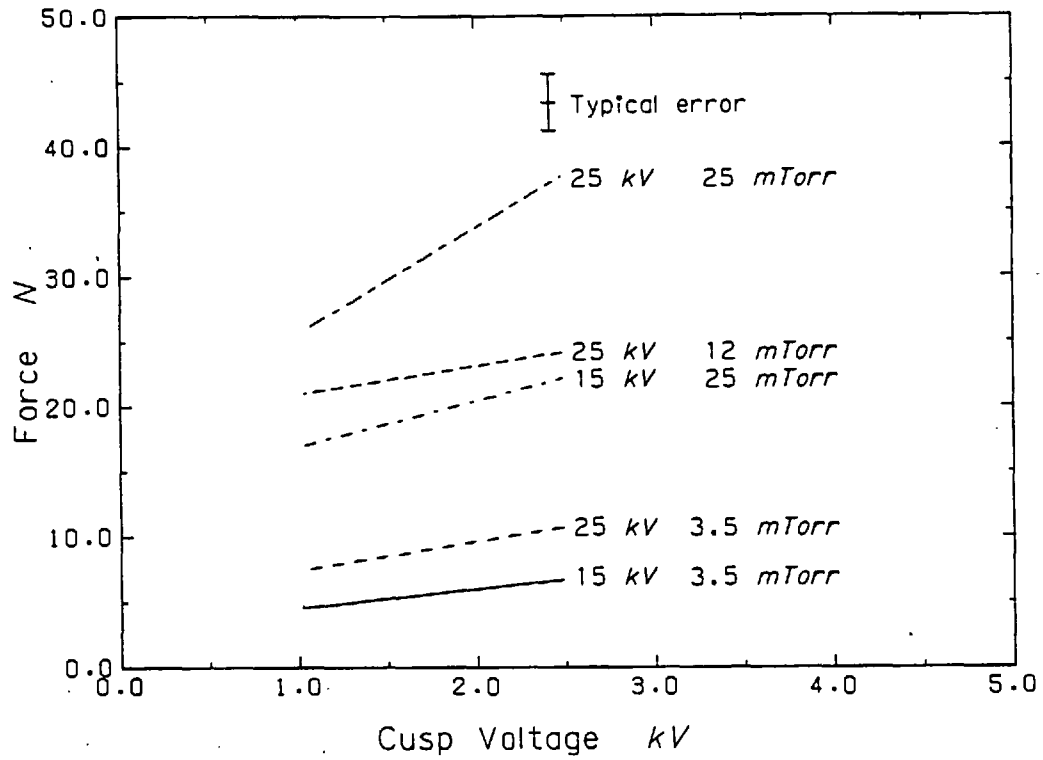

Fig. 4.6 Plasma accelerating force as a function of cusp voltage at t = 0.5 μs.

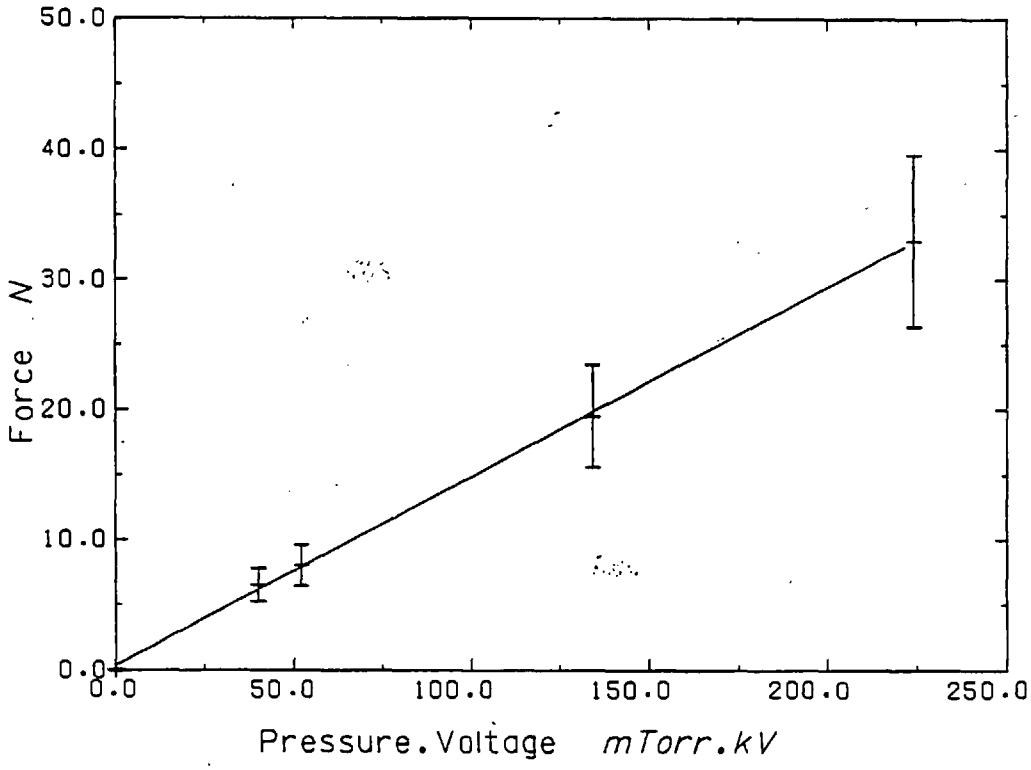

Fig. 4.7 Plasma accelerating force as a function of the product filling pressure and induced voltage, V_m = 25 kV, V_c = 1.5 kV at t = 0.25 μs.

essentially independent of cusp magnetic field. Fig. 4.7 gives the force at 0.5 μs against the product of filling pressure and induced voltage. A linear dependence is exhibited.

Fig. 4.8 gives the force as a function of time for different cusp and main bank voltages. It is interesting to note that the force time-scale decreases with increasing accelerating voltage and shows a slight increase with cusp field.

4.4 Toroidal ion velocities

Toroidal ion velocities have been measured for a fairly wide range of conditions. Most of the measurements are based on AIV line emission. Fig. 4.9 shows the results obtained for different main bank voltage. It is worth noting that at later times velocities are smaller for the highest main bank voltages. Fig. 4.10 shows ion velocities for AIII and AIV ions for one particular case.

4.5 Spectral line intensities

The highest ionization level studied is AIV, as higher ionization states have their strong emission lines in the VUV or soft X-ray wavelength region. However, it seems probable that there is little emission at higher levels as this would imply higher temperatures, in disagreement with other diagnostics. Results have been obtained looking tangentially, giving a line of sight integrated emission and looking radially in. For radial emission measurements a cusp was selected where the quartz vessel wall was most uniform.

Fig. 4.11 shows results with tangential viewing for two main bank voltages. AIV emission lasts longer for the lower voltage case.

Results for the case of radial line of sight are summarized in Fig. 4.12 for one of the conditions studied. Intensities have been normalized to the maximum value for each line. The plots have been obtained by utilizing an ICCC (Imperial College Computer Centre) library program (Monro, 1977) generating the results in microfilm. Each box is the intensity distribution for a particular spectral line at a particular time, indicated on the left hand side, in microseconds. Right and left

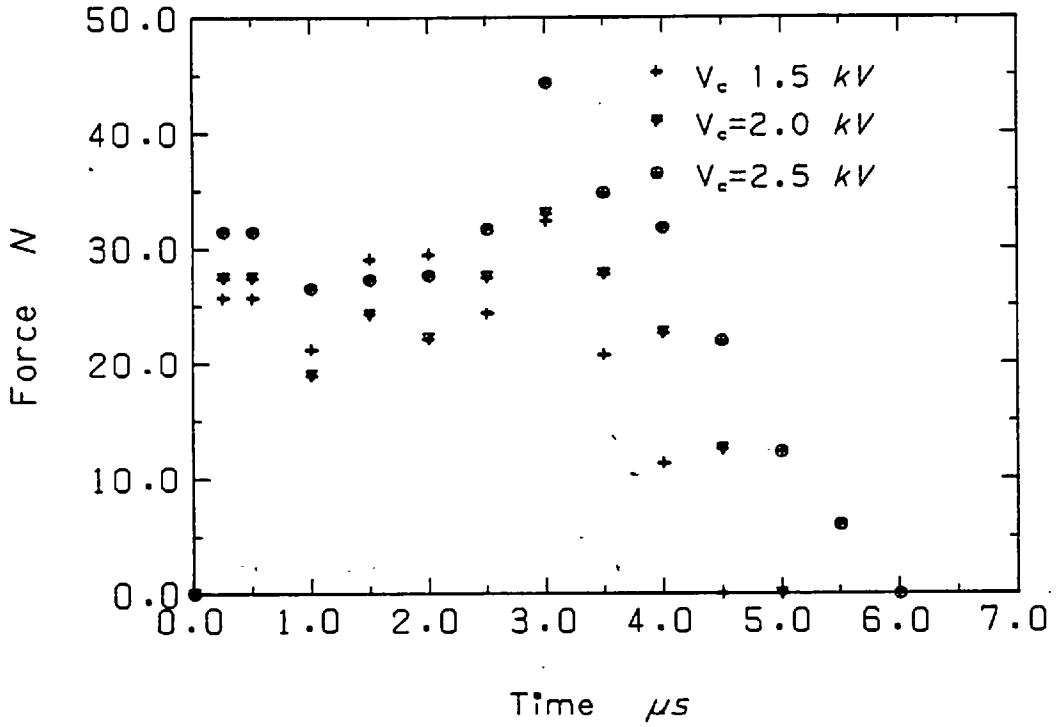

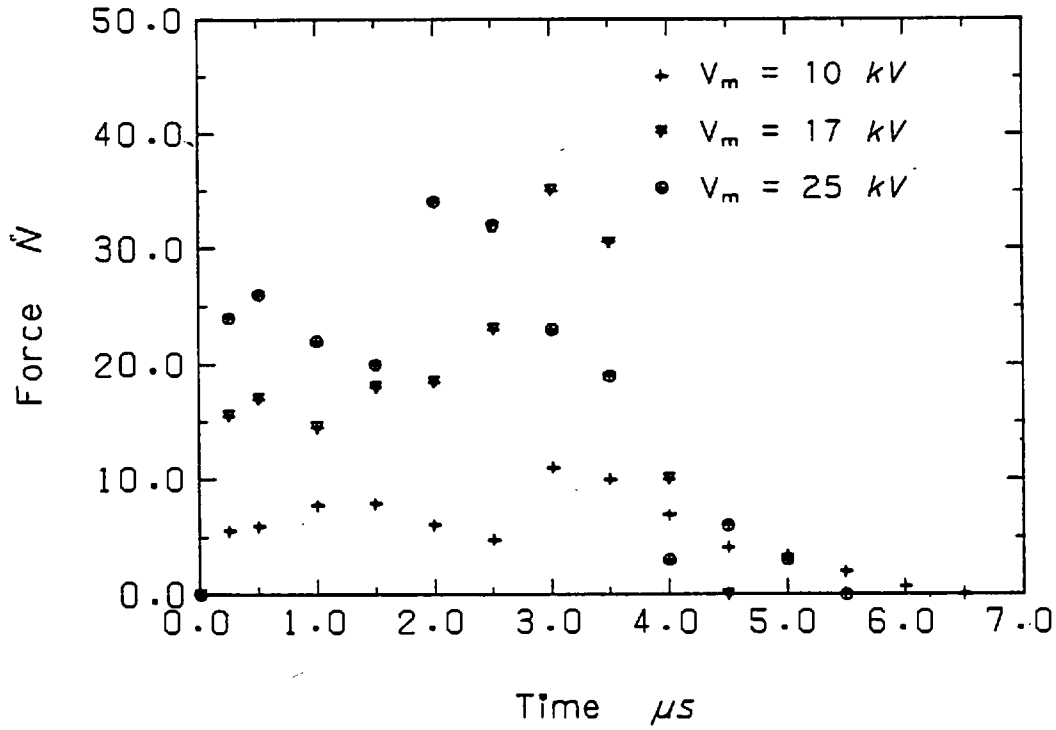

Fig. 4.8 Plasma accelerating force as a function of time for (a) different cusp voltages, V_m = 17 kV, p = 3.5 mTorr; (b) different main bank voltages, V_c = 1.5 kV, p = 3.5 mTorr.

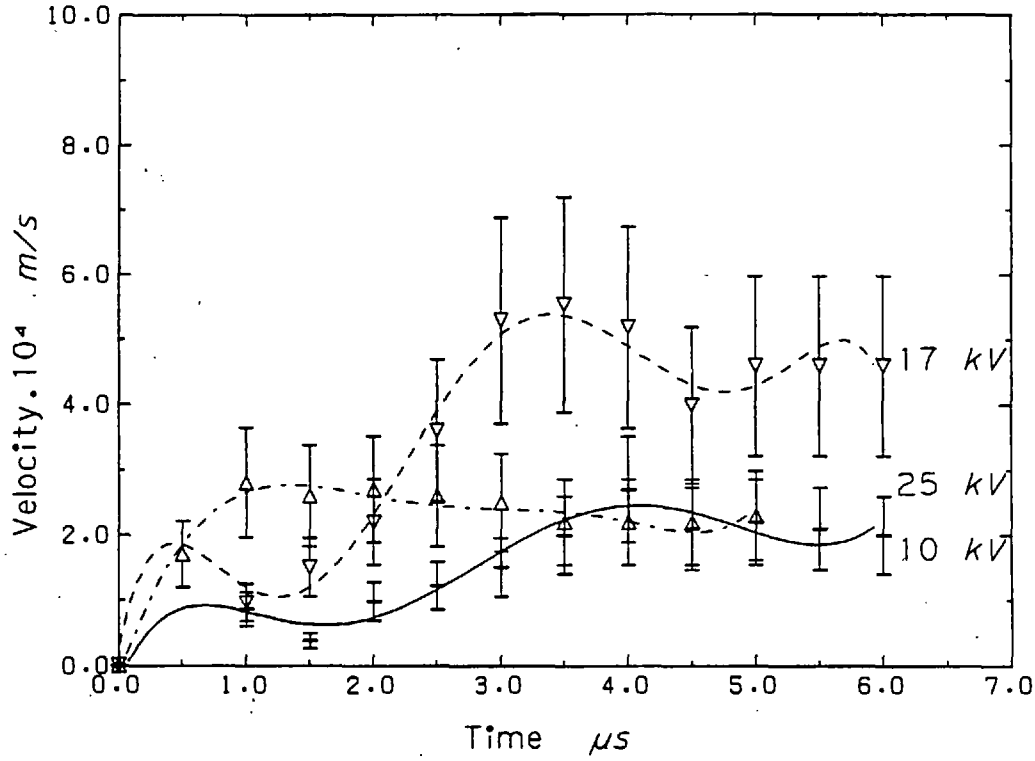

Fig. 4.9 Toroidal ion velocity as a function of time for V_c = 1.5 kV, p = 3.5 mTorr, V_m = 10, 17 and 25 kV. B_{vert} = .02 x V_m gauss.

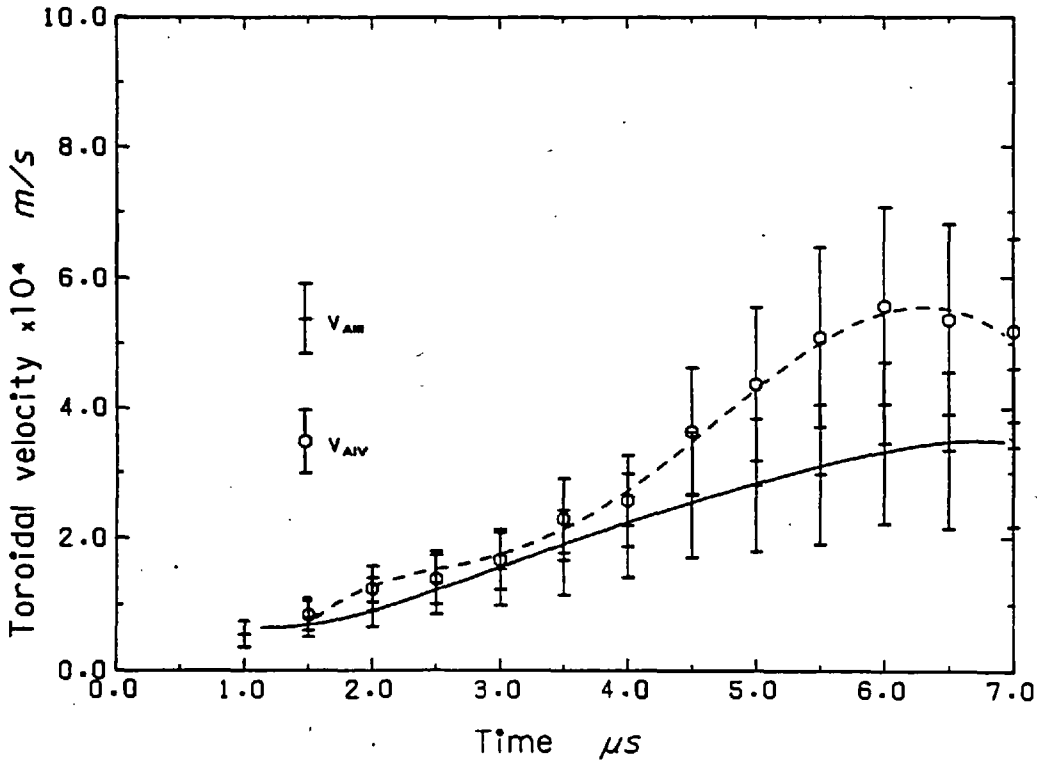

Fig. 4.10 AIII and AIV ion toroidal velocities. V_m = 10 kV, V_c = 1.5 kV, p = 3.5 mTorr, B_{vert} = 362 gauss.

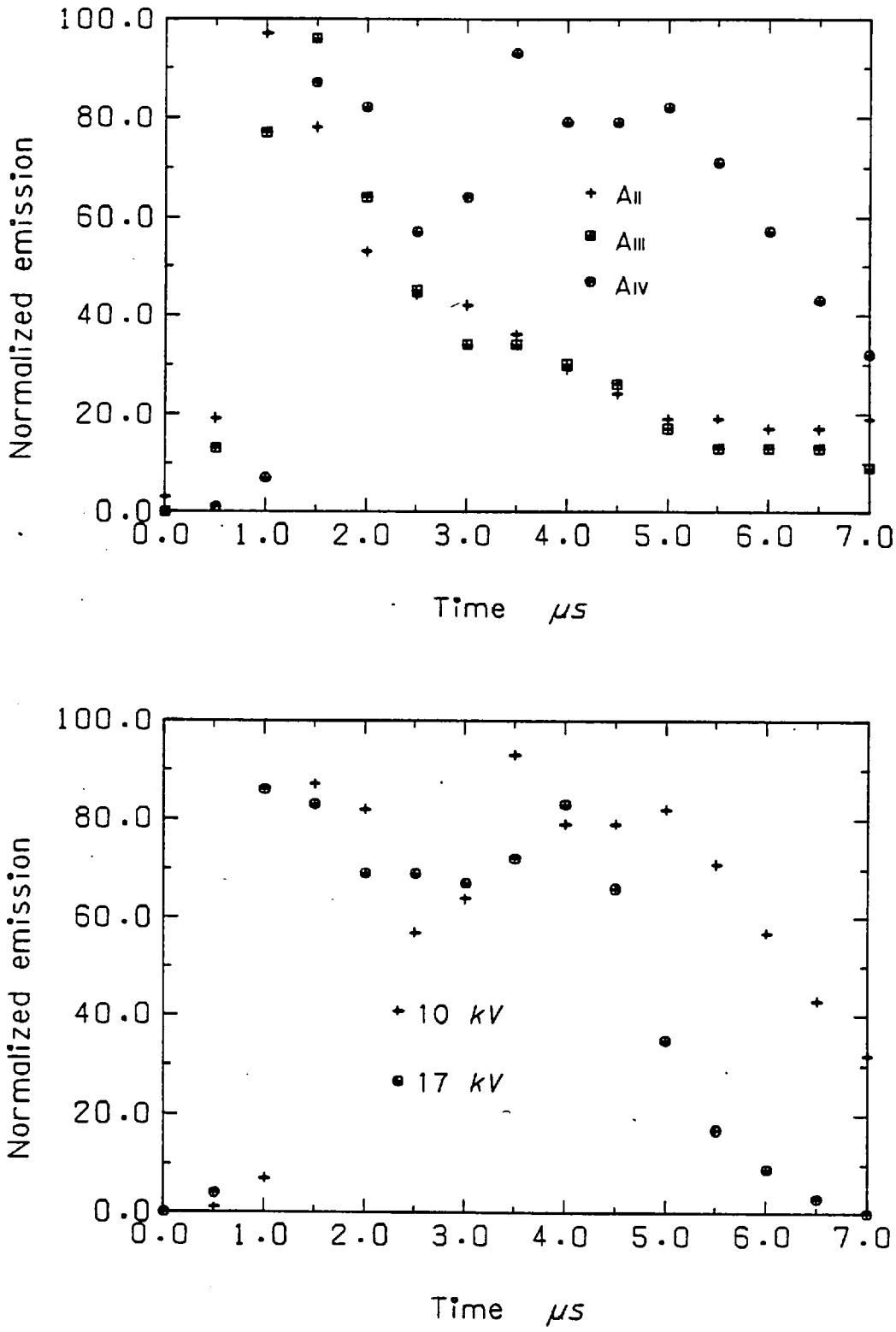

Fig. 4.11 Normalized line emission, tangential line of sight. (a) AII, AIII and AIV emission for V_m = 10 kV, V_c = 1.5 kV, p = 3.5 mTorr; (b) AIV emission for V_m = 10 and 17 kV, V_c = 1.5 kV, p = 3.5 mTorr.

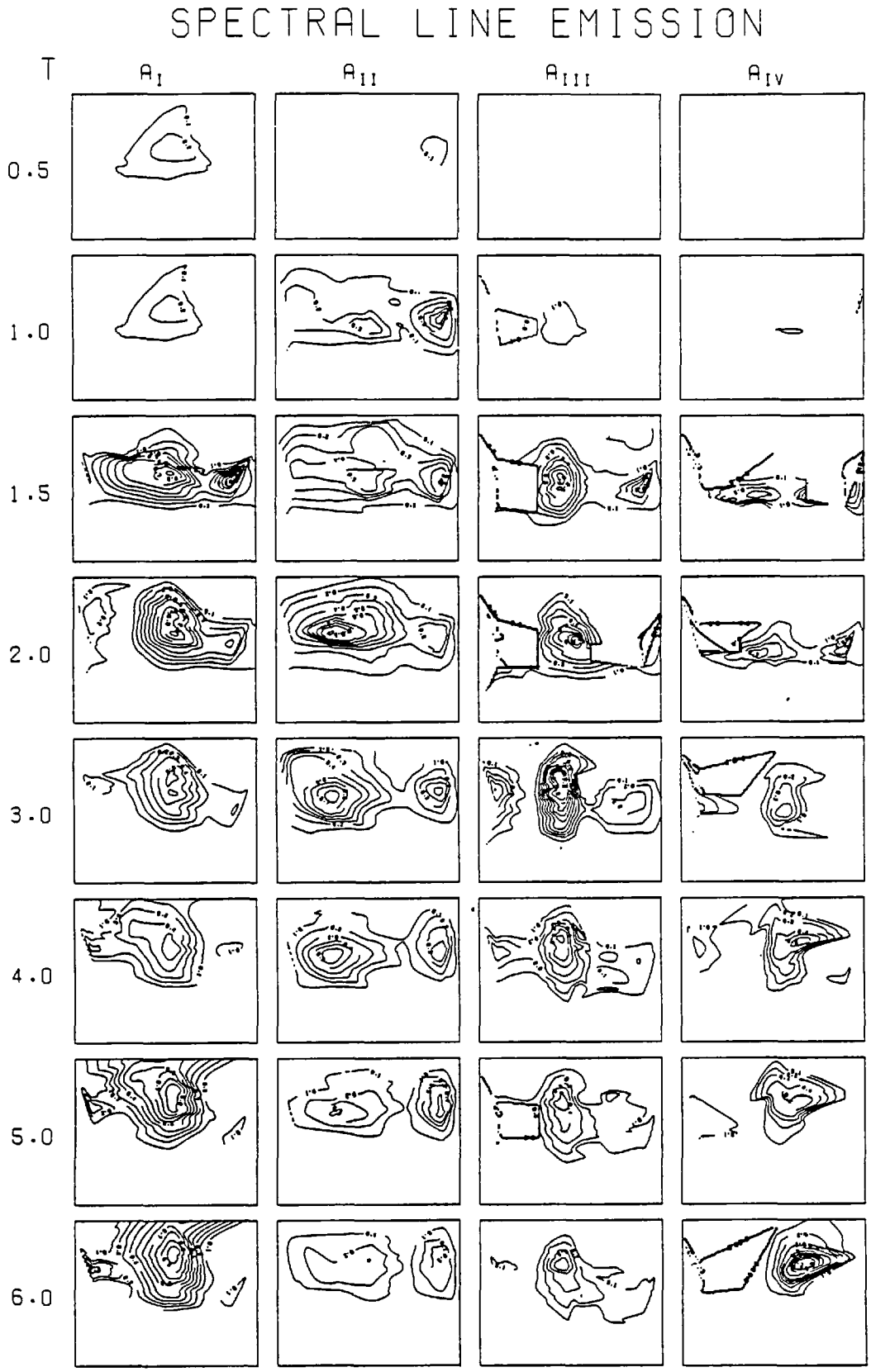

Fig. 4.12 Spatial distribution of spectral line emission, radial line of sight. The boxes are 5 x 4 cm in real space. Time in μs is shown on the left.

hand boundaries for each box are positions of cusp coils, the total height represented being 4 cm in real space. There are regions where the plot becomes discontinuous, possibly because of a low density of points in the original data.

4.6 Line broadening

Line profiles have been obtained on a shot to shot basis, a complete profile being obtained in about 50 discharges. The poor reproducibility results in a fairly large uncertainty in the line shape. It has already been pointed out (Section 2.5.4) that in the case of the Polytron the broadening is mainly Doppler broadening. It is possible then to obtain an equivalent 'temperature' from the line widths:

$$kT = \frac{mc^2}{4 \ln 2} \left(\frac{w_\lambda}{\lambda_o} \right)^2 \qquad 4.1$$

where m is the ion mass, w_λ is the measured line width and λ_o is the centre line wavelength. T is in ^oK.

Typical profiles have been shown in Fig. 3.9. The line of sight used to obtain these profiles is radial. Fig. 4.13 shows the 'temperature' obtained from Equation 4.1. The peak temperature obtained is simultaneous with or immediately after the initial loss.

4.7 Plasma position

Results of plasma position determination by optical and magnetic methods are given here.

Streak camera photographs are particularly useful to determine whether the plasma is in contact with the wall. Fig. 4.14 shows a comparison of the streak photographs with and without magnetic field. The slit is next to a cusp field coil. The photographs were taken from underneath; the outermost wall is to the left.

Fig. 4.15 shows some results obtained with a PIN photodiode array. At late times the plasma emission is not very well defined. This is probably due to the poor UV response of the photodiodes used.

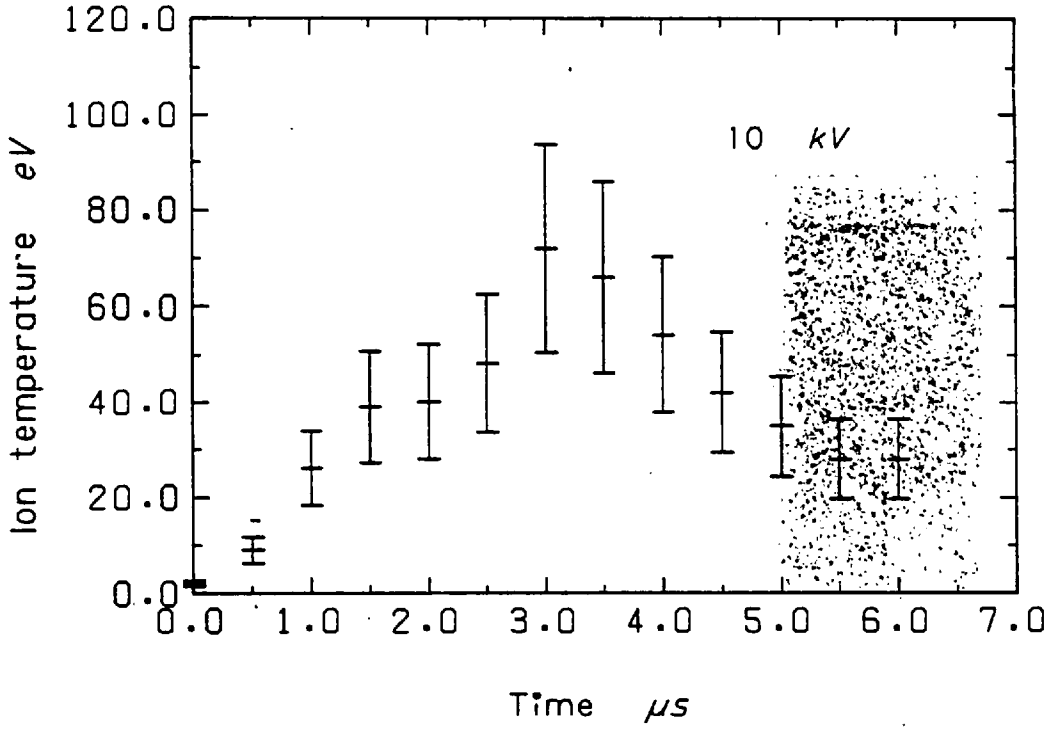

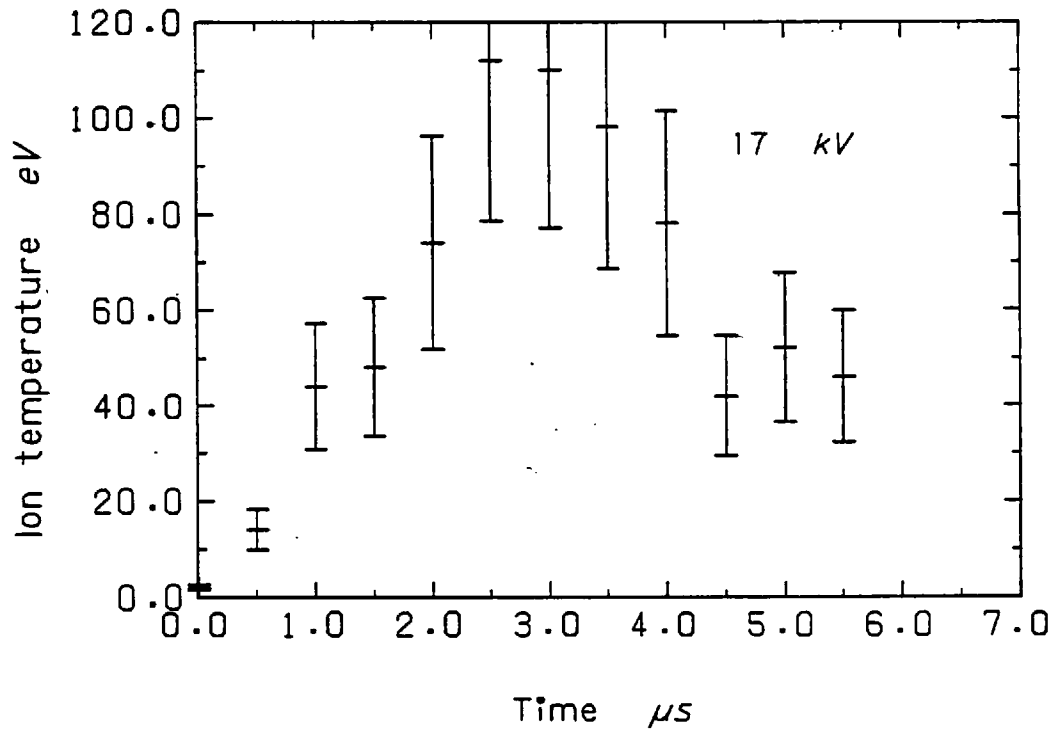

Fig. 4.13 Ion temperature as a function of time obtained from line broadening measurements, V_c = 1.5 kV, p = 3.5 mTorr.

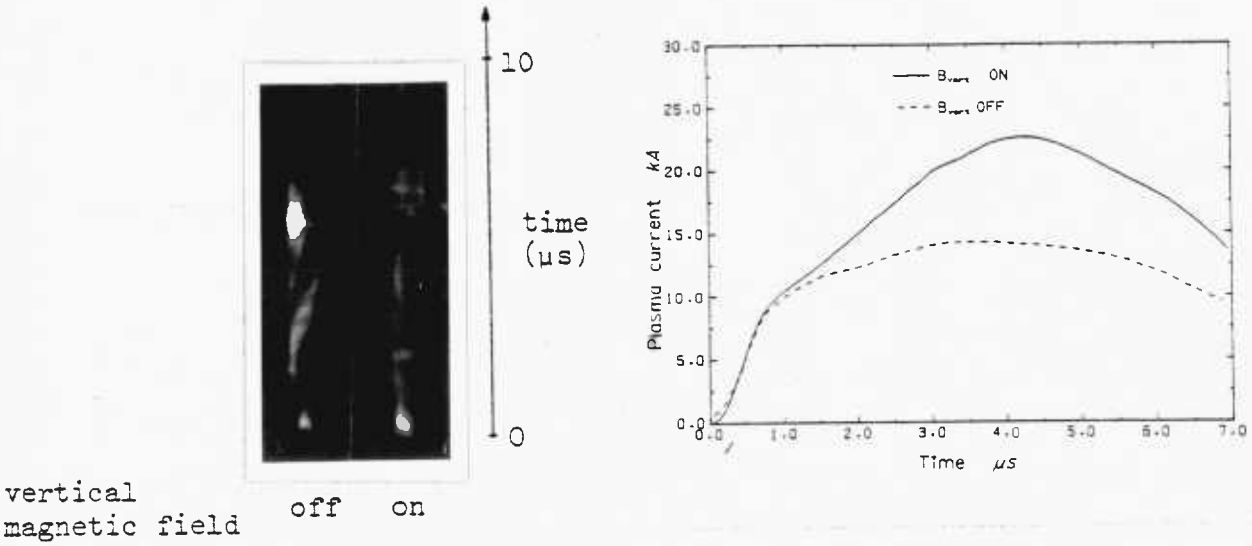

Fig. 4.14 Streak photographs and plasma current with B_{vert} on and off. V_m = 25 kV, V_c = 1.5 kV, p = 3.5 mTorr.

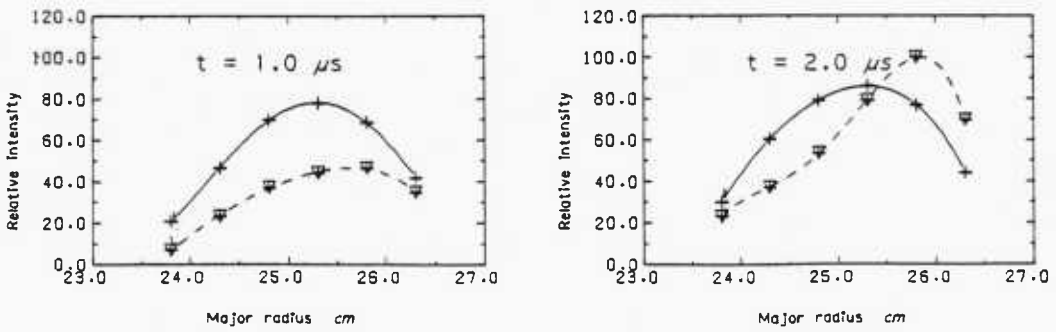

Fig. 4.15 PIN photodiode array intensity distribution at 1.0 and 2.0 μs. B_{vert} :(———) on; (- - - - -) off.

Results obtained by analysing the spatial distribution of AIV (2809 Å) emission and magnetic coil signals are shown in Figs. 4.16 and 4.17. Initially there is good agreement between the two methods, but it becomes poor at later times. The optical method becomes less reliable at later times as the light output is very small. The magnetic coils determine the position of the centre of the plasma current distribution. A change in distribution can be interpreted as an overall plasma motion.

With a vertical magnetic field there is some residual horizontal and vertical displacement. This is of the same order as the plasma column diameter.

4.8 Faraday cup probe measurements

These are measurements of the ion flux at the wall position in the equatorial plane. Results shown are only for low filling pressure (3.5 mTorr)as the Faraday probe does not operate satisfactorily at higher pressures (Bakulin et al., 1969). The bias voltage used was -70V and -140V, no appreciable difference being observed for the two cases.

The spatial dependence of the ion flux is given in Fig. 4.18, the temporal dependence in Fig. 4.19. The width of this flux is of the same magnitude as the electric sheath width. The total flux is large initially, peaking at the time the plasma current has its 'shoulder'. After this it becomes small.

For one of the conditions studied the Faraday cup probe bias was reversed. Under these conditions electrons are collected, the signal being 250 times larger than the corresponding ion signal. This is the same as the square root of the ion-electron mass ratio.

It should be pointed out that the electron signal outside the sheath region appears only after the initial loss.

4.9 Double electric probe in the presence of a vertical magnetic field

Attempts were made to measure the sheath electric field with a double electric probe for the case with a vertical magnetic field present, to compare with the measurement without magnetic field. Results

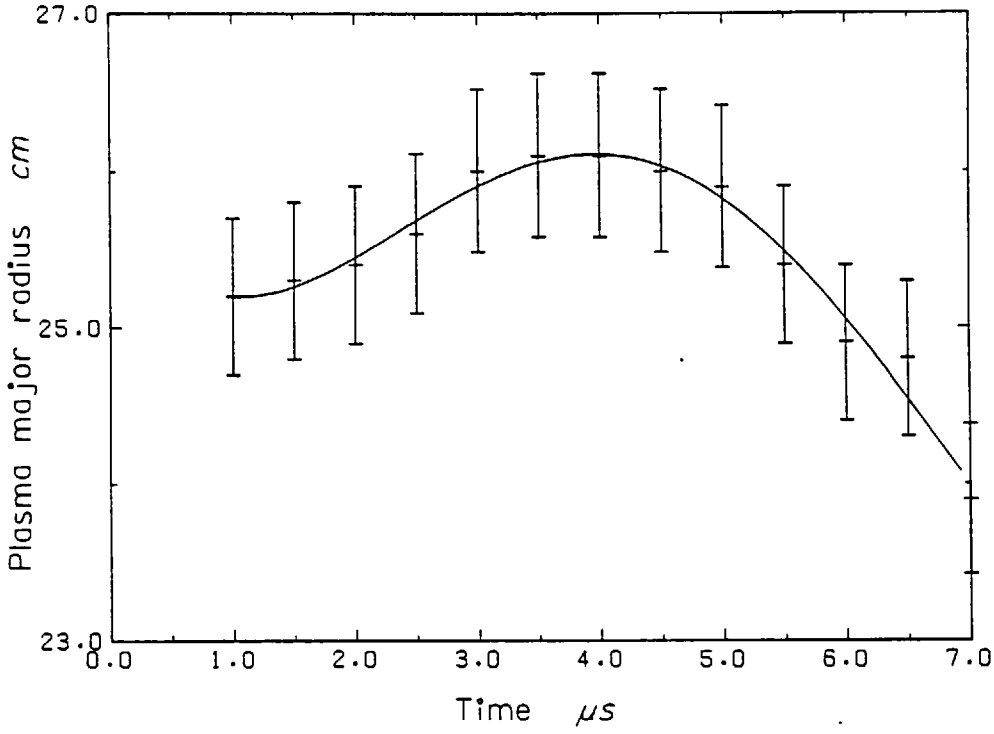

Fig. 4.16 Horizontal plasma displacement as a function of time measured with magnetic coils. V_m = 17 kV, V_c = 1.5 kV, p = 3.5 mTorr.

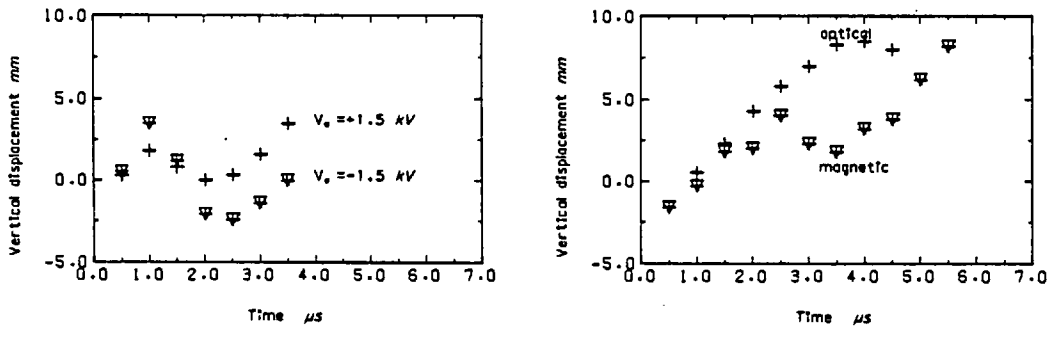

Fig. 4.17 Vertical plasma displacement measured with magnetic coils. (a) V_m = 25 kV, p = 12 mTorr (left). (b) Average ($V_c = \pm$ 1.5 kV) displacement. V_m = 17 kV, p = 3.5 mTorr using magnetic coils and optical methods.

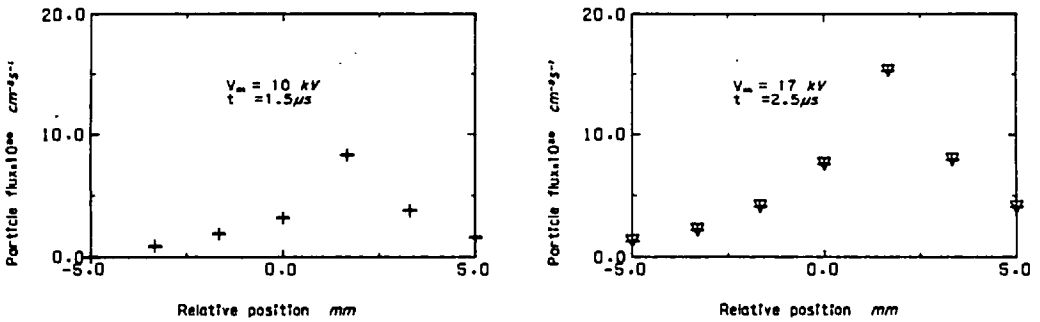

Fig. 4.18 Ion flux to the wall for two conditions: V_c = 1.5 kV, p = 3.5 mTorr.

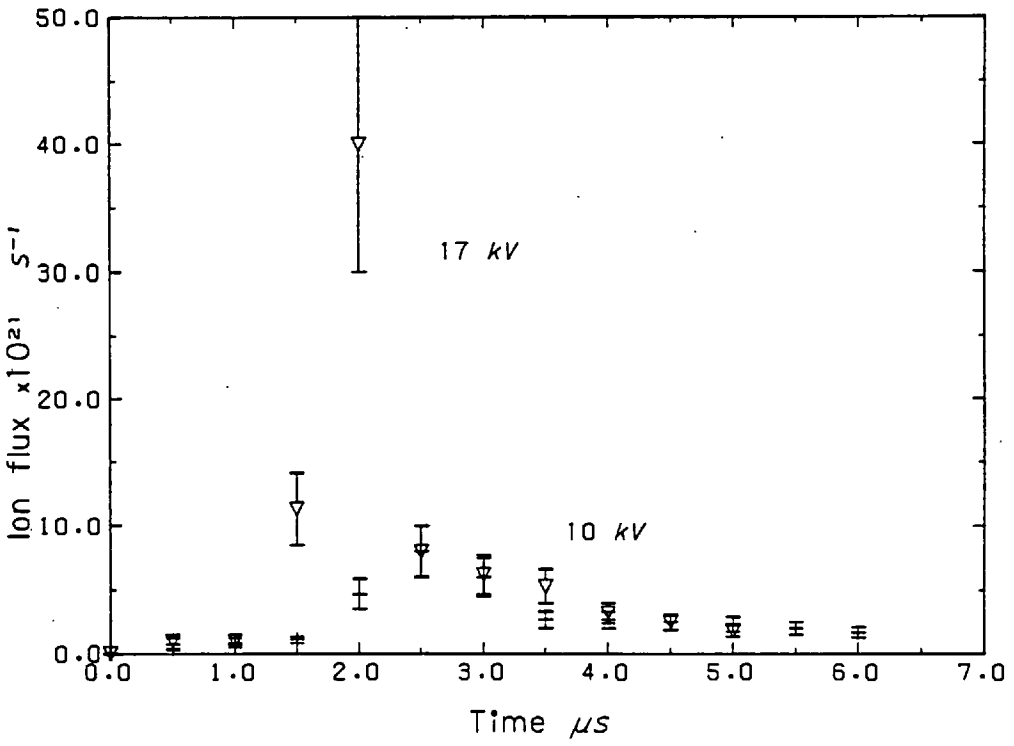

Fig. 4.19 Total ion flux to the wall as a function of time. V_m = 10 and 17 kV, V_c = 1.5 kV, p = 3.5 mTorr.

show that initially there is an electric field in the sheath region, which disappears during the loss time, occasionally reappearing for short times later. In Fig. 4.20 a comparison of double probe and Faraday cup signals shows up this result , which shows that the double probe is shorted out due to plasma interaction.

4.10 Other effects

In this section several effects, presumably related to wall interaction, are described. The evidence is mainly qualitative.

It became apparent that the plasma current shape was slightly different for the first shot of the day, the system being pumped overnight by an ion pump to pressures of 2×10^{-5} Torr. After an hour or so of pumping with our diffusion pump-cold trap system, the normal operating base pressure is reached, $1 \sim 2 \times 10^{-6}$ Torr. This difference between starting and following shots was particularly noticeable for low filling density and high voltage. Fig. 4.21 shows plasma current for first and second shots, 25 kV charging voltage, 3.5 mTorr filling pressure. The

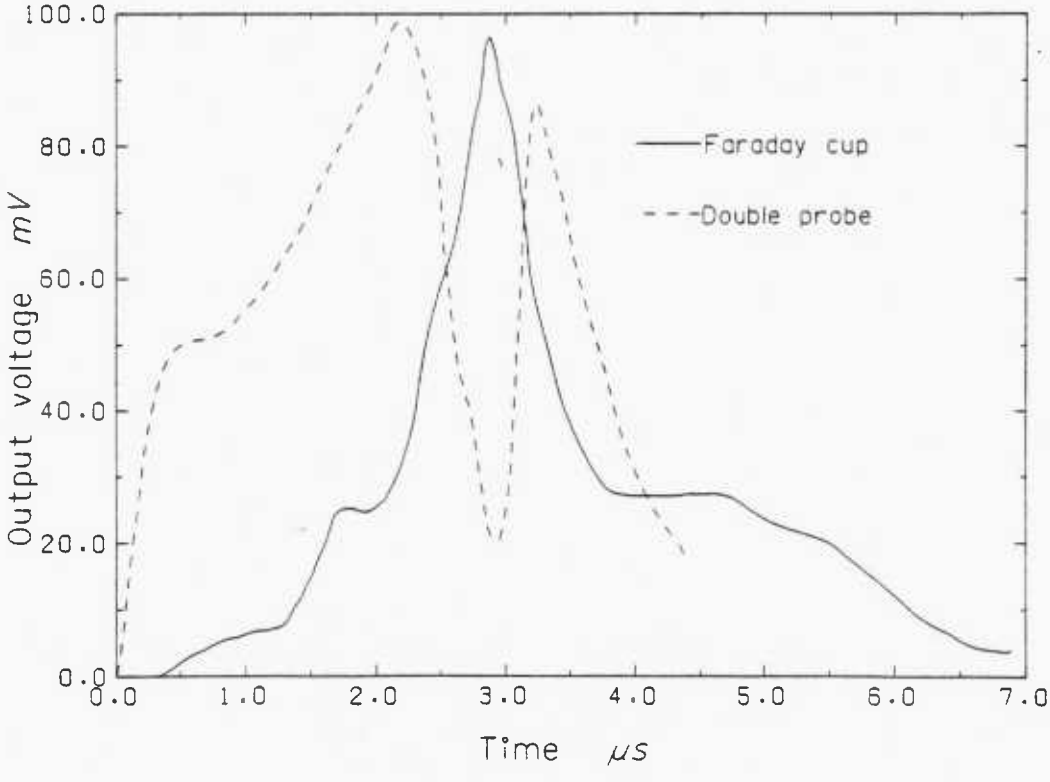

Fig. 4.20 Typical output signals obtained with Faraday cup and double probe. V_m = 15 kV, V_c = 1.5 kV, p = 3.5 mTorr, B_{vert} on.

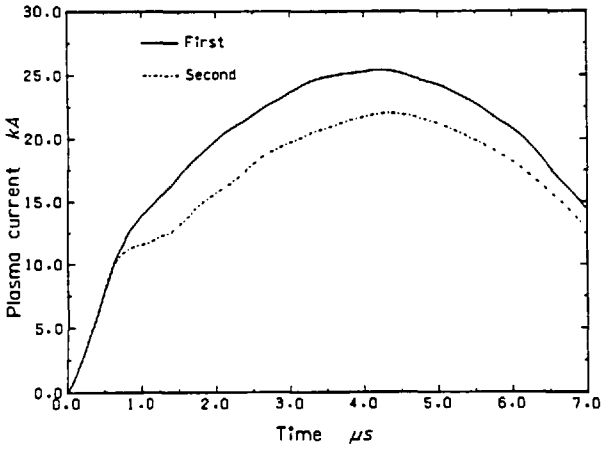

Fig. 4.21 Plasma current for first and second discharge of the day. V_m = 25 kV, V_c = 1.5 kV, p = 3.5 mTorr, B_{vert} on.

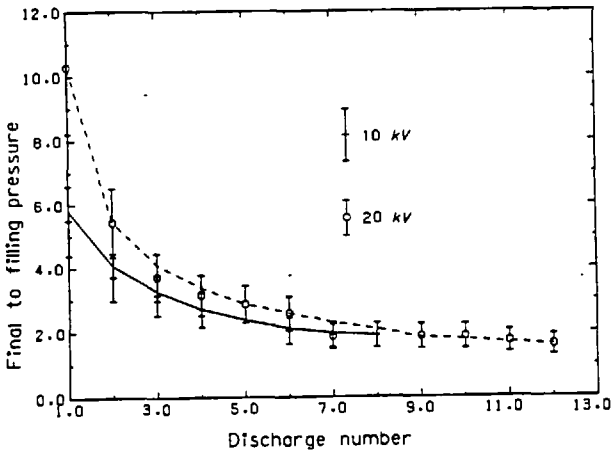

Fig. 4.22 Ratio of final to filling pressure as a function of discharge number. V_m = 10 and 20 kV, V_c = 1.5 kV, p = 3.5 mTorr.

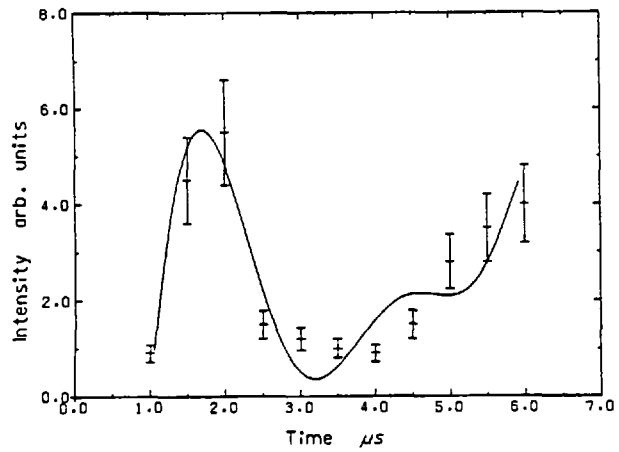

Fig. 4.23 Impurity line emission. Radial line of sight, ring cusp region. V_m = 17 kV, V_c = 1.5 kV, p = 3.5 mTorr.

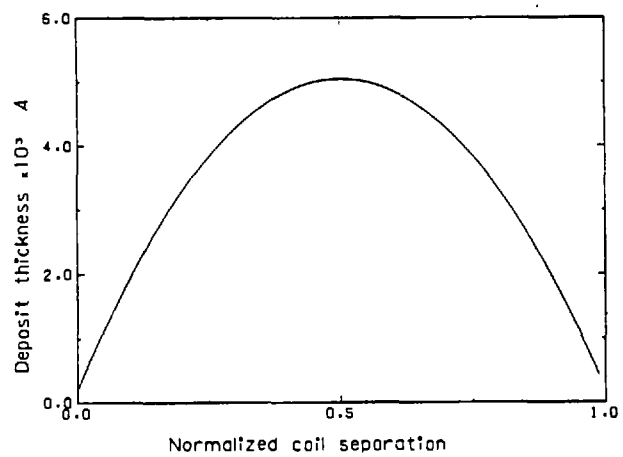

Fig. 4.24 Wall deposit thickness as a function of distance between coils. Several hundred discharges with B_{vert} on required to obtain this thickness.

'shoulder' associated with the initial loss is less marked on the first discharge; this can be accounted for in terms of a higher temperature or higher density, the former being unlikely. In order to test this, a series of shots, with the discharge vessel isolated from the pumping system, was carried out, results of which are shown in Fig. 4.22. The final pressure has a large increase in the first shot, the difference becoming smaller until it reaches a steady state.

Further evidence that the release of gas from the wall is associated with the initial loss is obtained from spectroscopic measurements that show an impurity line appearing after the initial loss, shown in Fig. 4.23. This line is close to the 2809 AIV line, it is either a Nitrogen or Oxygen line.

The quartz vessel had to be removed from the system on two occasions, the first one for induction rod repairs before using a vertical magnetic field and the second one because of a diagnostic port breakage after several hundred discharges with a vertical magnetic field applied. On this second occasion it was noticed that the inner wall of the discharge tube was coated unevenly by a brownish deposit, with no coating under cusp coils. Under white light illumination a set of coloured interference fringes is formed in this deposit. The thickness of this deposit has been calculated from fringe position (Born and Wolf, 1970) and a microdensitometer scan of a colour slide of it. This is shown in Fig. 4.24 as a function of distance between coils.

Chapter 5

DISCUSSION OF THE EXPERIMENTAL OBSERVATIONS

In this chapter an analysis of the results presented in Chapter 4 is put forward. The analysis is partly qualitative, particularly for the case of plasma-wall interaction.

5.1 Ion and electron densities

Conservation of momentum can be used to obtain an estimate of the ion density. For the plasma the equation of motion is given by

$$F_\phi = \sum_i n_i m_i A_i l_i \frac{dv_i}{dt} \qquad 5.1$$

where A_i is the cross section and l_i the length of the volume containing the i species being accelerated.

Assuming that cross sections, lengths and densities are not time dependent Equation 5.1 can be integrated to give

$$\int F_\phi dt = \sum_i n_i m_i A_i l_i v_i \qquad 5.2$$

The cross section can be obtained from the spatial distribution of the spectral line emission, and the length l_i from the width of the sheath obtained with the double probe measurements. Thus since ion velocity and force have been measured, the number density is the only unknown parameter. However, further assumptions have to be made, namely that the cross section and length of the accelerated volume for different ionization species are the same and that ion velocities are proportional to the charge of the corresponding ion. The last assumption has been experimentally verified for AIV and AIII ions after 3 μs (Fig. 5.5). Equation 5.2 can then be rewritten as

$$n = \sum_i n_i = \frac{\int F_\phi dt}{2 m_i A l v_{IV}} \qquad 5.3$$

where v_{IV} is the AIV velocity and the numerical factor 2 is to take into

account the contribution of AII and AIII ions.

Results of this calculation are shown in Fig. 5.1. An apparent density increase is observed at a time corresponding to the initial loss time. This is probably due to the fact that ions being lost from regions of uncontained particles carry to the wall part of the momentum being transferred to the plasma. A density increase is observed at late times, immediately before the disappearance of the force (4 to 5 μs). At this time particle loss, obtained from Faraday cup probe measurements, is small. This can therefore be ascribed to an influx of neutral Argon and impurities from the wall into the body of the discharge. A more detailed discussion of this influx of impurities is given in Section 5.7.

The average electron density can be obtained from the ion density as calculated above, and the average ion charge, obtained from spectral line emission measurements. The electron density obtained in this way is shown in Fig. 5.2. The electron density so obtained reaches a maximum at around 1.5 μs and decreases slowly after that.

5.2 Ion temperature

Doppler broadening of spectral lines represents the velocity distribution of the plasma ions along the line of sight. Under suitable conditions it is possible to obtain the ion temperature from the Doppler profiles. In particular the measurements have to be done with a line of sight along a major radius of the plasma torus. In order to establish whether the measured Doppler width is a real temperature a toroidal single particle computer code, originally developed by Kilkenny (1972) was used.

The code calculates ion trajectories only. Electron motion is neglected because the cusp magnetic field traps the electrons. Further it is assumed that the plasma magnetic field does not perturb the vacuum magnetic field. The electric field is assumed constant in time and with an inverse radial dependence.

The coordinate system used is cylindrical ($r = R_o + R, \phi, z$). Since R_o is the major radius of the torus, the coordinate R measures the radial component of the distance from the minor axis. The equations of motion are:

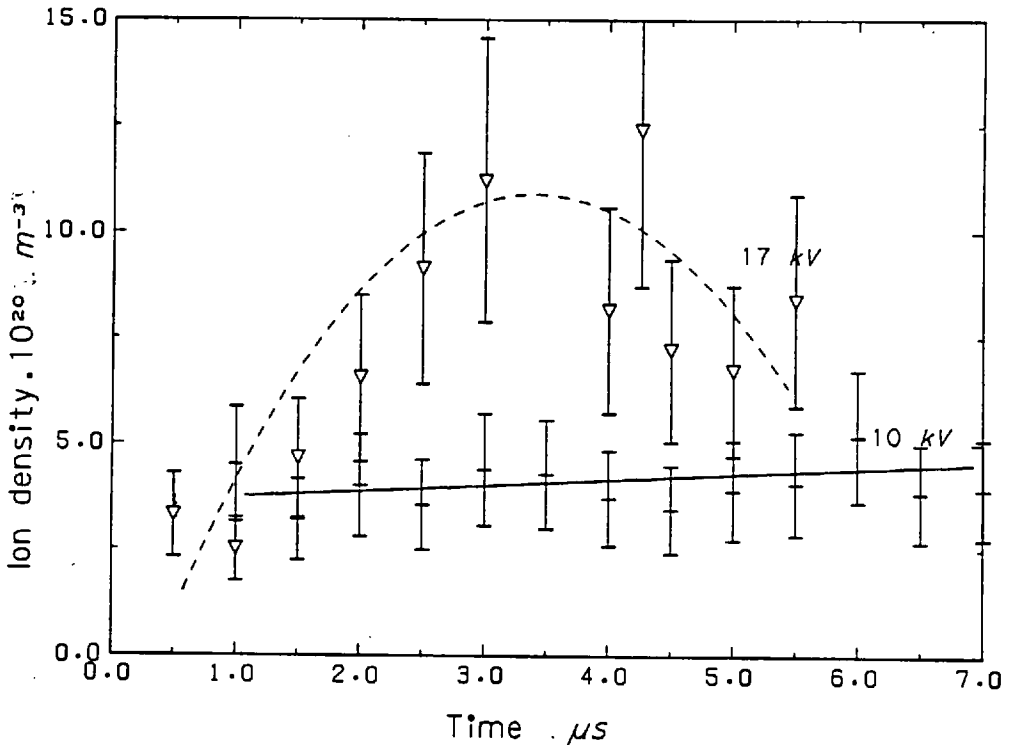

Fig. 5.1 Ion density as a function of time obtained from momentum balance. V_m = 10 and 17 kV, V_c = 1.5 kV, p = 3.5 mTorr.

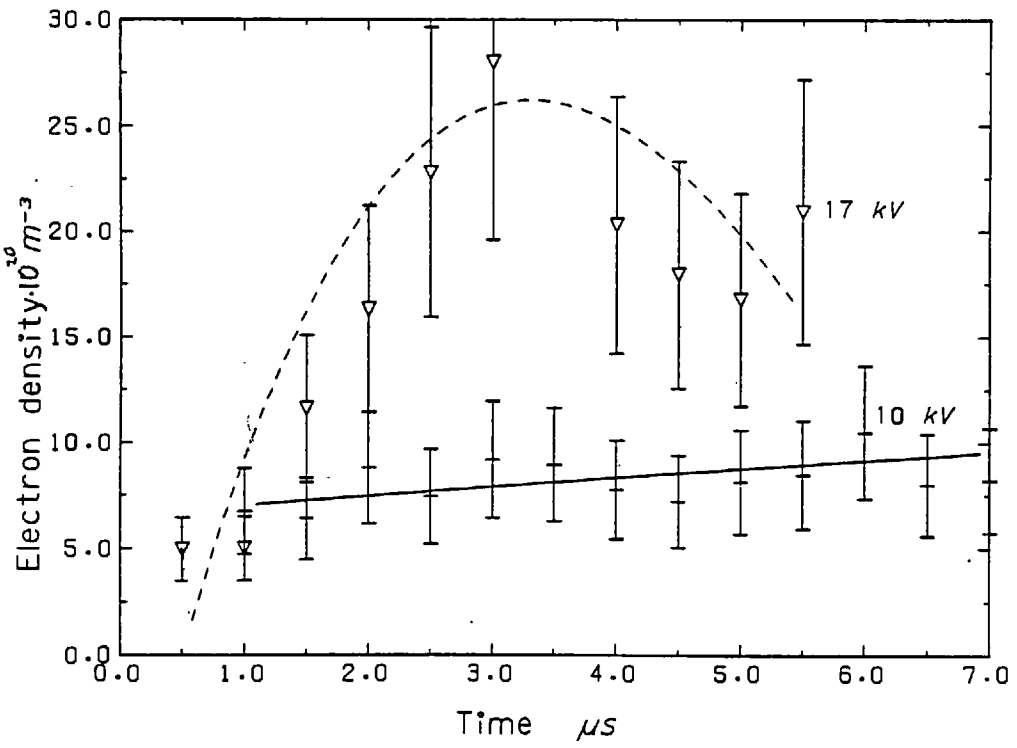

Fig. 5.2 Electron density as a function of time derived from momentum balance and average charge. V_m = 10 and 17 kV, V_c = 1.5 kV, p = 3.5 mTorr.

$$\ddot{R} = \frac{Ze}{m}(v_\phi B_z - v_z B_\phi) + \frac{v_\phi^2}{R_o + R}$$

$$\ddot{\phi} = \frac{Ze}{(R + R_o)m}(E_\phi + v_z B_R - v_R B_z) - \frac{2\dot{\phi}\dot{R}}{R + R_o}$$

$$\ddot{Z} = \frac{Ze}{m}(v_R B_\phi - v_\phi B_R) \qquad 5.4$$

$$\dot{R} = v_R$$

$$\dot{\phi} = \frac{v_\phi}{R + R_o}$$

$$\dot{z} = v_z$$

The magnetic field for the actual cusp coil configuration in the present device is calculated separately and stored in a 3-dimensional mesh (23 x 9 x 13). The value at any particular point is obtained by interpolating from this set of values.

The applied toroidal electric field is given by

$$E_\phi = \frac{E_o}{1 + R/R_o} \qquad 5.5$$

Thus E_ϕ is pseudo conservative.

Because of symmetry and periodicity any region can be reduced to

$$\phi : 0 \text{ to } 5^\circ$$

$$Z : 0 \text{ to } r_{max} \qquad 5.6$$

$$R : -r_{max} \text{ to } r_{max}$$

where r_{max} is the minor radius of the torus.

The equations are integrated using Merson's method (Lance, 1961). This is a modified fourth order Runge-Kutta scheme which allows an estimate of the error to be made. The method is accurate, but very slow.

Each ion is given zero initial velocity and a certain initial position and is followed for a predetermined time or until it is lost.

Using this program the radial velocity distribution is calculated as a function of time for each of 64 equal volume elements into which a cusp volume has been divided. From this data the radial velocity distribution for all the ions at any minor cross section can be obtained and compared with those obtained experimentally. Velocity is proportional to wavelength shift.

The calculated velocity distributions in two neighbouring volume elements out of the 64 into which a cusp volume is divided are shown in Fig. 5.3. It is clear that the velocity distribution obtained is not a true temperature as the centre of the distribution is shifted for the two volumes by the same amount as the width of the velocity distributions. The calculated velocity distribution over the minor cross section is given in Fig. 5.4. Also shown is the measured velocity distribution. The measured FWHM of the distribution is several times larger than the calculated value. The calculated FWHM is a third of the illustrated width. Its contribution to the observed FWHM will therefore be small. Thus an interpretation of the measured values of line broadening as ion temperature is reasonable.

The ion temperature obtained from the line widths measured along the major radius in the magnetic cusp region is shown in Fig. 4.13 as a function of time. It should be pointed out that the measurement was done on a shot to shot basis. As the discharge is not very reproducible the observed profile is broader than the true profile.

Within the experimental error the ion temperature obtained in the region of a cusp coil is not different from that obtained in the ring cusp region. This would be the case if the observed broadening were due to ion thermal motion.

According to laser scattering measurements made by Kilkenny, the electron temperature and density for the same discharge conditions (V_{cusp} = 1.5 kV, V_{main} = 10 kV, 3.5 mTorr filling pressure) are 4.5 eV and $10^{21} m^{-3}$ at 0.5 μs. These figures inserted in Spitzer's formula

$$\tau_{ei} = \frac{3(4\pi\varepsilon_o)^2 m_e m_i}{8(2\pi)^{\frac{1}{2}} n_e Z^2 e^4 \ln\Lambda} \left(\frac{kT_e}{m_e} + \frac{kT_i}{m_i} \right)^{3/2} \qquad 5.7$$

give an electron-ion energy equipartition time of 12 μs at 0.5 μs. Since T_i at this time is 15 eV (cf $T_e \sim 4.5$ eV) the observed ion temperature must be due to some form of direct heating, possibly viscous

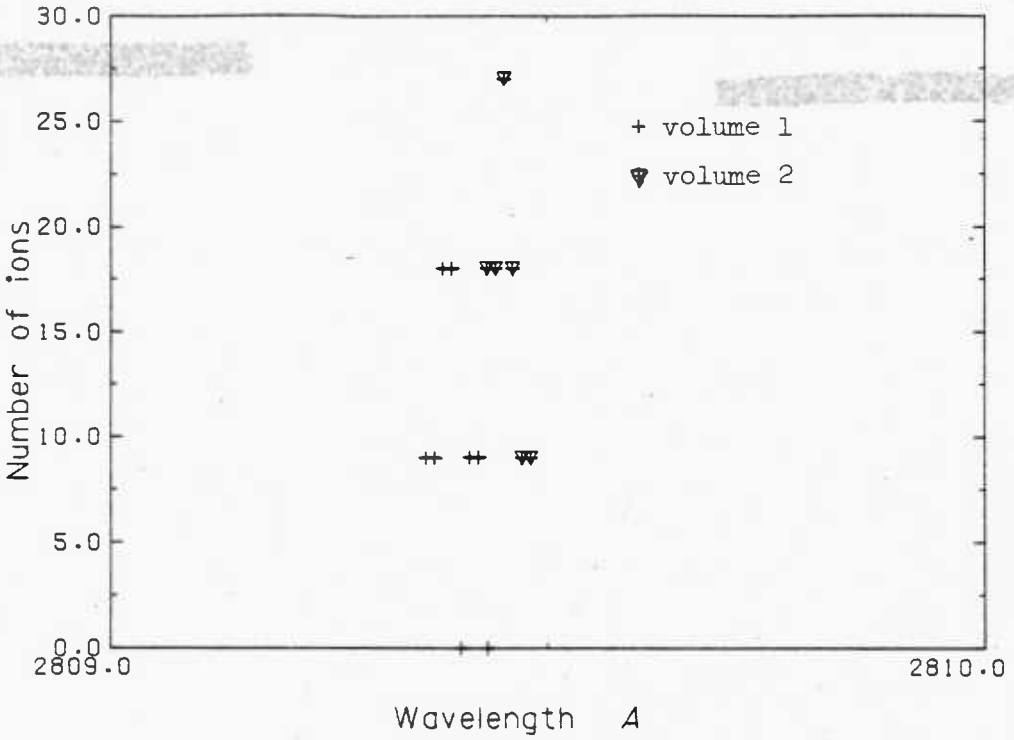

Fig. 5.3 Calculated velocity distribution in two adjacent elementary volumes into which the plasma region has been divided. V_m = 10 kV, V_c = 1.5 kV, p = 3.5 mTorr at t = 2.0 μs. Velocity is proportional to wavelength shift.

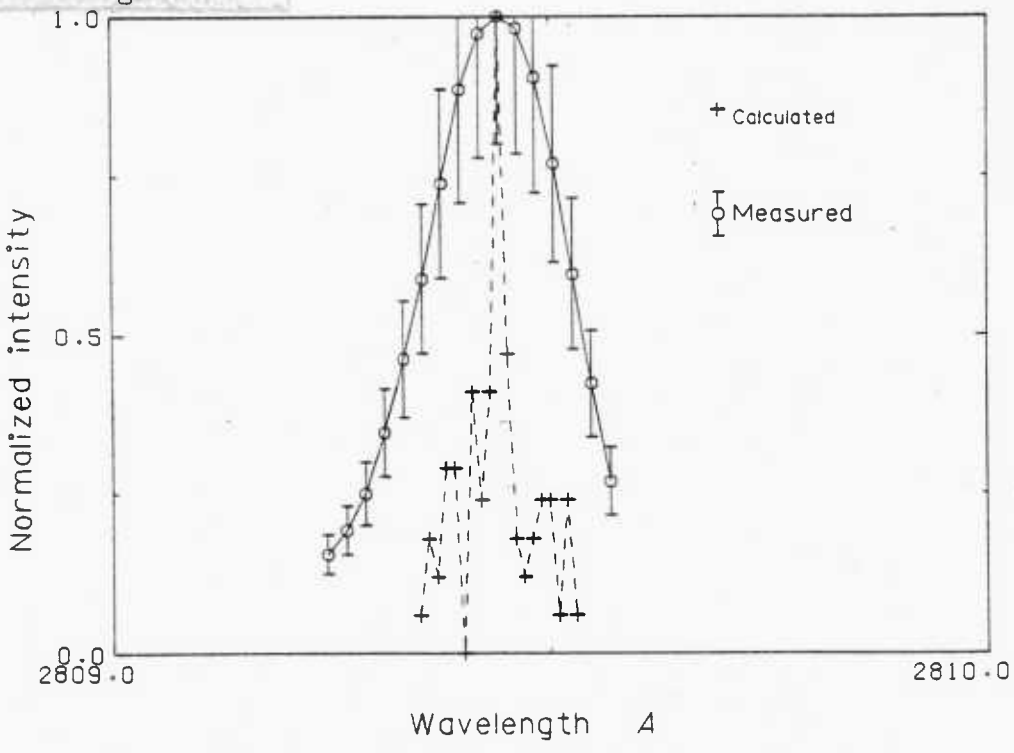

Fig. 5.4 Calculated and measured AIV line profiles. V_m = 10 kV, V_c = 1.5 kV, p = 3.5 mTorr. Line of sight along major radius, ring cusp region.

heating.

The heating rate Q_{vis} per unit volume in a plasma as a result of viscosity is given by

$$Q_{vis} = -\pi_{\alpha\beta}\frac{\partial v_\alpha}{\partial x_\beta} \qquad 5.8$$

where $\pi_{\alpha\beta}$ are the components of the stress tensor, v_α the velocity components and x_β the position coordinates.

Since electron viscosity can be neglected because of the small electron mass, and if terms of order $(\omega_{ci}\,\tau_i)^{-2}$ are neglected, the heating rate generated with magnetic field in the z direction is

$$Q_{vis} = \frac{\eta_o}{3}\left(\frac{\partial v_x}{\partial x} + \frac{\partial v_y}{\partial y} - 2\frac{\partial v_z}{\partial z}\right)^2 \qquad 5.9$$

where

$$\eta_o = 0.96\,\frac{3(4\pi\epsilon_o)^2\sqrt{m_i}(kT)^{5/2}}{4\sqrt{\pi}\,\ln\Lambda\; e^4}$$

is the ion viscosity coefficient (Braginskii, 1965). $\omega_{ci}\,\tau_i$ is of the order of 0.5 in the experiment. However, terms in $(\omega_{ci}\,\tau_i)^{-2}$ contribute little to the viscous heating rate. The viscous heating rate given by Equation 5.9 is therefore a good approximation.

It has not been possible to determine experimentally the terms $\partial v_i/\partial x_i$ in Equation 5.9. However, an estimate can be obtained from the results of the single particle calculation described earlier. The value estimated for the term in brackets in Equation 5.9 is $2 \times 10^5\ s^{-1}$, which is an order of magnitude lower than the quotient of centre of mass velocity and plasma diameter ($4 \times 10^6\ s^{-1}$). Using the estimated value for the term in brackets in Equation 5.9 and the measured ion temperature of 70 eV between 2 and 3 μs, an ion energy increase of 0.01 J per cusp is obtained. The ion energy increase per cusp calculated from ion temperature, ion density and volume is 0.015 J, between 2 and 3 μs. A decrease of ion temperature is observed after 3.5 μs (Fig. 4.13) whilst the toroidal velocity (Fig. 4.9) and accelerating force (Fig. 4.8) increase or are nearly constant. As ions and electrons are thermally decoupled ($\tau_{ei} \sim 12$ μs) it is evident that a direct ion energy loss process

occurs. Charge exchange processes, which are very efficient at removing ions from the plasma, may be responsible.

The toroidal velocity ratio AIV to AIII is shown in Fig. 5.5. AIV and AIII velocities were not measured simultaneously, twenty discharges being used to obtain the velocity ratio. Initially the ratio is nearly one and it increases to 1.5 at 5 μs, immediately after the disappearance of the accelerating force. A value of 1.5, corresponding to the charge ratio, would be expected if viscosity were not important because the ion accelerating force is proportional to the ionic charge. However, the measurements are tangential line of sight averages and therefore contributions from different plasma regions are obtained. Spatial distribution of the line emission along a major radius line of sight shows that atoms at a higher ionization stage are closer to the torus axis. The observed increase of the velocity ratio is consistent with gas and impurities reaching the plasma, highly ionized atoms being reached later.

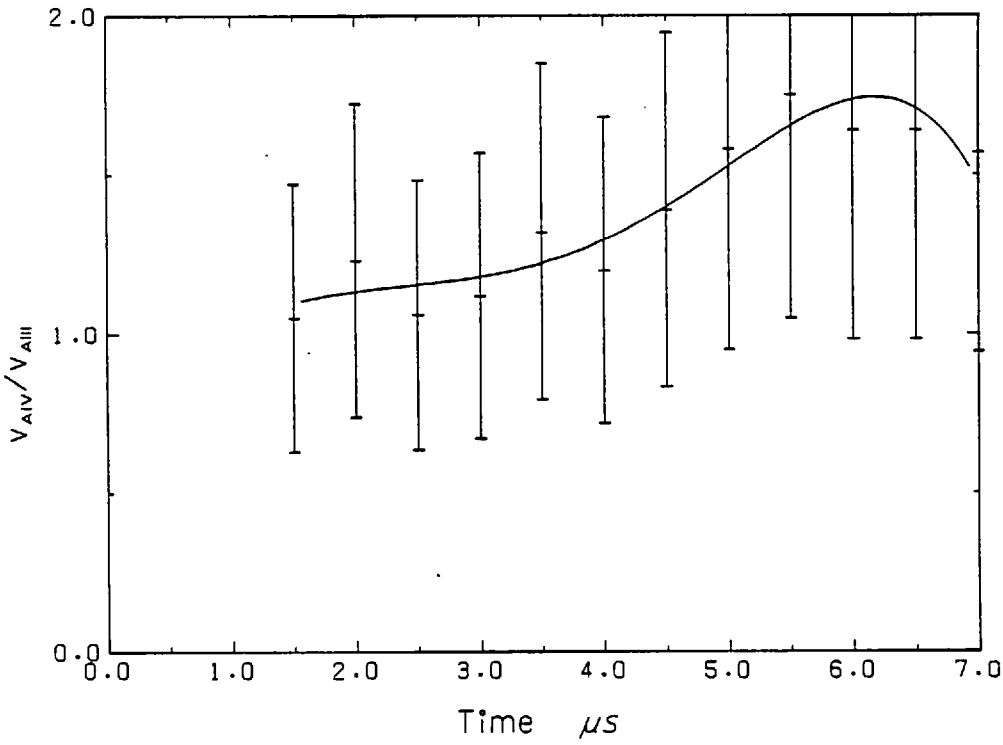

Fig. 5.5 AIV to AIII toroidal velocity ratio as a function of time. V_m = 10 kV, V_c = 1.5 kV, p = 3.5 mTorr.

5.3 Energy balance

An estimate of the energy contained and lost by the plasma is obtained in this section from the measurements made. The contribution of electrons to the energy balance is obtained from the plasma energy equation and electron temperature measurements at early times made by Kilkenny (1972). The plasma energy equation is

$$\frac{\partial}{\partial t}\left(\frac{1}{2}\rho v^2 + \frac{3}{2} n\,(kT_e + kT_i) + \sum_i n_i I_i\right) + \nabla.\left(\frac{1}{2}\rho v^2 \underline{v} + U\underline{v} + \underline{\underline{P}}.\underline{v} + \underline{Q} + \underline{S}\right) = \underline{j}.\underline{E} \qquad 5.10$$

where n_i and I_i are the number density and ionization energy for stage i, $\underline{\underline{P}}$ is the pressure tensor, U the internal energy, $\underline{Q}$ the heat flux, $\underline{S}$ the radiation flux, ρ the mass density, $\underline{j}$ the plasma current density and $\underline{E}$ the applied electric field.

The energy equation is integrated over a volume between two cusp coils and the tube walls. The different terms are evaluated. In particular the heat flux loss to the walls is

$$\int_V \nabla.\underline{Q}\,dV = \int_S \underline{Q}.d\underline{S} = 2\pi a\, w\, Q_r \qquad 5.11$$

where a is the tube radius, w the equivalent width over which heat loss is occuring and Q_r is the r component of the heat flux. Initially the electron-electron mean free path is small, so classical heat conduction is valid. At later times, after about 0.5 μs the mean free path becomes comparable with the minor radius of the tube (this calculation uses Kilkenny's experimental values of T_e). However, double probe measurements of the sheath are still in good agreement with a collisional model with a classical collision frequency. This is probably due to microinstabilities whose effect is to give an equivalent collision frequency. It is not unreasonable to assume then that a classical coefficient of heat conductivity applies. Thus

$$Q_r = -\kappa \frac{\partial T_e}{\partial r} \qquad 5.12$$

where κ is the coefficient of heat conductivity and is given by Spitzer

(1967) as

$$\kappa = \varepsilon\delta_T \frac{80}{2^{1/2}\pi^{3/2}} \frac{k(kT_e)^{5/2}}{m_e^{1/2} e^4 Z \ln\Lambda} \qquad 5.13$$

$$= 4.67 \times 10^{-12} \varepsilon\delta_T \frac{T_e^{5/2}}{Z \ln\Lambda} \frac{\text{cal}}{\text{sec deg cm}}$$

where ε and δ_T are coefficients depending on the ion charge Z.

Assuming that $\frac{\partial T_e}{\partial r} \sim \frac{T_e}{a}$, the heat flux term in the energy equation becomes

$$\int \nabla.\underline{Q}\, dV = \varepsilon\delta_T 80 \left(\frac{2}{\pi}\right)^{1/2} \frac{(kT_e)^{7/2} w}{m_e^{1/2} e^4 Z \ln\Lambda} \frac{\text{cal cm}^2}{\text{sec deg}} \qquad 5.14$$

The energy input from azimuthal electric field can be neglected as

$$\frac{j_\theta E_\theta}{j_\phi E_\phi} \leq \frac{neE_\phi}{B_r} \frac{r}{2} \frac{\partial B_\phi}{\partial t} \Big/ ne\, v_\phi E_\phi = \frac{r}{2} \frac{1}{B_r} \frac{\partial B_\phi}{\partial t} \frac{1}{v_\phi} \ll 1 \qquad 5.15$$

as $\frac{B_\phi}{B_r} \ll 1$ in the cusp region and $\frac{r}{2} \frac{\partial}{\partial t} \approx v_\phi$.

Radiation flux has been obtained from PIN photodiode measurements, with the corresponding correction for their low UV sensitivity. Centre of mass energy is obtained from ion centre-of-mass velocity measurements and the deduced density in section 5.1. Ion thermal energy is obtained from Doppler broadening of spectral lines. Ionization energy is calculated on the assumption that ionization is uniform over the whole emitting plasma volume. The energy carried away by ions and lost to the walls is obtained from Faraday cup probe and Doppler broadening measurements.

The electron energy has been calculated at early times (up to a microsecond after the beginning of the discharge) from electron temperature measurements obtained by Kilkenny (1972) for a situation with no vertical magnetic field. In the present situation, with a vertical magnetic field, the electron temperature should be nearly the same, as little plasma displacement has occurred and as the plasma current and voltage waveforms are very nearly the same up to this time. The energy equation

can therefore be used to obtain an equivalent width w for the heat flux. The equivalent widths obtained for 10 and 17 kV main bank voltage are 3 and 5 mm. The widths obtained are of the same order as the electric sheath width obtained by means of a double electric probe (6 mm).

The different terms of the energy equation are given as percentages of input energy at 1.0 μs in Table 5.1.

Table 5.1

Energy losses at t = 1.0 μs for 10 and 17 kV main bank voltage, 1.5 kV cusp bank voltage and 3.5 mTorr filling pressure

Energy / Voltage	Ion thermal	Ion centre of mass	Lost by convection of ions	Ionization	Electron thermal	Lost by radiation	Lost by heat flux
10 kV	5%	3%	1%	8%	14%	0.2%	69%
17	10.6%	9.4%	0.4%	3.8%	2.4%	0.1%	73.4%

Radiation energy loss is negligible compared with other losses. Energy lost by ions is small at this time, before the bulk of the initial loss has occurred. Ionization energy is important at this time while most of the ionization takes place. At later times this becomes less important. The most important loss is through heat flux, which at later times becomes 90-95% of the total energy input.

Using at later times the same value of heat flux width, the integrated energy equation (integrated on a cusp volume and in time) can be written as

$$A - B\int T_e dt - C\int T_e^{\frac{1}{2}} dt = 0 \qquad 5.16$$

where A represents the energy contribution of terms other than electron energy or heat flux loss, and B and C are given by

$$B = \frac{3}{2} n k V$$

$$C = \varepsilon\delta_T \left(\frac{2}{\pi}\right)^{1/2} \frac{k^{7/2} w}{m_e^{1/2} e^4 Z \ln\Lambda} \qquad 5.17$$

The electron temperature can be obtained from this equation for times greater than 1.0 μs. (Kilkenny's laser scattering measurements were limited to times earlier than 1.0 μs.) The electron temperature so obtained is plotted as a function of time in Fig. 5.6. The electron temperatures obtained are consistent with Faraday cup probe measurements which show that they should be less than 70 eV.

The energy containment time, defined as

$$\tau_w = \frac{W_p}{\frac{dW_p}{dt}} \qquad 5.18$$

where W_p is the total plasma energy, is obtained from the values obtained for the different energy contributions. The electron energy is 20 to 40% of the total plasma energy. An error of 100% in electron temperature would introduce an error of less than 50% in the energy containment time. The energy containment time so obtained is shown in Fig. 5.7. Between 70 and 95% of the energy supplied to the plasma is lost by heat conduction. Therefore, any errors in the estimate of heat conduction losses have a large effect on the value of energy containment time.

5.4 Ion and electron currents

The total ion and electron currents is evaluated using the measured centre of mass ion velocities and the cross-sectional area of ion flow. The current is given by

$$I_i = e \sum_i n_i Z_i A_i v_i \qquad 5.19$$

where the summation is over all ionization species. Lower ionized states have a smaller contribution as both their charge and velocity are smaller. The total ion current is expressed in terms of the A_{IV} parameters, assuming that the cross-sectional area of current flow is the same for all species, as

$$I_i = e n A Z_{IV} v_{IV} \sum_i \frac{Z_i}{Z_{IV}} \frac{v_i}{v_{IV}} \qquad 5.20$$

$$I_i = 3 \times 1.55\ e n A v_{IV}$$

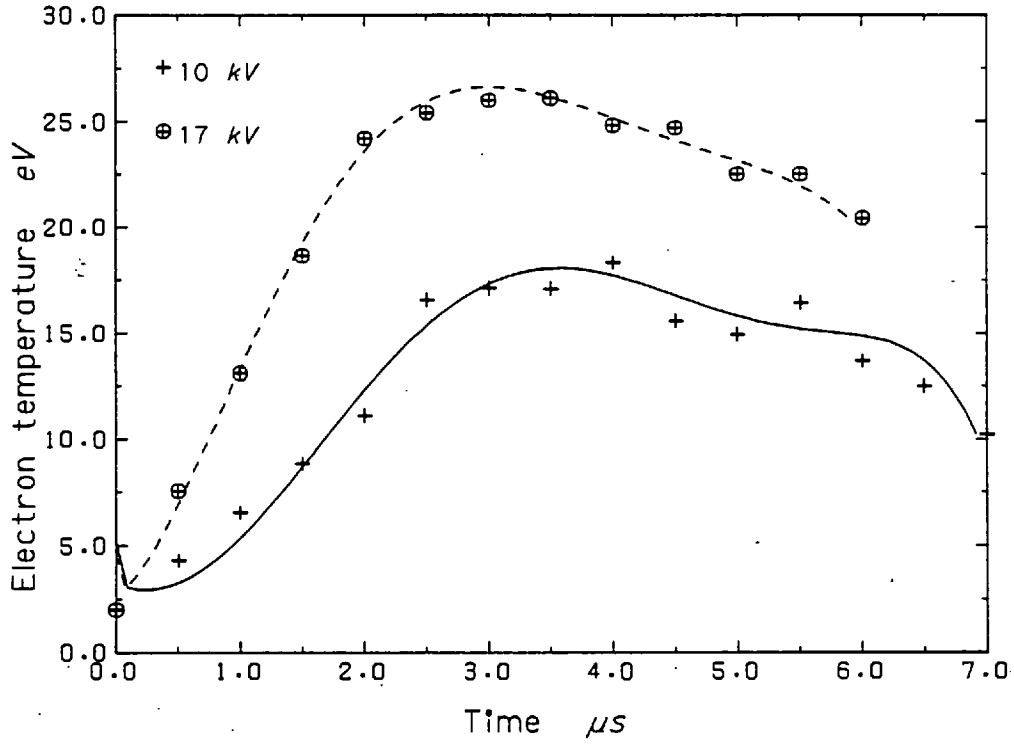

Fig. 5.6 Electron temperature obtained from energy equation. V_m = 10 and 17 kV, V_c = 1.5 kV, p = 3.5 mTorr.

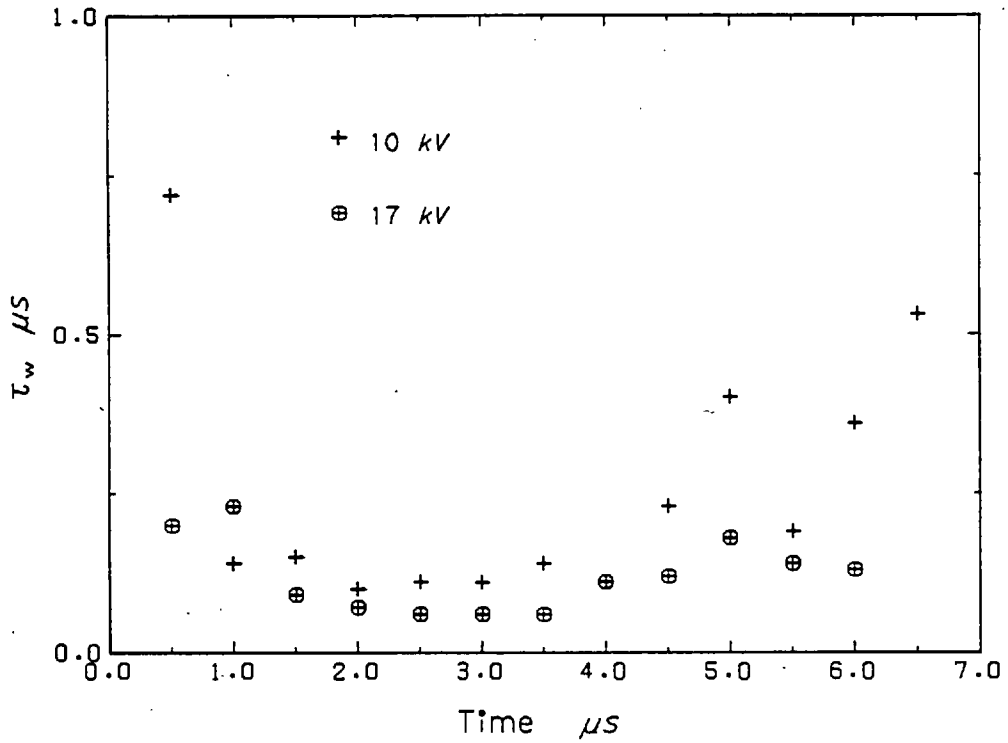

Fig. 5.7 Energy containment time τ_w as a function of time. V_m = 10 and 17 kV, V_c = 1.5 kV, p = 3.5 mTorr.

The numerical factor 1.55 takes into account the contribution of the lower states.

The results obtained are shown in Fig. 5.8 as percentage of the total current, the electron current making up the balance.

It is supposed that electron current can flow only in regions of small Hall parameter, in a narrow channel close to the magnetic axis. Initially the electron current will be limited by plasma resistance, whereas at late times it will be mainly limited by the inductance of this narrow channel.

Assuming that the electron current at initial times flows uniformly in a plasma channel of radius r_o and that all the applied voltage V is dropped in the total resistance R_p of this plasma channel, and using Spitzer's resistivity, the total resistance is given by

$$R_p = \frac{V}{I_e} = \eta \frac{R_o}{r_o^2} \qquad 5.21$$

where R_o is the plasma major radius. The value of r_o has been calculated from Equation 5.21 using the electron current obtained from Figs. 4.3 and 5.8 and assuming a classical resistivity. The values of n_e and T_e used for the resistivity are obtained from Fig. 5.2 and Fig. 5.6. The values of r_o so obtained are shown in Fig. 5.9 together with the values obtained from Equation 2.8, which are the values of r_o obtained from the resistive sheath calculation. The value of r_o obtained from Equation 2.8 is the minimum plasma channel radius, under a cusp coil, whereas the experimentally derived one is an average value.

5.5 Plasma loss

The ratio of lost to total number of particles in a cusp region is obtained from the particle flux measurements and initial number of particles. Fig. 5.10 shows this loss for two different main bank voltages as well as the calculated value obtained by Kilkenny (1972) from a particle calculation for a linear Polytron. Electrons are included in this calculation. The agreement is good. Fig. 5.11 is a comparison of the results obtained for different cusp bank voltages. The loss

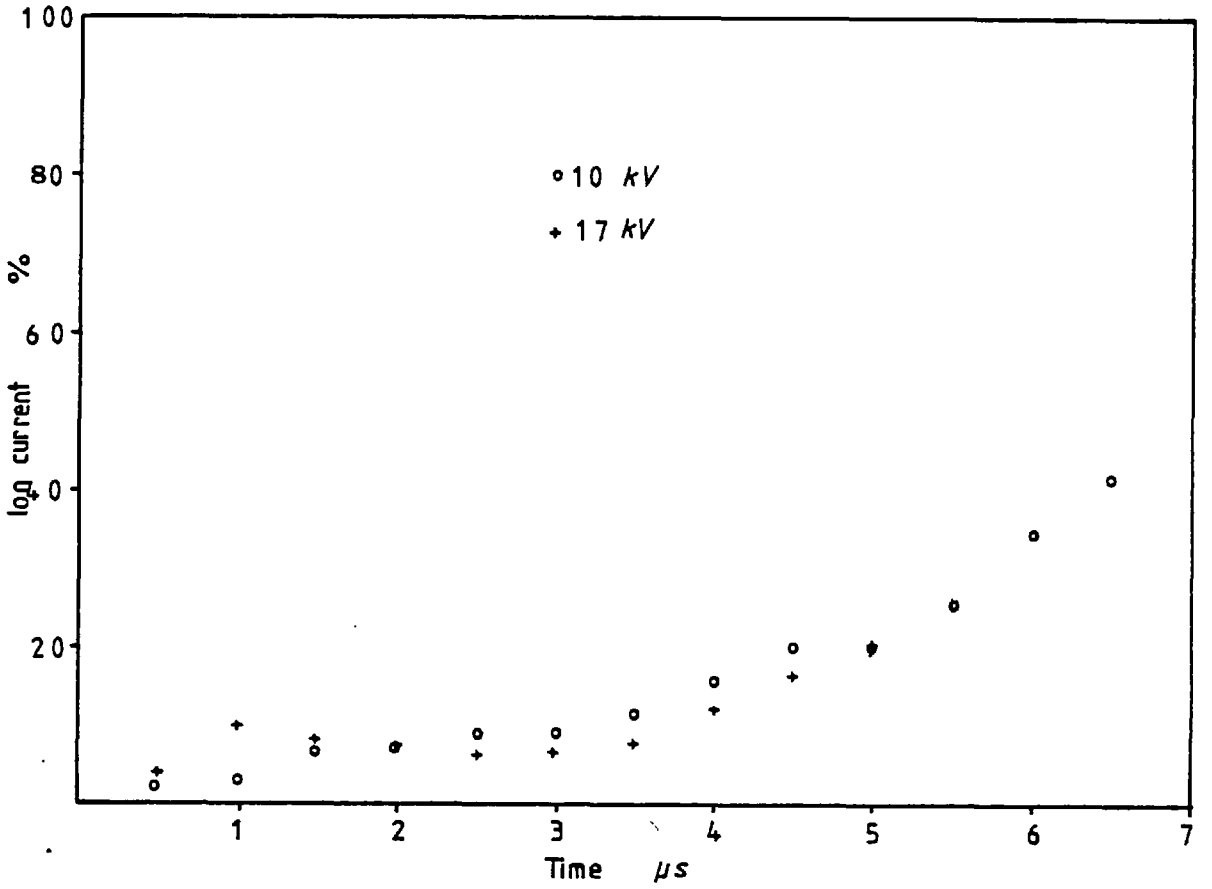

Fig. 5.8 Ion current as percentage of total plasma current versus time. V_m = 10 and 17 kV, V_c = 1.5 kV, p = 3.5 mTorr.

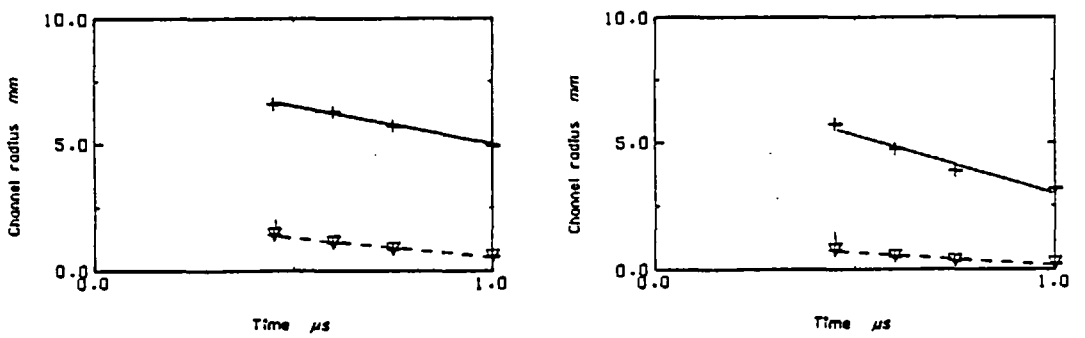

Fig. 5.9 Average radius of electron current channel derived from current, voltage and electron temperature compared with minimum value obtained from Equation 2.8 (----) Theory.

Fig. 5.11 Total particle loss as percentage of the initial number of particles in a cusp volume. V_m = 17 kV, V_c = 1.13 and 1.5 kV, p = 3.5 mTorr.

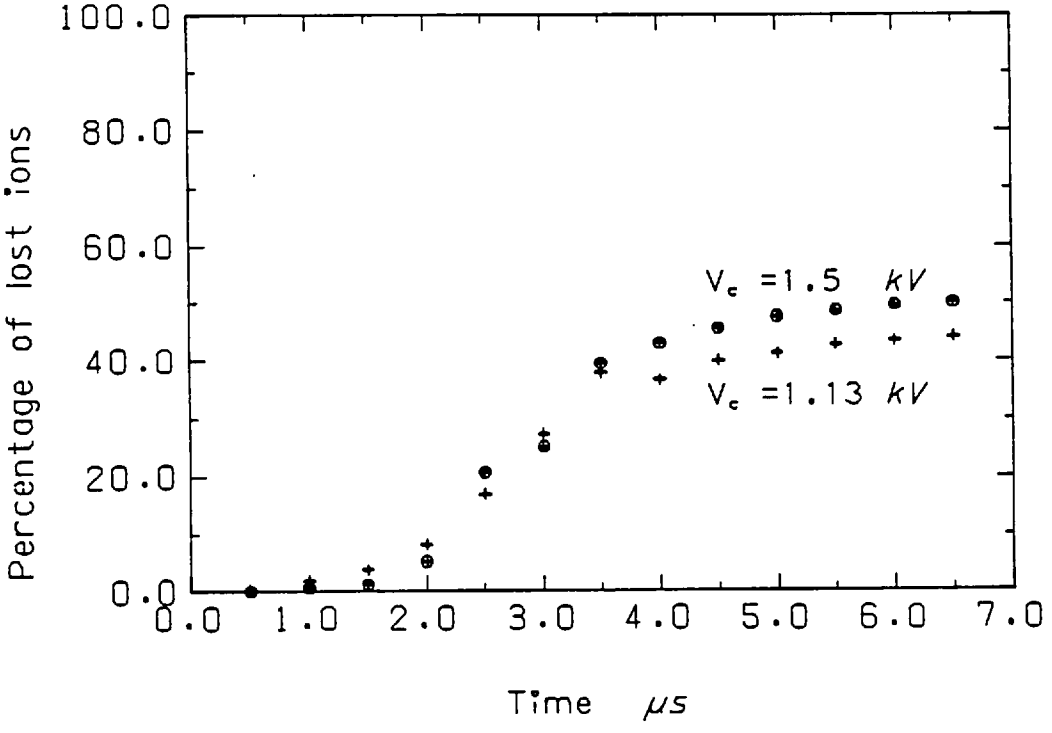

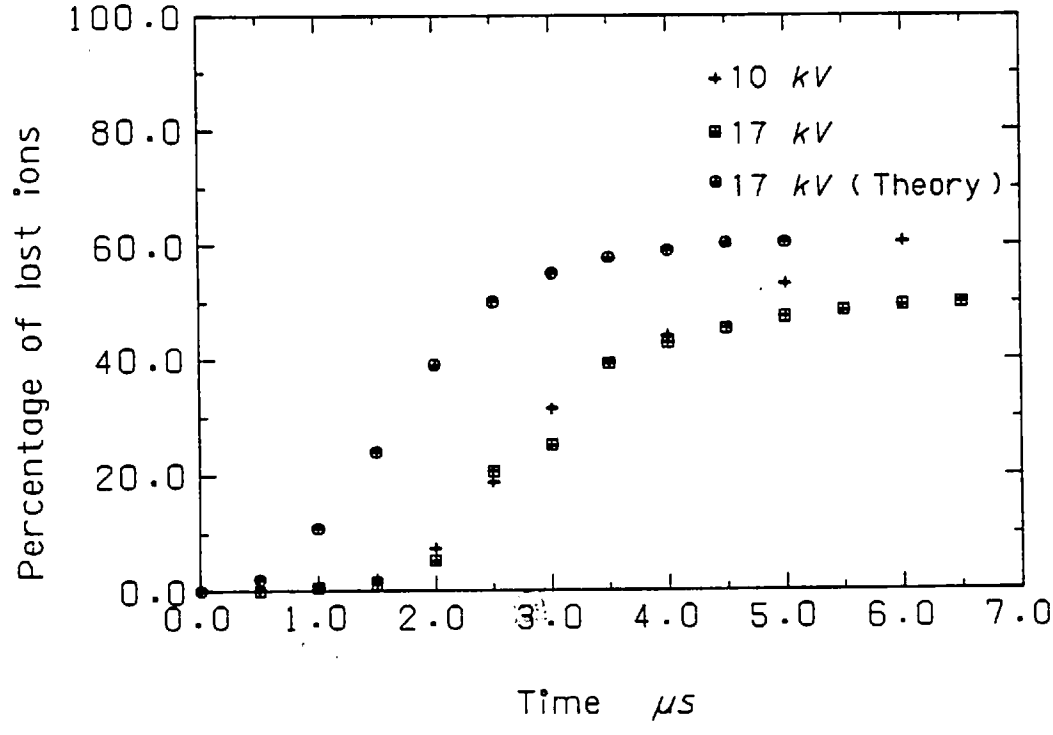

Fig. 5.10 Total particle loss expressed as percentage of the initial number of particles in a cusp volume. V_m = 10 and 17 kV, V_c = 1.5 kV, p = 3.5 mTorr. Calculated values are for $E_\phi = 10^4$ V/m, B^c= o.4 T, n = 4 x 10^{20} m^{-3}.

is higher for higher cusp magnetic fields.

For the high main bank voltage an average charge of 1.5 for the escaping particles is assumed, whereas a charge of 1.0 is assumed for the low voltage case. In the latter case the electron flux obtained with the same probe scales roughly as the square root of the electron-ion mass ratio. No comparison is available for the higher voltage case, but it is reasonable to assume a higher charge of lost ions in view of the fact that contained ions have a higher average charge in this case.

The FWHM of the plasma loss region is 7 mm, in good agreement with the value obtained from the single particle calculation described earlier.

Plasma containment time is obtained from

$$\tau_p = \frac{N}{\frac{dN}{dt}} \qquad 5.22$$

where N is the total number of particles in the plasma. N is obtained as the difference between the initial number of particles and the total number of lost particles up to a time t. τ_p is shown in Fig. 5.12. The plasma containment time is much longer than the energy containment time and is seen to decrease at the time of the initial loss, increasing at later times. Higher accelerating voltage improves the plasma containment time.

These results show that the loss in the Polytron can be greatly reduced provided that the initial distribution of particles is wholly within the contained region obtained from the single particle calculation. The results obtained using an auxiliary capacitor bank for the vertical magnetic field fired before the main bank (Chapter 4, Section 4.1) provide further evidence that this is the case.

5.6 Plasma displacement

The radial forces (acting along a major radius) on a unit length of the toroidal plasma column are:

f_s = force due to self magnetic field

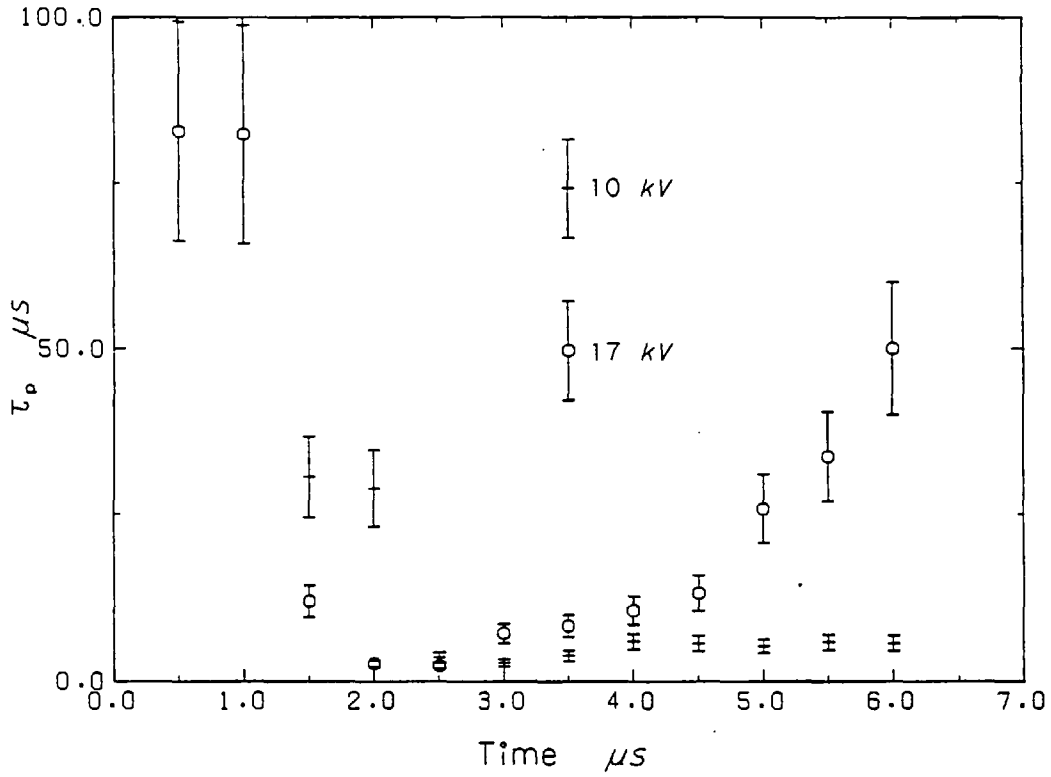

Fig. 5.12 Plasma containment time. V_m = 10 and 17 kV, V_c = 1.5 kV, p = 3.5 mTorr.

f_a = force due to vertical magnetic field

f_{cusp} = " " " cusp " "

f_{cen} = centrifugal force

f_s and f_a have been discussed in Chapter 3 (Sections 3.1 and 3.2) and are given by

$$f_s = \frac{\mu_o I^2}{4\pi R}\left[\ln\frac{8r}{a} - 0.75\right] \qquad (Eq^n\ 3.8)$$

$$f_a = IB_z \qquad (Eq^n\ 3.9)$$

f_{cusp} is due to the net difference of radial cusp magnetic pressures towards and away from major radius. This force is a function of r and ϕ. However, the cusp magnetic field can be approximated by (Kilkenny, 1972)

$$B = B_o I_1[k(r-R_o)]\sin(18\phi) \qquad 5.23$$

where B_o is the magnetic field at $r = R_o$, I_1 is the modified Bessel function of the first kind and $k = \pi/L$, L being the distance between cusp coils. The average value of cusp magnetic field along the ϕ coordinate between two cusp coils is

$$B_{av}(r) = \tfrac{1}{2}B_o I_1[k(r-R_o)] \qquad 5.24$$

The average cusp force is given by

$$f_{cusp} = \frac{a}{\mu_o}\left[B_{av}^2(r-a) - B_{av}^2(r+a)\right] \qquad 5.25$$

where a is the average plasma column radius.

f_{cen} is given by

$$f_{cen} = \rho\frac{v_\phi^2}{r} \qquad 5.26$$

where $\rho = \pi n m_i a^2$ is the mass per unit length.

The equation of motion for the plasma column is

$$\rho\frac{dv_r}{dt} = f_s + f_a + f_{cusp} + f_{cen} \qquad 5.27$$

The dominant term on the rhs of Equation 5.27 is f_s. f_{cen} is the least significant; for most cases f_{cen} can be neglected. Of the other two terms f_a is usually more important than f_{cusp}.

Using Equations 3.8, 3.9, 5.25 and 5.26, Equation 5.27 can be written as

$$\rho\frac{dv_r}{dt} = \left\{\frac{\mu_o I(t)}{4\pi r}\left[\ln\frac{8r}{a} - 0.75\right] - B_z(r,t)\right\} I(t) +$$

$$\frac{a}{\mu_o}\left[B_{av}^2(r-a) - B_{av}^2(r+a)\right] + \rho\frac{v_\phi^2(t)}{r} \qquad 5.28$$

It has the general form $\ddot{r} = f(r,t)$. The equation was integrated numerically using Milne's (1949) predictor corrector method. This method is appropriate in the present case, as the first derivative of r does not appear in the equation, and the integration can be performed in one step. A listing of the computer program used is given in

Appendix B. The experimentally determined values of plasma current, toroidal velocity, cusp and vertical magnetic field are used in the calculation.

Results of this integration for two values of accelerating field are shown in Figs. 5.13 and 5.14. In Fig. 5.13, for the lower field, three cases are displayed, cusp field only, vertical field only and both together. In this calculation a plasma radius of 1 cm is used. Also shown is the experimentally determined plasma position. In the case of both fields together there is good agreement between experimentally determined and theoretically predicted position. The calculation clearly shows that a vertical magnetic field is required to keep the plasma column away from the walls. In Fig. 5.14 a higher accelerating field is used, and two cases are considered, cusp field alone and cusp field with vertical field. A plasma radius of 1.5 cm is used and very good agreement is obtained. The use of the 1.5 cm radius is in agreement with the experimental value derived from spectral line emission spatial profiles.

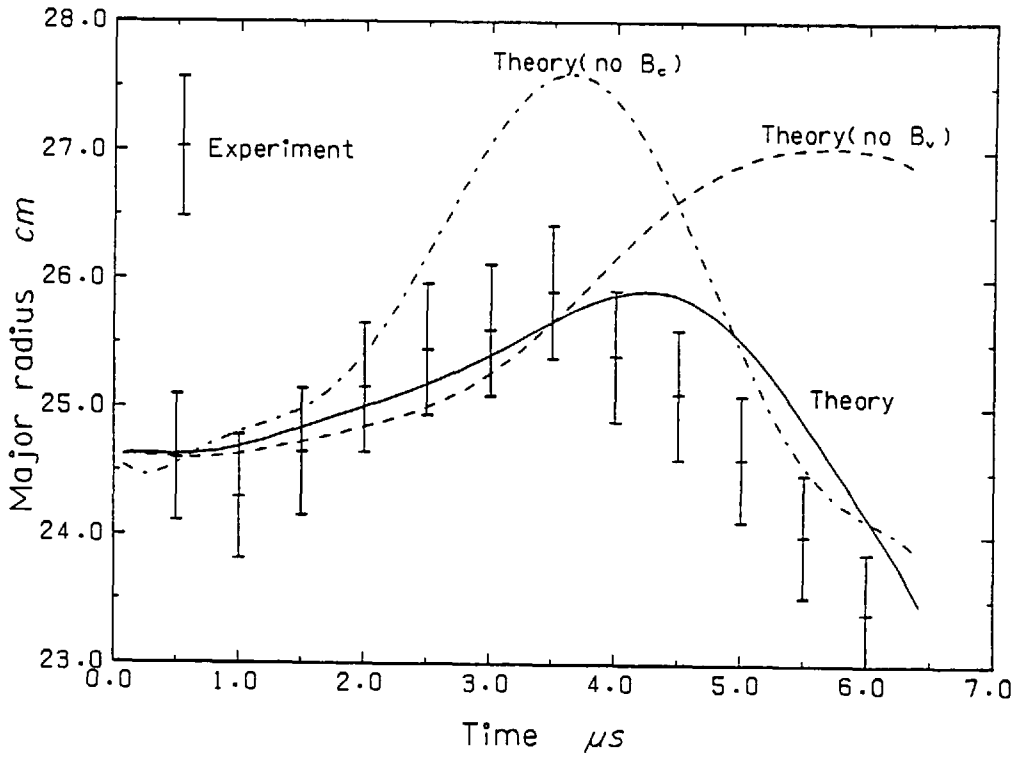

Fig. 5.13 Calculated and measured plasma major radius. V_m = 17 kV, V_c = 1.5 kV, p = 3.5 mTorr. The calculation is performed with B_{vert} only, B_{cusp} only and both. B_{vert} = 362 gauss.

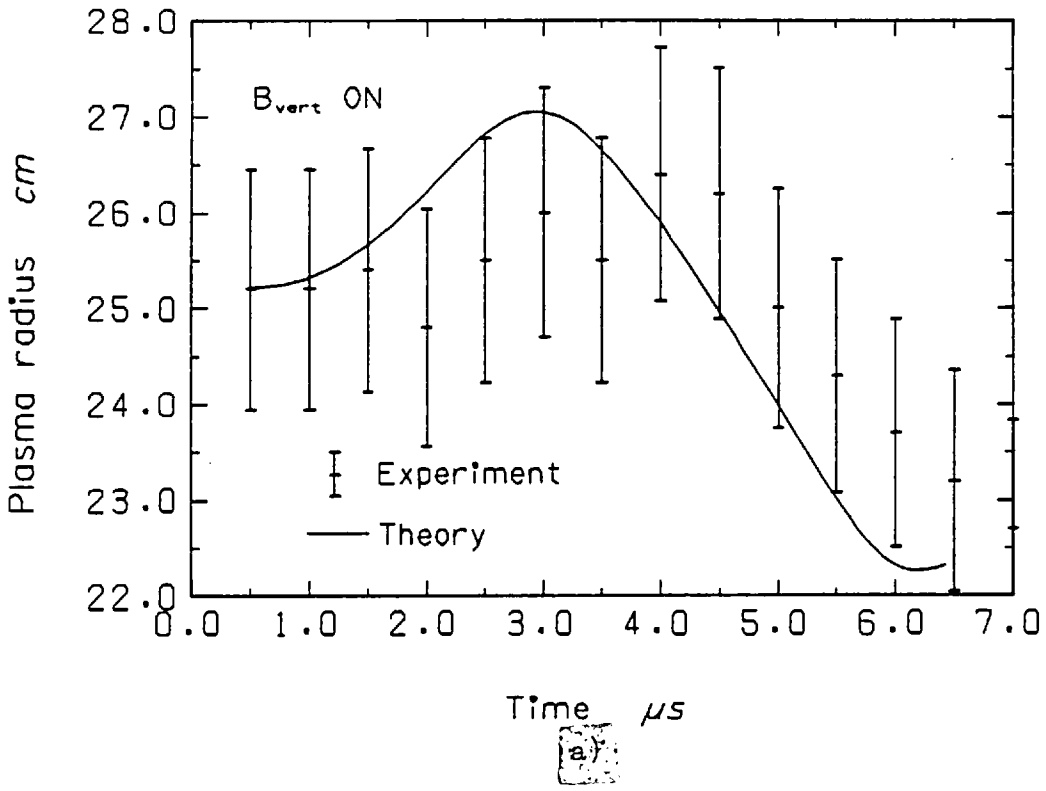

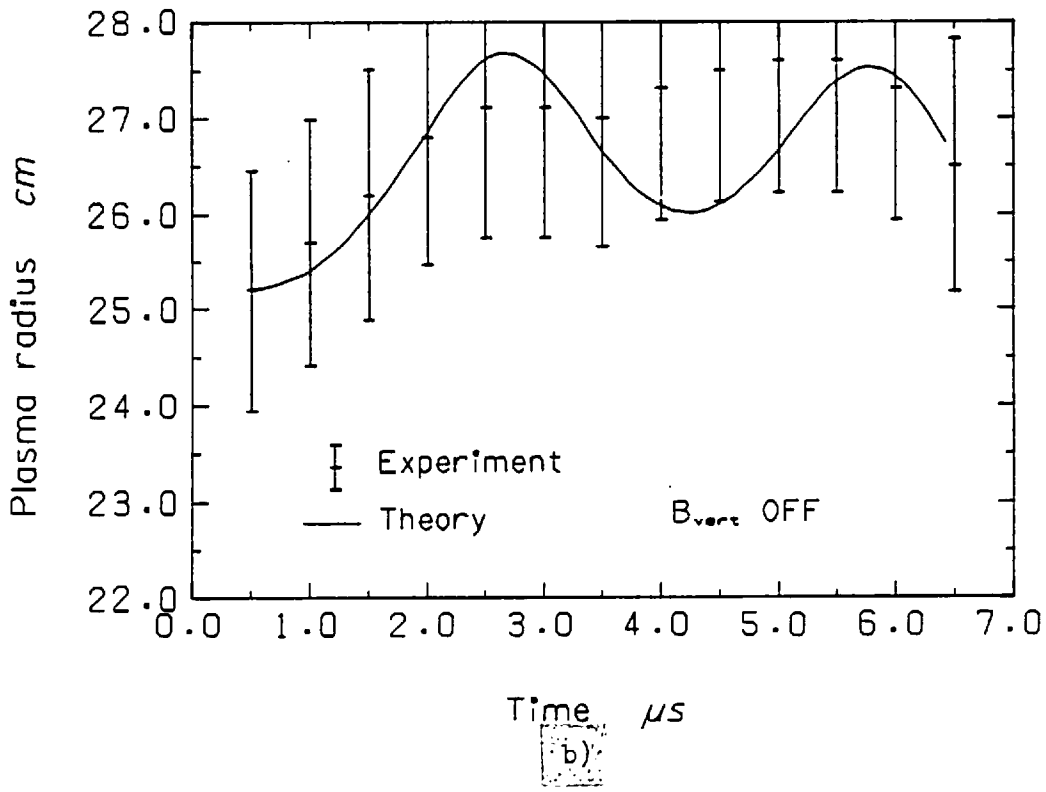

Fig. 5.14 Calculated and experimentally measured plasma major radius. V_m = 25 kV, V_c = 1.5 kV, p = 3.5 mTorr. (a) B_{vert} = 670 gauss; (b) B_{vert} = 0.

As mentioned in Chapter 4, the experimentally observed vertical plasma displacement has two components. One is dependent on cusp and main bank polarities, the displacement is in the direction $\underline{j}x\underline{B}$. The second component is always upwards, independent of cusp or main bank polarity (see Fig. 4.17).

An asymmetry which may be responsible for this behaviour is due to the fact that the quartz vessel minor axis does not lie exactly in the magnetic equatorial plane, but is 5 mm below it, so that the upper wall is closer to the plasma than the lower wall. The plasma position is determined by the cusp magnetic field minor axis. Impurities from the upper wall will reach the upper region of the plasma and get ionized earlier than the ones from the lower wall. Under these conditions an apparent upward motion would be observed. The apparent motion would be faster for a higher electric field. This is the behaviour observed in the experiment.

5.7 Polytron action and its cessation

The evidence presented indicates that the Polytron can be operated in the so-called 'Polytron regime'. The conditions for Polytron action have been given in Chapter 1 and will be discussed now in the light of the results obtained.

The condition

$$\omega\tau > 1 \qquad (\text{Eq}^{n}\ 1.1)$$

holds for radii larger than a few mm (see Section 5.4) and therefore Hall currents flow.

The condition

$$a_L \geq \frac{L}{2} \qquad (\text{Eq}^{n}\ 1.2)$$

holds for Argon ions but it does not hold for Hydrogen. Argon ions can therefore be accelerated.

The condition

$$\mu . ne \frac{E}{B^2} < \frac{2}{L} \qquad (\text{Eq}^{n}\ 1.3)$$

holds for the experimental conditions used.

These three conditions are essential for Polytron action to occur and are met in the present experiment for Argon ions.

The condition

$$v_\phi^2 >> \frac{2kT_i}{m_i} \qquad (Eq^n\ 1.4)$$

is satisfied as is apparent from Fig. 5.15 which shows the Mach number for two accelerating fields. Plasma leakage should therefore be small. This is consistent with Faraday cup measurements which show that the ion leakage is large only at about 1.5 μs when loss of ions from uncontained regions is dominant.

The condition

$$v_\phi^2 >> \frac{2kT_e}{m_e} \qquad (Eq^n\ 1.5)$$

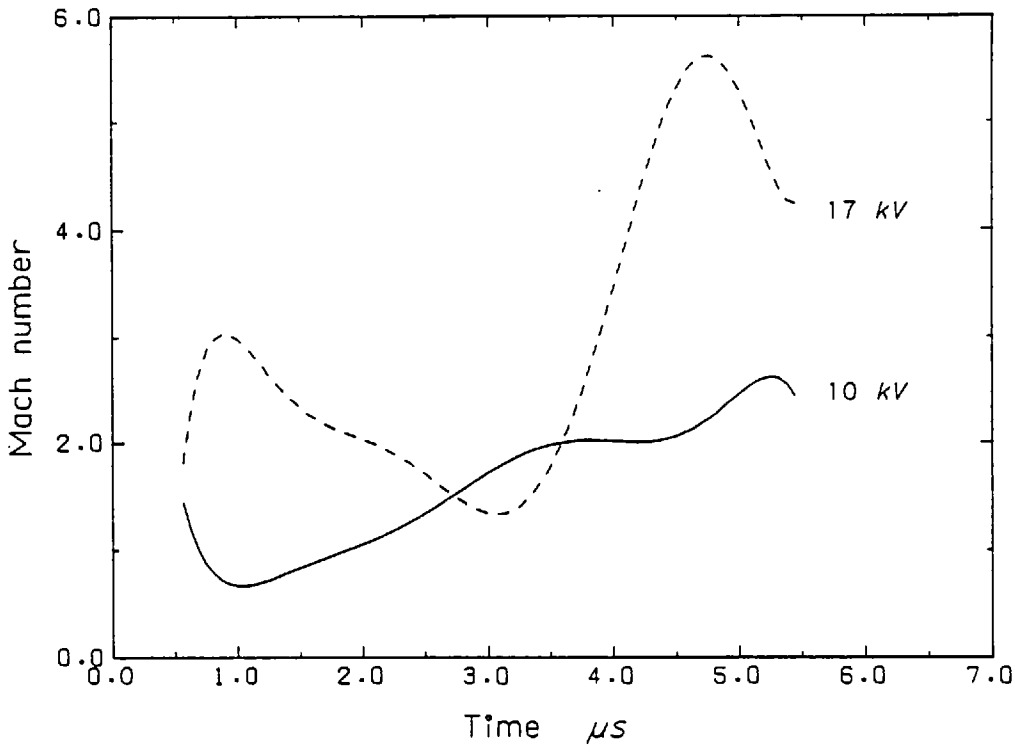

Fig. 5.15 Mach number as a function of time. V_m = 10 and 17 kV, V_c = 1.5 kV, p = 3.5 mTorr.

is certainly satisfied, therefore no two stream instability should be generated.

The condition

$$B_\theta << B \qquad (Eq^n\ 1.6)$$

is satisfied as the plasma poloidal magnetic field is at least an order of magnitude smaller than the cusp magnetic field. MHD stability is therefore ensured.

The condition

$$\mu_o I^2 < 8\pi Nk(T_e + T_i) \qquad (Eq^n\ 1.7)$$

is certainly satisfied in the experiment.

Thus it is apparent that the present device does operate in 'Polytron regime', although a steady state situation is not obtained. The acceleration time to reach steady state τ_a, given by Haines (1962) is

$$\tau_a = \frac{2}{\omega_{ci}} (\omega\tau + \frac{1}{\omega\tau}) \qquad 5.29$$

which for a typical value of Hall parameter of 10 is 15 μs, much longer than the discharge duration in the present device. The accelerating force disappears before the electric field drops to zero. The evidence seems to indicate that this disappearance of the accelerating force is due to neutral Argon and impurities released from the walls of the plasma vessel. The evidence can be summarized as follows:

a) The timescale for the force is only slightly dependent on cusp magnetic field, the effect does not appear to be associated with a cusp magnetic field effect.

b) The timescale is strongly dependent on the accelerating electric field, and is shorter for higher electric fields.

c) Wall deposits, final pressure measurements and impurity lines indicate that gas and material from the walls are released and redistributed.

d) Ion density, derived from momentum balance, increases immediately before the disappearance of the accelerating force.

Times between initial loss and force disappearance are given in Table 5.2, with the corresponding pump-down times to base pressure after the discharge. The time of flight of impurities is taken as the time difference between the time of peak plasma loss and the time at which the force disappears. The impurity velocity is obtained assuming that impurity atoms have to travel 3 cm to reach the core of the plasma.

Table 5.2

Velocity of impurities from walls and pump-down times

Main bank voltage (kV)	Impurity time of flight to plasma (μs)	Impurity velocity (cm/sec)	Pump-down time (min)
10	3.0	1.0	3
17	2.25	1.33	10
25	1.8	1.65	45

The binding energy of silica (SiO_2) is about 8 eV (Kaye and Laby, 1956), much smaller than the energy of ions lost to the wall. The energy required to generate the same number of atoms as the initial number of argon atoms in a cusp volume is 0.01 Joules, an order of magnitude smaller than the energy carried by lost ions during the initial loss. Therefore ions lost to the walls have enough energy to release significant numbers of wall atoms.

An influx of cold gas into the discharge increases the density and decreases electron temperature, as electron-electron energy equipartition time is 10 ns for $T_e \sim 20$ eV (Spitzer, 1967), and decreases ion temperature through charge exchange processes. A small particle influx causes an increase in the accelerating force, as long as the Hall parameter remains large. Using Spitzer's conductivity, the Hall parameter is

$$\omega\tau = 6 \frac{(2\pi k)^{3/2} \epsilon_o^2}{m_e^{1/2} e^3} \frac{B T_e^{3/2}}{\ln\Lambda\, n}$$

As further new particles get into the discharge a point is reached when the Hall parameter becomes small over the whole cross section of the discharge. Cooling down of electrons and increased density contribute to a decrease of the Hall parameter.

As the Hall parameter decreases, the radius of the electron carrying current channel increases. At the same time conductivity decreases, so it is probable that no drastic change in electron current occurs. The plasma current does not increase, as seen from the current wave form (Fig. 4.3).

If energy is fed into the plasma at a fast enough rate, the accelerating force should reappear as soon as the electron temperature is high enough. This is the case for the highest main bank voltage (25 kV, Fig. 4.8).

5.8 Stability

No major instabilities have been observed. There is no indication from the diagnostics used of large scale instability. Kilkenny (1972) observed what could be a Rayleigh-Taylor instability. This effect is not present with the vertical magnetic field.

Double probe measurements rule out the possibility of low frequency microinstabilities, although higher frequency ones might be present.

5.9 Summary

In the present device three distinct phases can be observed during the discharge. An initial phase, leading up to the initial loss, with acceleration and considerable ion and electron heating; a second phase after this loss and before the entry of gas and material from the walls, the centre of mass velocity of the ions rises continually during this stage; and a final third phase, the gas and material from the walls penetrate into the discharge, disrupt the acceleration process, and the accelerating force decreases or vanishes.

Ion heating is probably viscous. Ion temperature is higher than electron temperature. A classical heat conditivity is adequate to describe heat losses , heat loss occuring through a ring of width similar

to the electric field sheath and the particle loss widths.

Particle containment time and the total number of contained particles increase with increasing accelerating field.

No major instabilities are observed.

Chapter 6

CONCLUSIONS

As a culmination of this work modifications of the present device are discussed showing that it is possible to achieve a configuration in which negligible plasma losses are present.

The obvious design criteria are

(a) Suppression or reduction of initial loss.
(b) Capability of operating in deuterium.
(c) Increased accelerating field.
(d) Vertical magnetic field suitable for a wide range of plasma conditions.
(e) Longer timescale of the discharge, allowing the terminal velocity to be reached.

The last criterion will not be discussed here as it is a purely technological one and can be met.

The first three criteria are closely related and will be discussed jointly, after criterion (d).

Finally a discussion of a device using a different geometry, in which the magnetic and electric fields are orthogonal to the present device, is presented.

6.1 Vertical magnetic field

In the present system the value of accelerating electric field fixes the vertical magnetic field. The ratio of the two is essentially determined by the geometry of the induction rods. The plasma current has little effect on the vertical magnetic field.

Ideally the vertical magnetic field should be independent of the accelerating electric field and the system capable of sensing the plasma position and adjusting the vertical magnetic field accordingly. Unfortunately it is not possible to have two electrically independent inductive circuits in close proximity. Any change of current in one will induce an emf in the other and vice versa. The coefficient of coupling

C_c is given by

$$C_c = \frac{M_{ij}}{\sqrt{L_i L_j}} \qquad 6.1$$

where M_{ij} is the mutual inductance between circuits i and j and L_i and L_j their self-inductances. This coefficient is zero for no coupling and one for perfect coupling. In the present device its value is between 0.50 and 0.60, clearly a case of close coupling. However it is possible to have two sets of coils, one to generate most of the induced emf at the plasma position and the other to generate the vertical magnetic field without inducing a large emf in the plasma.

In Fig. 6.1 a circular loop carrying a current I is in the horizontal plane. In any plane P parallel to the horizontal there is a radius R_o for which the vertical magnetic field component is zero. For a time varying current the induced emf on a circle of radius R_o in the plane P is nevertheless non-zero. To illustrate this point the vertical magnetic field and the induced emf generated by two coaxial circular coils are calculated. A schematic diagram of the geometry is shown in Fig. 6.2. The coils are parallel and equidistant from the horizontal plane. The distance between coils is 0.18 m. The vertical component of the magnetic field and the induced emf are calculated at a point in the horizontal plane, radius 0.254 m, for different coil major radius. Both coils are connected in parallel to a 60 μF capacitor bank, with currents flowing in the same sense. Results of this calculation are shown in Fig. 6.3. The coils are assumed to have been made of a .01 m diameter wire. The vertical component of the magnetic field generated changes direction at a radius of 0.218 m. The induced emf on the other hand is always of the same polarity and is not very dependent on coil radius.

It is conceivable then to have a set of coils generating flux only (and hence induced electric field), whilst the required magnetic field is provided by a different set of coils. Ideally the magnetic field coils should be driven from a controllable source, capable of responding to the changes in plasma position. In practice this is difficult to achieve. However a far simpler approach can be implemented more readily, namely several coil sets, each set driven by a separate capacitor bank. To illustrate this a simple case has been solved. A hybrid system, in which part of the vertical magnetic field is generated by a set of coils

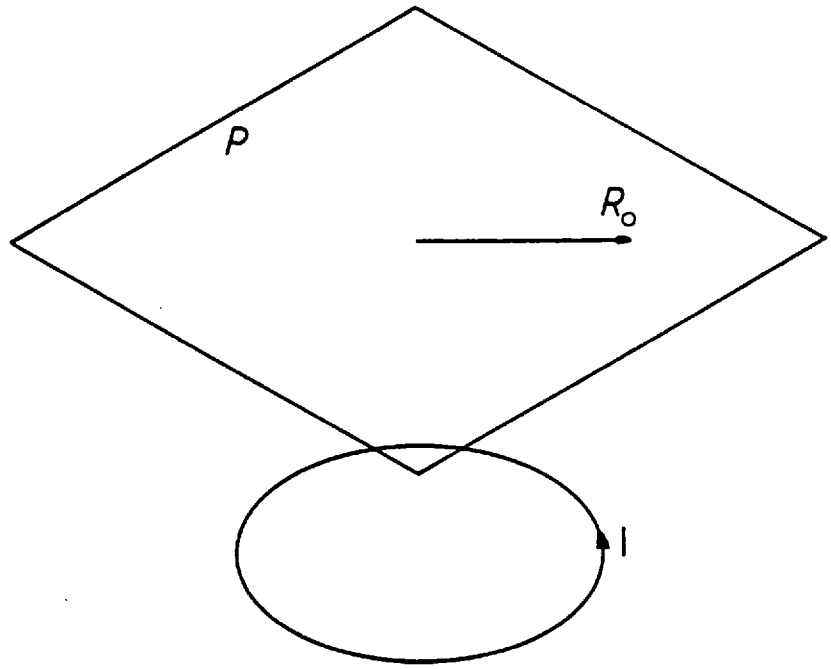

Fig. 6.1 Schematic diagram of a single circular current carrying coil in the horizontal plane (see text).

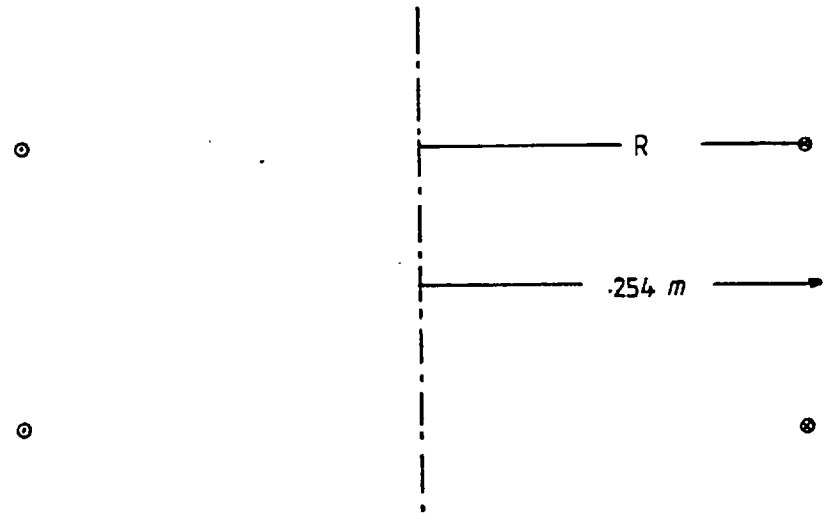

Fig. 6.2 Two coil configuration for which the vertical magnetic field and induced voltage are calculated. Results of this calculation are shown in Fig. 6.3.

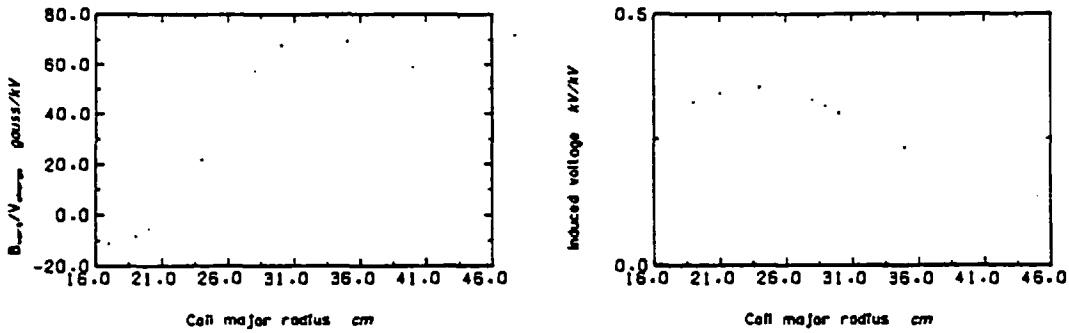

Fig. 6.3 Peak vertical magnetic field and induced voltage at R = 25.4 cm, Z = 0 per kV charging voltage of a 40 μF capacitor bank discharged through the coils.

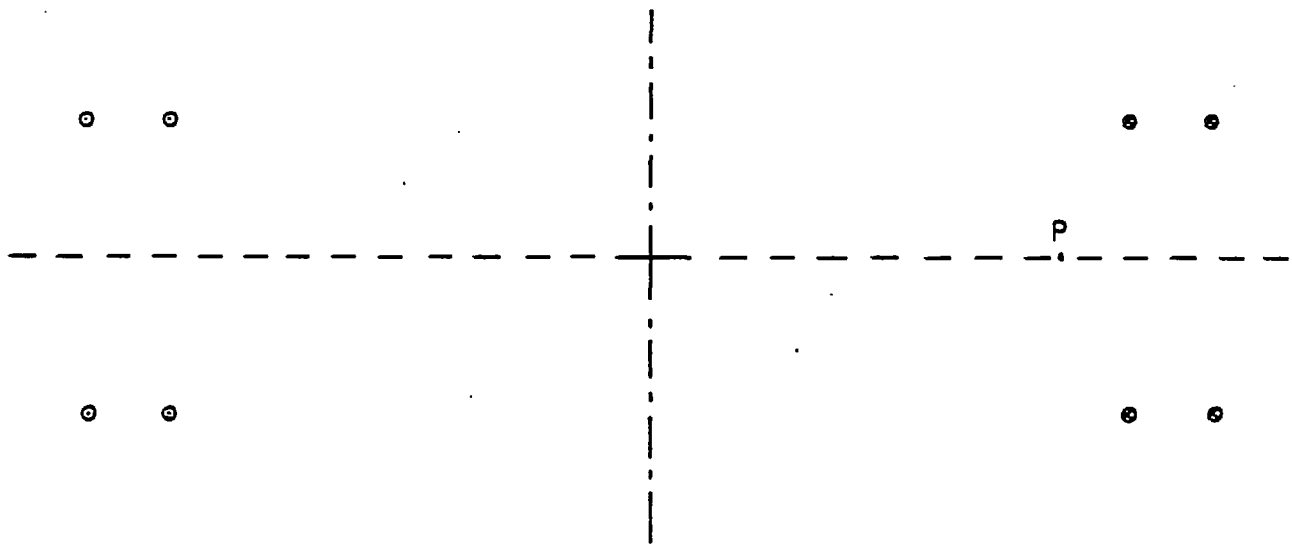

Fig. 6.4 Schematic diagram for system of induction rods to generate different magnetic field and induced voltages.

driven by a capacitor bank and the rest of the required magnetic field is provided by a set of coils whose current depends on the plasma position is used in Cleo (P Reynolds et al., 1974).

A system of n coupled linear circuits requires 2n coupled differential equations with constant coefficients. Using Laplace's method an algebraic system of equations of order 2n is obtained which allows the determination of the frequencies and damping coefficients. The case n = 2 can be solved analytically. Details of this solution are given in Smythe (1950).

A solution has been obtained for the geometry shown in schematic form in Fig. 6.4 in which two pairs of coils, radii 0.30 and 0.35 m, separated by 0.18 m, are used. Each pair is connected in parallel to a capacitor bank of capacitances of 40 and 4 μF. In order to provide a critically or overcritically damped discharge, two sets of series resistors are used: 3 and 1.5; 1.5 and 1.0 ohm. The induced emf is important only during the beginning of the discharge. The values of induced emf and vertical magnetic field as a function of time have been obtained for a point in the horizontal plane at a radius of 0.254 m. Results of this calculation are shown in Fig. 6.5. The vertical magnetic field obtained has the required time dependence for the present device, namely a fast risetime followed by a constant or slightly increasing phase. A different set of series resistors produces a marked difference in the magnetic fields obtained.

A change in the initial loss would change the plasma current shape, presumably making the "shoulder" usually present less noticeable. In that case the required magnetic field would be closer to a sinusoid, requiring undamped capacitor banks. The emf generated would be more important in this case.

A modular construction of capacitor banks and induction rods would make a rapid modification of vertical field possible, so a wide range of plasma conditions could be investigated.

6.2 The initial loss problem

It has been shown in the previous chapter than the initial loss is of major importance, leading to an eventual cessation of the acceleration

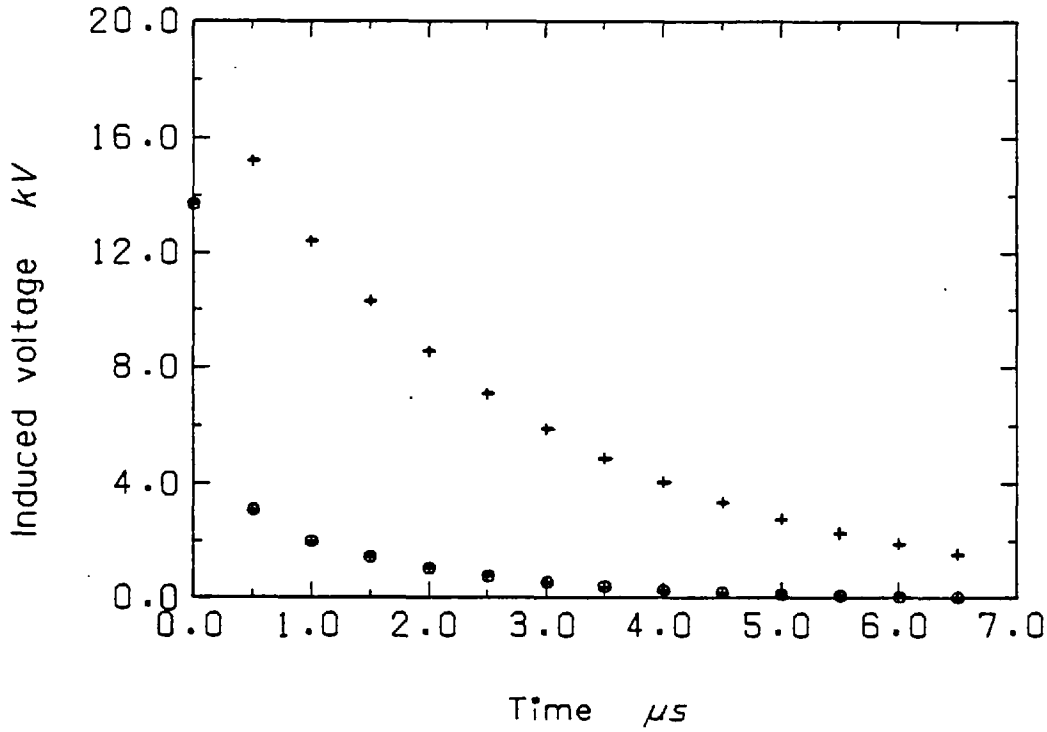

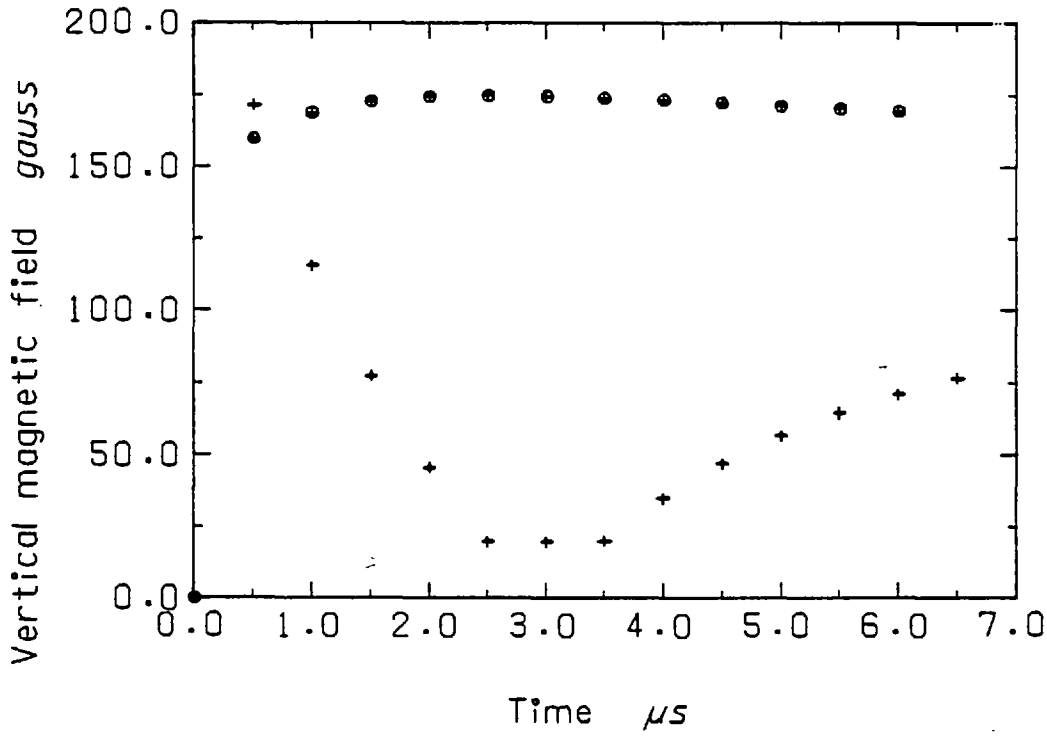

Fig. 6.5 Induced voltage and vertical magnetic field at R = 25.4 cm. Capacitor banks of 40 and 4 μF. (a) (+) 1.5 and 1.0 ohm series resistance, 10 and 30 kV charging voltage; (b) (⊕) 3 and 1.5 ohm series resistance, 30 and 10 kV charging voltage.

mechanism. It is of utmost importance to find means of either controlling or suppressing it. Two alternative schemes are possible and will be discussed in turn.

6.2.1 Suppression of reentry of wall material

The results obtained seem to show that the initial loss per se is not an important problem, the difficulty arising as the lost particles interact with the walls. This being the case, the obvious solution is to take the walls away and provide means of absorbing the lost particles. A practical scheme would be to have a large vacuum vessel with internal cusp and induction coils. Insulators in the external region of each cusp coil and coplanar with them are required to prevent current flow outside the cusp field; they must act as getters to prevent reentry of lost particles and generation of new particles.

This approach is used in the Torso device (Hamberger et al., 1975), in which a large vacuum vessel encloses the field generating coils. The technical problems in this case have been solved. The scheme should therefore be applicable to the Polytron.

6.2.2 Initial loss suppression

An alternative solution is to look for a magnetic field configuration for which losses are not present. An ideal configuration consisting of square field lines has been discussed by Kilkenny (1972) in which losses would not be present. In this configuration field lines are strictly parallel or perpendicular to the axis. Cylindrical coordinates are used, the magnetic field defined by

$$\begin{aligned} -\pi/4 < kz < \pi/4 \qquad & \underline{B}(r,\theta,z) = (0,0,B_o) \\ \pi/4 < kz < 3\pi/4 \qquad & \underline{B}(r,\theta,z) = (B_o\tfrac{kr}{2},0,0) \\ 3\pi/4 < kz < 5\pi/4 \qquad & \underline{B}(r,\theta,z) = (0,0,-B_o) \end{aligned} \tag{6.2}$$

where $k = \pi/L$, L being the separation between coils.

Suppose that at time $t = 0$, $r = r_o$ and $z = 0$, the particle is at rest. The axial equation of motion is

$$\frac{dv_z}{dt} = \frac{Ze}{m} E \quad \text{for} \quad 0 < kz < \pi/4 \tag{6.3}$$

where E is the applied electric field.

The particle will therefore enter the region where $B_r = 0$, with

$$\left.\begin{aligned} r &= r_o \\ z &= L/4 \end{aligned}\right\}, \quad v_z = \left(\frac{L}{2}\frac{ZeE}{m}\right)^{\frac{1}{2}}, \quad v_r = v_\theta = 0 \tag{6.4}$$

defining a new time origin. The non zero equations of motion for $\pi/4 < kz < 3\pi/4$ are

$$\frac{dv_\theta}{dt} = v_z\omega' \qquad \pi/4 < kz < \frac{3\pi}{4} \tag{6.5}$$

$$\frac{dv_z}{dt} = -v_\theta\omega' + \frac{Ze}{m}E$$

where $\omega' = \frac{ZeB_o}{m}\frac{kr}{2}$

solving

$$v_z = \frac{ZeE}{m\omega'}\sin\omega't + \left(\frac{L}{2}\frac{ZeE}{m}\right)^{\frac{1}{2}}\cos\omega't \tag{6.6}$$

and

$$v_\theta = \frac{ZeE}{m\omega'}(1 - \cos\omega't) + \left(\frac{L}{2}\frac{ZeE}{m}\right)^{\frac{1}{2}}\sin\omega't$$

Integrating, the v_z equation, we find that for an ion to pass into the region $z > 3L/4$ it is necessary that

$$\frac{ZeE}{m\omega'^2} + \left(\left(\frac{ZeE}{m\omega'^2}\right)^2 + \frac{L}{2}\frac{ZeE}{m\omega'^2}\right)^{\frac{1}{2}} \geq \frac{L}{2} \tag{6.7}$$

In terms of the Larmor radius a_L

$$a_L = \frac{ZeE}{m\omega'^2} \tag{6.8}$$

Equation 6.7 can be written as

$$\left(1 + \frac{L}{2a_L}\right)^{\frac{1}{2}} \geq \frac{L}{2a_L} - 1 \tag{6.9}$$

or

$$1 + \frac{L}{2a_L} \geq \left(\frac{L}{2a_L} - 1\right)^2 \qquad 6.10$$

which gives

$$3a_L > \frac{L}{2} \qquad 6.11$$

Equation 6.11 is a more exact condition than that given by Equation 1.2 which simply requires that the ion Larmor radius be greater than half the cusp separation. Thus with a square magnetic field distribution, the requirement on the Larmor radius is relaxed, and it becomes easier to accelerate deuterium ions. Note that Equation 6.11 has been obtained assuming a uniform electric field. It has been shown that in the experiment the accelerating electric field is present only in a narrow sheath region, the effect of which is to relax the inequality 6.11 even more. This is important as the number of cusps required is reduced, consequently the heat loss, which is linearly dependent on the number of cusps, is correspondingly reduced.

As ions cross into the region $kz > 3\pi/4$ the only radial motion they will experience will be towards the axis as the radial equation of motion will be

$$\frac{dv_r}{dt} = -\omega' v_\theta \qquad 6.12$$

Hence in this configuration there are no lost ions.

A magnetic field which is closer to square field lines than the present one can be obtained by using several thin coils instead of the single coil per cusp used at present. Essentially the several thin coils become one thick coil. Fig. 6.6 shows the calculated magnetic field lines for several multiple coil structures. The multiple coils are equally spaced filling half and 7/8 of the distance between cusps. The shape of the field lines becomes more square as the number of coils per cusp is increased, the region of large radial field becoming smaller. Using the same total current as in the single coil case, the maximum axial magnetic field is two thirds of the single coil case for the 15 coil configuration. This 15 coil configuration will be referred to as Polytron II.

The toroidal single particle code was used to evaluate the

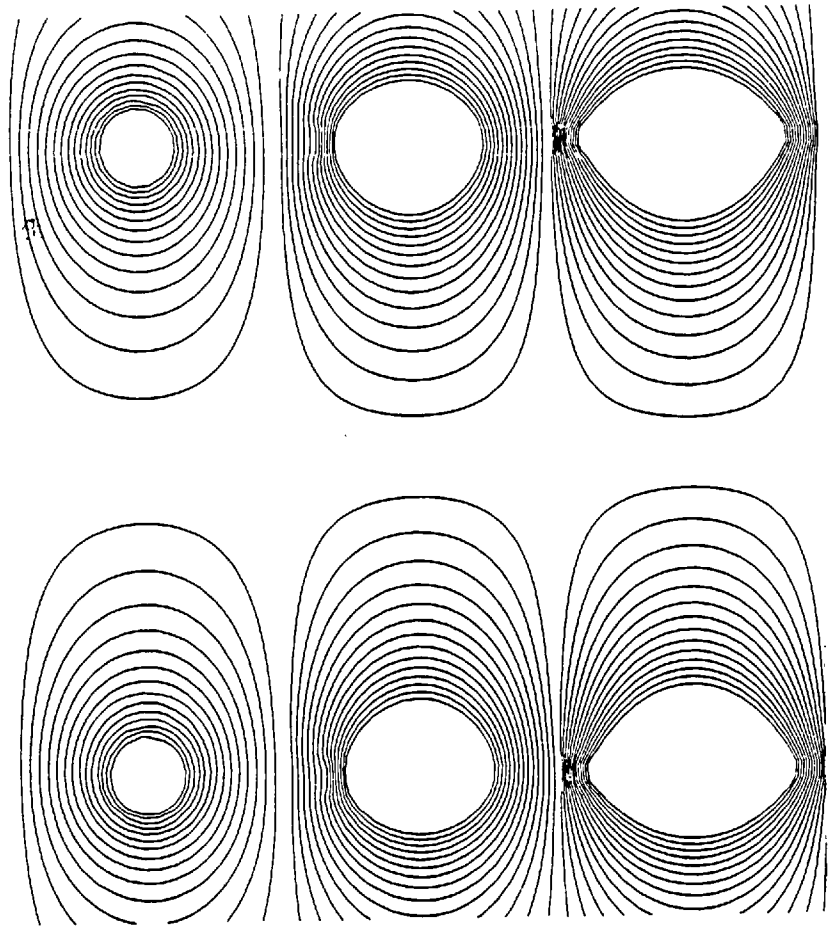

Fig. 6.6 Magnetic field lines for 1, 9 and 15 cusp coil configurations.

effectiveness of the different cusp field geometries. An increase of the accelerating field reduces plasma losses for any of the configurations studied. For the single and 15 coil configurations respectively the accelerating field required to obtain a no loss situation with hydrogen ions are 250 and 45 kV/m.

This multiple coil cusp configuration therefore appears to be extremely attractive and should be investigated further. It should be possible to obtain a further improvement by using a non-uniform distribution of coils in each cusp. A better approximation to square field lines should then be possible. Another parameter that can be altered is the aspect ratio of the cusp magnetic fields (ratio of radius to separation between cusps). The number of ring cusps used could be reduced, which would be accompanied by a reduction of heat losses. However, ion acceleration would be reduced if the electric field is maintained at the same value, so a compromise between the two requirements has to be reached. The problem of stability with a smaller number of cusps has also to be considered.

6.3 The orthogonal Polytron

This is an orthogonal transformation of the present device, in which the ring cusps are toroidal as opposed to the present poloidal ones. A linear orthogonal Polytron has been considered, a schematic diagram of it is shown in Fig. 6.7. A similar configuration was considered by Haines (1963) where he analysed a linear theta-pinch with Ioffe bars. Unlike a theta-pinch the orthogonal Polytron requires diffusion of the magnetic field into the plasma, as in the present device. The advantage of a linear orthogonal Polytron is that the induced emf is zero at the centre, where the magnetic field is zero, and increases linearly with radius. This means that there would be little electron current flowing, unlike the present device where a large electron current flows in regions of small $\omega\tau$. The electric field curvature should improve particle containment properties. A further advantage is that it is probable that no additional magnetic field would be required to maintain the plasma current contained, as the changing magnetic field used to induce the accelerating emf would have the same effect.

There are several experiments in which multiple magnetic fields

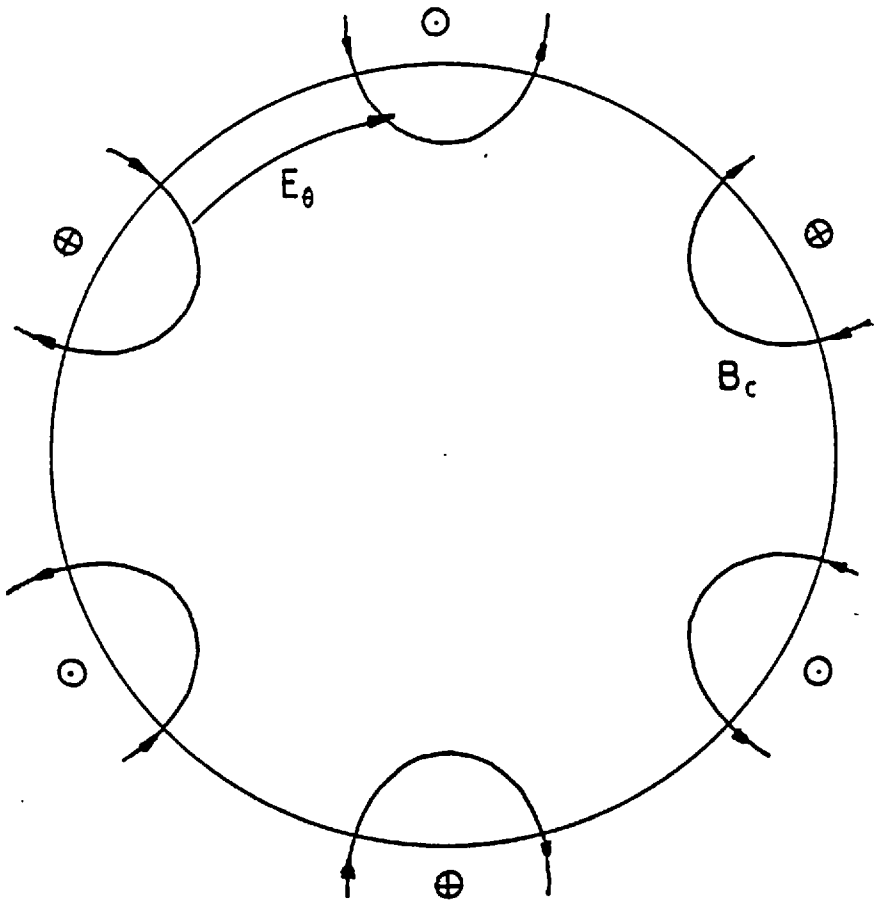

Fig. 6.7 Schematic diagram of orthogonal Polytron configuration

are used. One of these is a toroidal theta-pinch with a superimposed hexapole magnetic field (Von Gierke et al., 1966; Junker and Lotz, 1970). The hexapole field is used to prevent toroidal drift and reduce plasma losses. In 'Tormac', an experiment by Levine and co-workers (1970, 1972, 1973) an axisymmetric multipole field superimposed on a toroidal magnetic field is used. In this case the aim is to have the toroidal magnetic field diffusing into the plasma magnetic field and plasma being contained by the multipole field. In both experiments, unlike the orthogonal Polytron, the multipole fields would induce Hall currents at the plasma-multipole interface, preventing any multipole field penetration.

In order to study the loss properties of a linear orthogonal Polytron, a single particle computer simulation was developed. Details of this computer code are given in Appendix A. Several multipole fields were tried. Typical results for a hexapole field are shown in Fig. 6.8. The magnetic field lines for quadrupole and hexapole configurations are shown in Fig. 6.9. In this case, as in the present

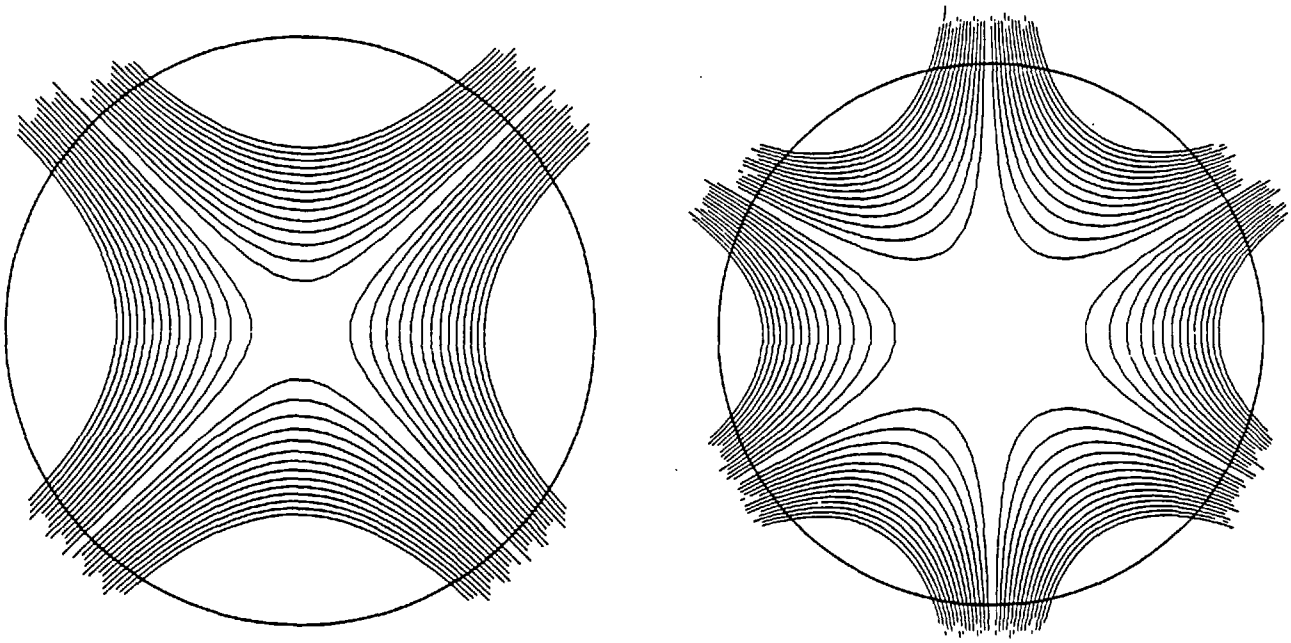

Fig. 6.8 Quadrupole and hexapole magnetic field lines

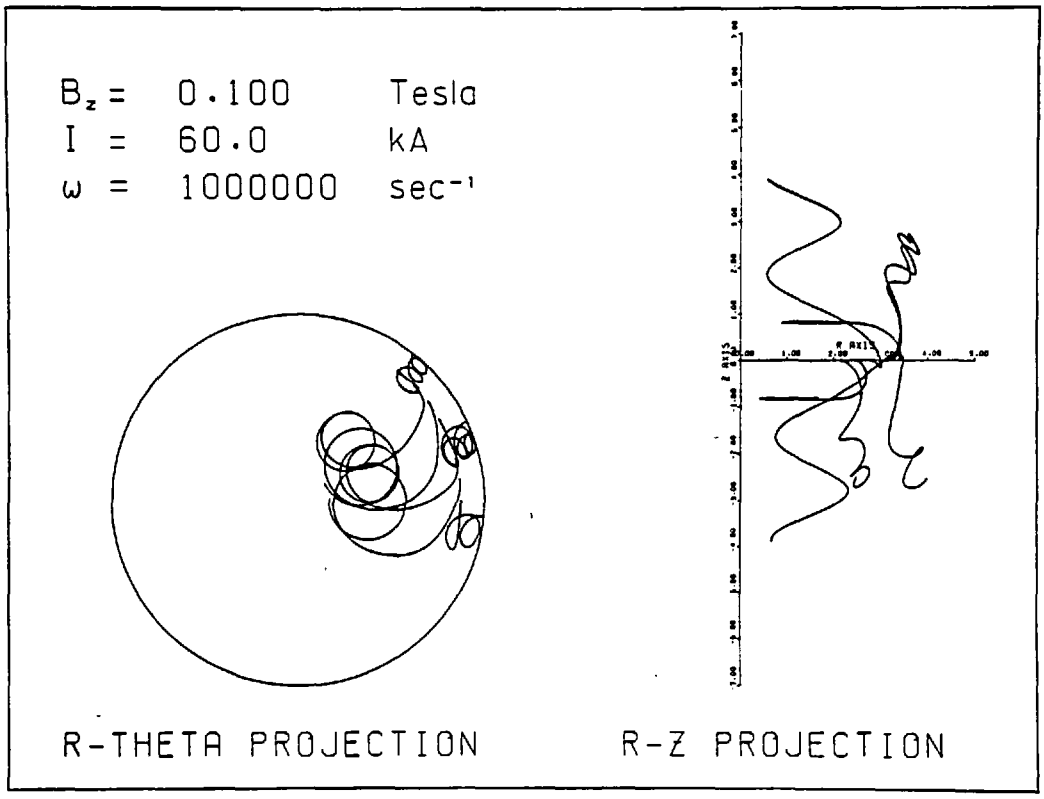

Fig. 6.9 Typical particle trajectories for the hexapole configuration

configuration, there are lost and contained ions. In order to decrease the number of lost ions an increased accelerating field is required. The induced emf is given by Equation 6.9.

$$E_\theta = -\frac{B_o \omega}{2} r \cos \omega t \qquad 6.13$$

where B_o is the peak magnetic field generated by the solenoid, ω the frequency of the capacitor driving circuit and r the radial position. The total emf can be increased by increasing the peak magnetic field or increasing the frequency or both. The frequency is determined by the time required to accelerate ions. Thus the only method of achieving a large E_θ is to increase B_o. A force towards the centre of the discharge given by

$$F_c = Zev_\theta B_z \qquad 6.14$$

will eventually drive the ions towards the axis. It seems that the ion loss cannot be suppressed without driving ions towards the axis of the device. The inclusion of electrons in this calculation might improve the situation.

The results obtained seem to indicate that the orthogonal Polytron is not a desirable development.

6.4 Heat and plasma losses

In the Polytron, as in any other open magnetic field containment device, heat losses along magnetic field lines are of considerable importance. It was shown in the present work that heat loss through electron conduction is the dominant loss process and that the energy containment time is much smaller than the plasma containment time (Chapter 5, sections 5.3 and 5.5). In the present experiment a classical heat conductivity is seen to be adequate to account for the observed losses. In a plasma of thermonuclear interest, in which the mean free path is larger than the plasma dimensions, the total heat flux is given by the free streaming value,

$$Q = \tfrac{1}{2} n_{ewall} \bar{v}_e \frac{3}{2} kT_e + \tfrac{1}{2} n_{iwall} \bar{v}_i \frac{3}{2} kT_i \qquad 6.15$$

where n_{ewall} and n_{iwall} are the electron and ion densities at the wall and $\bar{v}_e$ and $\bar{v}_i$ are the average velocities.

The total current must be zero, therefore the electron and ion particle fluxes are equal, i.e.

$$n_{ewall}\,\bar{v}_e = n_{iwall}\,\bar{v}_i \qquad 6.16$$

For a steady state situation quasi-neutrality dictates that

$$n_{ewall} = n_{iwall} \qquad 6.17$$

In the Polytron ions have a large centre of mass velocity, much larger than the thermal velocity, which reduces the number of ions that can be lost. An imbalance in electron and ion numbers results which is compensated by a radial outward electric field. This electric field slows down electrons and accelerates ions to equalize the ion and electron fluxes.

The number of ions that are lost is now estimated for a Maxwellian distribution displaced by a centre of mass velocity v_{cm}, parallel to the magnetic axis. Assuming that ion losses occur through a region of width w, ions whose transit time t_t along this region is equal to or smaller than the escape time to the wall t_e will be lost. An ion with a velocity v parallel to the magnetic axis has a transit time given by

$$t_t = \frac{w}{v} \qquad 6.18$$

The escape time determined from the acceleration in the electric field E_r from an initial velocity $v_\perp$ is

$$t_e = \frac{-v_\perp + v_\perp\sqrt{1 + \dfrac{2eE_r a_w}{kT_\perp}}}{\dfrac{2eE_r}{m}} \qquad 6.19$$

where $T_\perp$ is the temperature perpendicular to the ion centre of mass motion, $v_\perp = \sqrt{\dfrac{2kT_\perp}{m}}$ and a_w the wall radius.

Assuming that $a_w \simeq w$ and that the total potential difference is $= E_r a_w$, the critical parallel velocity v_c is given by

$$v_c = \frac{2e\phi}{mv_\perp\left(\sqrt{1+\frac{2e\phi}{kT_\perp}} - 1\right)} \qquad 6.20$$

The total number of lost ions n_{iL} is obtained from

$$n_{iL} = n\left(\frac{m_i}{2\pi kT_{||}}\right)^{\frac{1}{2}} \int_{-v_c}^{v_c} e^{-\frac{\frac{1}{2}m_i(v-v_{cm})^2}{kT_{||}}} dv \qquad 6.21$$

which gives

$$n_{iL} = \frac{n}{2}\left[\mathrm{erf}(M+M_c) - \mathrm{erf}(M-M_c)\right] \qquad 6.22$$

where M is the Mach number, $M_c = v_c/v_{||}$ and

$$\mathrm{erf}(x) = \frac{2}{\sqrt{\pi}} \int_o^x e^{-t^2}\, dt$$

The ion flux to the wall must be conserved, therefore

$$n_{iL}\sqrt{\frac{2kT_\perp}{m_i}} = n_{iwall}\sqrt{\frac{2(kT_\perp + e\phi)}{m_i}} \qquad 6.23$$

The electron density at wall is given by

$$n_{ewall} = n\, e^{-e\phi/kT_e} \qquad 6.24$$

From Equations 6.17, 6.22, 6.23 and 6.24 an equation for $e\phi$ is obtained:

$$\tfrac{1}{2}\left[\mathrm{erf}(M+M_c) - \mathrm{erf}(M-M_c)\right] = e^{-e\phi/kT_e}\sqrt{1+\frac{e\phi}{kT_\perp}} \qquad 6.25$$

from which the lost ions flux can be obtained for any particular Mach number.

The energy containment time τ_w is given by

$$\tau_w = \frac{W}{\frac{dW}{dt}}$$

Assuming that $T_e = T_\perp = T_{//} = T$, τ_w can be written as

$$\tau_w = \frac{\frac{3}{2} n kT \pi a^2 L_c}{\frac{3}{2} n e^{-e\phi/kT} kT \frac{2(kT + e\phi)}{m_i} w\pi D} \qquad 6.26$$

$$\tau_w = \frac{a^2 L_c}{e^{-e\phi/kT} \frac{2(kT + e\phi)}{m_i} wD}$$

where a is the plasma radius, L_c the cusp separation and D the diameter of the device. The plasma containment time is equal to the energy containment time because it has been assumed that each lost particle carries with it the same energy as it had in the plasma.

The fraction of lost ions $\alpha = n_{iL}/n$ is shown in Fig. 6.10. For plasma densities of 10^{18} and $10^{20} m^{-3}$ the Mach numbers for which $n\tau = 10^{14} cm^{-3} s$, obtained from Fig. 6.10 and Equation 6.26, are 8.4 and 7.15. The ratios of potential energy in the radial electric field to centre of mass energy are 0.34 and 0.33 for the two densities.

The values of α obtained show that in order to satisfy Lawson's criterion, a density at the wall nine orders of magnitude lower than the plasma density is required for the low filling density case. Such a low density would be very difficult to achieve. For the high density case the situation is less demanding, although it is not clear as to how it would be possible to maintain this density differential. The problem is similar to that of a divertor. Techniques such as differential pumping, maintaining cryogenic wall temperatures, etc. will be required.

In plasmas of thermonuclear interest bremsstrahlung and cyclotron radiation losses are most important. Heat conduction, cyclotron and bremsstrahlung radiation losses are given in Table 6.1 for a Polytron of thermonuclear interest with densities of 10^{18} and $10^{20} m^{-3}$. The relevant parameters used in the calculation are also given. Cyclotron

Table 6.1

Plasma parameters, power losses and power generated in the proposed Polytron R

Parameter				Units
Density	n	10^{18} ...	10^{20}	m^{-3}
Ion temperature	T_i	10^4	10^4	eV
Electron temperature	T_e	10^4	10^4	eV
Cusp length to major diameter	L_c/R	0.1	0.1	
Mach number	M	8.4	7.15	
Average magnetic field	B	0.1	1	Tesla
Accelerating electric field	E	60	1500	kV/m
Ion Larmor radius	a_L	0.14	0.014	m
Free accelerating time	t_a	2	0.07	μs
Plasma to magnetic field pressure	β	0.4	0.4	
Plasma radius	a	0.1	0.05	m
Major diameter	2R	6	6	m
Minor diameter	D	0.5	0.5	m
Heat conduction loss/m^3		.84	3.38×10^3	$W.m^{-3}$
Bremsstrahlung loss	P_b	1.69	1.69×10^4	$W.m^{-3}$
Cyclotron radiation loss	P_c	6.19	6.19×10^4	$W.m^{-3}$
D-T power density generation as charged particles	P_{DT}	15.4	1.54×10^5	$W.m^{-3}$
D-D power density generation as charged particles	P_{DD}	9.9×10^{-2}	9.9×10^2	$W.m^{-3}$

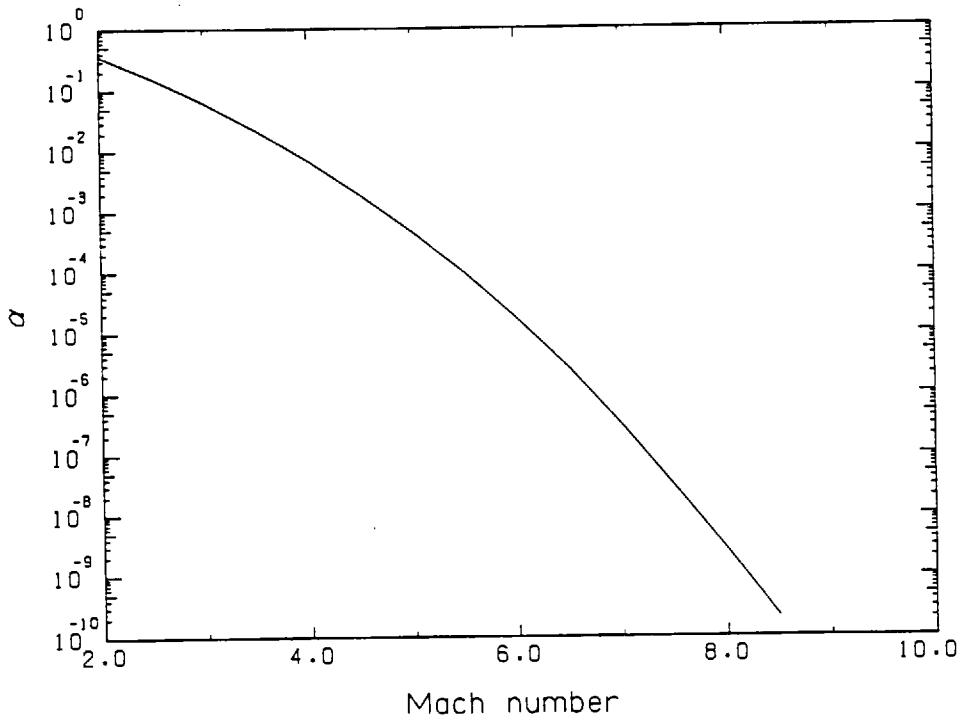

Fig. 6.10 Fraction of lost ions as a function of Mach number

radiation losses were calculated assuming that there is no plasma absorption. The number of cyclotron harmonics trapped in a medium of finite depth a is

$$m^* = (5700\ \beta Ba)^{1/6} \qquad 6.27$$

which for the two cases discussed gives 7.1 and 5.

At an electron temperature of 10 kV most of the cyclotron emission is in the first few harmonics (Trubnikov and Bazhanova, 1959). Therefore cyclotron radiation losses will be very small in a plasma with parameters as quoted. It is apparent that break-even can be obtained in a 1 : 1 D-T mixture, but not in pure deuterium. The heat loss width used in the calculation is the ion Larmor radius, although it is possible that this loss width is smaller, of the order of $(a_i a_e)^{\frac{1}{2}}$ (Haines, 1977) or even $2a_e$ (Kilkenny, 1976).

The condition obtained by Dunnett (1968) from Equations 1.2 and 1.3 which requires the ion collisionless skin depth to be much larger than the plasma characteristic length is violated for a 10^{20} m^{-3} density. However, the experimental evidence shows that even for a situation with a skin depth of the same order as the plasma dimensions the accelerating force is proportional to the number of particles present (Fig. 4.7). In the high density case the Bennett relation (Equation 1.7) is also violated. Nevertheless, the presence of the cusp magnetic field should prevent pinching in view of the fact that β is small (~ 0.4). Some compression of the cusp magnetic field counteracts the condition on the ion collisionless skin depth since the cusp field will tend to be strengthened in the plasma rather than weakened.

The plasma parameters given in Table 6.1 are chosen so that the criteria for Polytron action are met. The plasma density has already been discussed. The ion temperature is chosen to obtain fusion in a 1 : 1 D-T mixture. The electron temperature has been assumed equal to the ion temperature because the electron ion energy equipartition time is 0.6 s which is shorter than the timescale of the experiment envisaged. Plasma density and temperatures determine the Mach number required to satisfy Lawson's criterion. The cusp magnetic field has to be large enough so that $\omega\tau >> 1$ (Equation 1.1) and its energy density has to be large enough to be able to deflect the ion flow. This condition is given by Haines (1962) as

$$\frac{B^2}{2\mu_o} > \tfrac{1}{2} n m_i v_{cm}^2 \theta \qquad 6.28$$

where

$$\theta = \frac{1}{M^2} + \frac{L_c^2}{R^2}$$

and R is the major radius of the torus. Chosing a value of L_c/R allows to calculate the cusp magnetic field required. The electric field is obtained from the requirement that the ion Larmor radius $a_L = \frac{mE}{eB^2}$ has to be larger than the radial cusp magnetic field region (Equations 1.2 and 6.11).

The initial plasma radius is obtained from the result of particle simulation in which the contained plasma volume scales as E/B^2.

The free acceleration time t_a is defined as

$$t_a = \frac{v_{cm}}{a} = \frac{m v_{cm}}{eE} \qquad 6.29$$

Bremsstrahlung losses are given by

$$P_b = \frac{n_e n_i}{m_e \hbar c^3} \left(\frac{e^2}{4\pi\varepsilon_o}\right)^3 \frac{16}{3} \left(\frac{2\pi kT}{3m_e}\right)^{\frac{1}{2}} \qquad 6.30$$

Cyclotron radiation losses are obtained from

$$P_c = \frac{e^4 B^2 n_e kT}{3\pi \varepsilon_o c^3 m_e^3} \qquad 6.31$$

Charged particle D-T and D-D power generation is obtained from

$$P_{D-T} = 5.6 \times 10^{-13} n_D n_T (\overline{\sigma v})_{DT} \quad \text{Watt/cm}^3 \qquad 6.32$$

$$P_{D-D} = 3.3 \times 10^{-13} n_D^2 (\overline{\sigma v})_{DD} \quad \text{Watt/cm}^3 \qquad 6.33$$

where $\overline{\sigma v}$ are fusion reaction cross sections averaged over a Maxwellian distribution. The D-T energy equipartition time is of the order of 10^{-2} s. Therefore between the end of the acceleration time and the equipartition time a differential velocity between deuterium and tritium will exist. This velocity differential should increase the fusion reaction rate, as in the case of two components tokamaks (Furth, 1975).

The parameters which are free and are chosen are density, temperature and the ratio L_c/R. From these the values of M, B, E, a_L, a, t_a, and β are calculated, from which the values of power losses and power generation are estimated.

6.5 Concluding remarks

It has been shown that the present device operates in what has been described as 'Polytron regime' in Argon. Ion heating is seen to be mainly viscous, whereas electron heating is resistive. Particle and energy losses are seen to occur mainly through a thin region near the ring cusp. Particle losses decrease with increasing accelerating electric field as predicted by theoretical models.

Application of the vertical magnetic field led to suppression of the outward toroidal displacement leading to greatly increased confinement.

Future work should be centred on Polytron II, as the elimination of initial loss is possible with easily obtainable electric fields. The elimination of initial loss would allow the detailed study of the sheath region, role of whistler waves in its formation and possible presence of other waves like the runaway electron induced two-stream instability. To this end, special care should be taken in the accelerating field design, so that no high frequency components are present that would confuse the experimental interpretation.

Before a toroidal Polytron II is built, the properties of the modified magnetic cusp geometry should be studied experimentally, especially as regards the initial loss mechanism. A linear Polytron II would be best suited for this purpose. When the predictions of the single particle calculation are experimentally checked then a toroidal Polytron II experiment should be set up and energy loss and ion heating studied in detail. The potential of the Polytron configuration as a fusion device will then have been properly assessed.

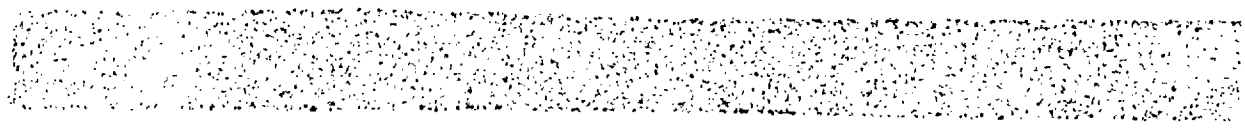

APPENDIX A

Single Particle Trajectory Calculation in the Orthogonal Polytron

Ion trajectories have been calculated in the Orthogonal Polytron assuming that electrons are tied to the magnetic field lines (large Hall parameter) and therefore can be neglected. No self-consistent electric or magnetic fields are included. Cylindrical coordinates are used. Fig. A.1 shows in schematic form the geometry used. The magnetic field is generated by a set of parallel conductors (six for the case shown in Fig. A.1) carrying currents in alternating directions. The induced accelerating electric field is generated by an infinitely long solenoid, whose current has a sinusoidal time variation of frequency ω.

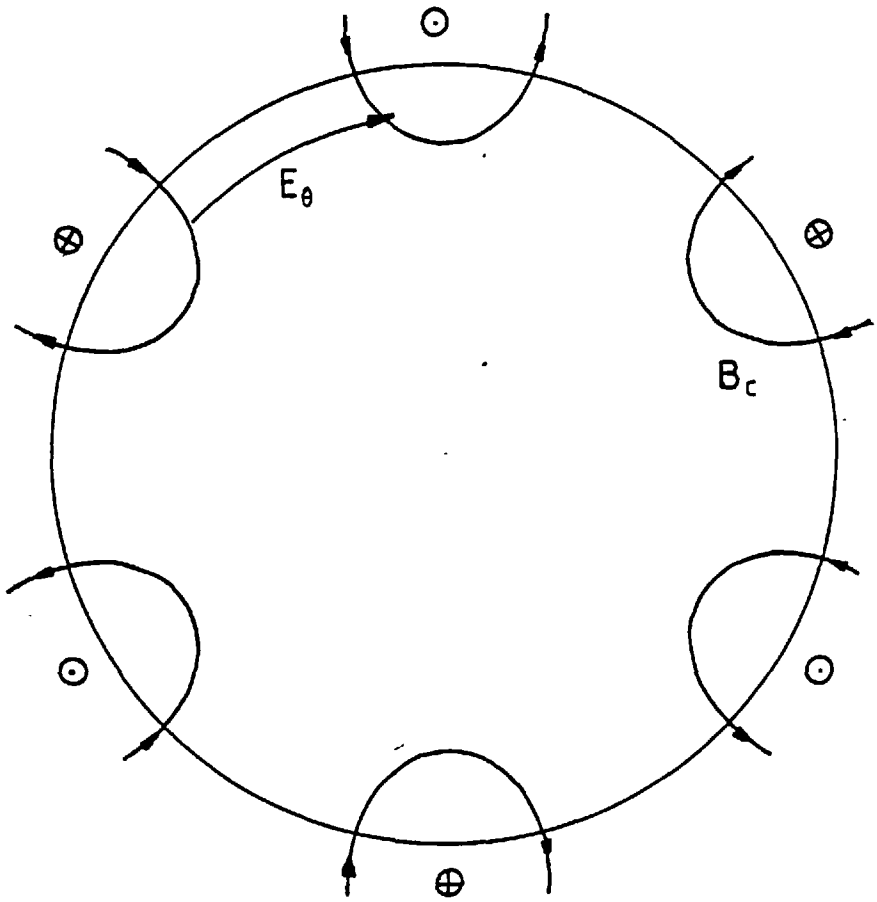

Fig. A.1

The equation of motion for a charged particle of charge q and mass m in electric and magnetic fields is

$$m \frac{d\underline{v}}{dt} = q(\underline{E} + \underline{v} \times \underline{B}) \qquad \text{A.1}$$

where

$$\underline{v} = \frac{d\underline{r}}{dt}$$

In cases with symmetry, it is advantageous to use canonical equations of motion. If Q_i and P_i are the canonical coordinates the corresponding equations of motion are

$$\dot{Q}_i = \frac{\partial H}{\partial P_i}$$

$$\dot{P}_i = -\frac{\partial H}{\partial Q_i} \qquad \text{A.2}$$

where H is the Hamiltonian.

If the Hamiltonian does not depend on one of the coordinates Q_k, then

$$\dot{P}_k = 0 \qquad \text{A.3}$$

therefore P_k is a constant of motion.

In the present case the Hamiltonian is independent of the z coordinate, therefore the canonical angular momentum P_z is

$$P_z = mv_z + qA_z = \text{constant} \qquad \text{A.4}$$

where A_z is the z component of the vector potential.

The velocity v_z can thus be obtained without integrating the corresponding equation A.1. The number of equations to integrate is reduced to five.

The equations used are:

$$m \frac{dv_r}{dt} = q(v_\theta B_z - v_z B_\theta) + m v_\theta^2 / r$$

$$m \frac{dv_\theta}{dt} = q(E_\theta + v_z B_r - v_r B_z) - m \frac{v_r v_\theta}{r}$$

$$\frac{dr}{dt} = v_r \qquad \text{A.5}$$

$$\frac{d\theta}{dt} = \frac{v_\theta}{r}$$

$$\frac{dz}{dt} = v_z$$

The magnetic vector potential of an infinitely long straight current filament is given by (Durand, 1960)

$$A_r = A_\theta = 0 \qquad \text{A.6}$$

$$A_z = \frac{\mu_o I}{2\pi} \ln \frac{r_1}{r_o}$$

where r_1 is the distance from the point under consideration to the current filament and r_o the distance at which the vector potential is zero.

The magnetic field is obtained from

$$B_r = \frac{1}{r} \frac{\partial A_z}{\partial \theta} \qquad \text{A.7}$$

$$B_\theta = - \frac{\partial A_z}{\partial r}$$

The vector potential of several current carrying conductors can be obtained by superposition. For a set of z_n infinitely long and parallel conductors, with currents I and -I in adjacent conductors, the total vector potential is

$$A_z = \frac{\mu_o I}{2\pi} \ln \frac{r_1 \, r_3 \cdots r_{2n-1}}{r_2 \, r_4 \cdots r_{2n}} \qquad \text{A.8}$$

where r_i is the distance from the i conductor to the point considered.

The induced electric field is obtained from

$$\nabla \times E = -\frac{\partial \underline{B}}{\partial t} \qquad A.9$$

The only time varying magnetic field is the solenoid field and is given by

$$B_z = B_o \sin \omega t$$
$$B_r = B_\theta = 0 \qquad A.10$$

The poloidal electric field E_θ induced by the current in the solenoid can be obtained by integrating Equation A.9 over the surface of a circular disc of radius r centred on axis. Thus

$$\int \nabla \times \underline{E} \cdot d\underline{s} = -\frac{\partial}{\partial t} \underline{B} \cdot d\underline{s}$$

giving A.11

$$E_\theta = -\frac{\omega B_o r}{2} \cos \omega t$$

Using electric and magnetic fields from Equations A.11 and A.7 Equations A.5 have been integrated numerically by a modified Runge-Kutta technique developed by Merson (Lance, 1961) in which the integrating error can be estimated and the step size varied accordingly. A limitation on step size is obtained at small radii

$$\Delta t < \frac{r}{\frac{dr}{dt}} \qquad A.12$$

The electric and magnetic fields are calculated for each point, as the exact shape of the field lines was considered necessary to give an accurate representation of the loss of particles. No self-consistent magnetic or electric fields due to plasma current or charge redistribution have been included. Results of this calculation have been given in Chapter 6.

A listing of the program used follows.

```
      PROGRAM TPA1(OUTPUT,TAPE6,TAPE62)
C    THIS PROGRAM CALCULATES THE TRAJECTORIES OF PARTICLES FOR
C   THE ORTHOGONAL POLYTRON
C
C
      DIMENSION Y(6),DER(6)
      COMMON /FIELD/ OMEGA,BZ,I
      REAL I
C
C    SET ERROR
C
      ERROR=1.0E-1
      ERL=ERROR/32.0
C
C
C    SET MAXIMUN AXIAL MAGNETIC FIELD
C    AND FREQUENCY
C
C
      OMEGA=1.0E5
      BZ=0.05
      I=3.0E4
C
C
C     INITIAL CONDITIONS FOR PARTICLES
C
C
      DO 999 N1=1,3
      DO 999 N2=1,1
      Y(4)=0.0
      Y(5)=0.0
      Y(6)=0.0
      Y(1)=0.005*FLOAT(3-N2)
      Y(2)= 3.1416/2+.1*FLOAT(N1)
      Y(3)=0.0
C
C
      CALL BEGIN(X,Y,DER,H,ERROR,ERL,N1,N2)
      CALL SOLVE(X,Y,DER,H,ERROR,ERL,N1)
  999 CONTINUE
      CALL ENPLOT
      REWIND6
      STOP
      END
C
C
C
C




      SUBROUTINE SOLVE(X,Y,DER,H,ERROR,ERL,NPAR)
C
C
C    MAIN BODY OF THE INTEGRATION
C
C
      COMMON R,Z
      COMMON /COEF/ AK(5,6)
      LOGICAL L
      DIMENSION Y(6),DER(6),YLAST(6)
C
C
C
      NSTEP=7000
      XMAX=1.0E-5
      RMAX=0.04
      ITIME=1
      DO 700 J=1,NSTEP
      NS=J
  701 CONTINUE
      XLAST=X
      DO 703 J1=1,6
      YLAST(J1)=Y(J1)
  703 CONTINUE
      L=.TRUE.
C
      CALL MERSON(X,Y,H,6,DER,AK)
```

```
      CALL CHECK(H,AK,ERROR,ERL,L)
      IF(L) GO TO 705
      X=XLAST
      DO 704 J=1,6
      Y(J)=YLAST(J2)
  704 CONTINUE
      GO TO 701
  705 CONTINUE
      TIME=.1E-6*FLOAT(ITIME)
C
C
C   FIND OUT WHETHER GOT TO PLOTTING
C   TIME AND DO THE PLOTTING
C
C
      IF(X.LT.TIME) GO TO 711
      ANEW=TIME-XLAST
      CALL INTERCON(XLAST,YLAST,ANEW,6,DER,AK)
      CALL INTRPO(XLAST,ANEW,YLAST,ITIME,1)
      TEST=FLOAT(ITIME)/3.-FLOAT(ITIME/2)
      IF(TEST.LT..5) IN=30
      IF(TEST.GT..5) IN=15
      CALL INTERVAL(IN)
  711 CONTINUE
C
C
C
      IF(X.GT.XMAX.OR.Y(1).GT.RMAX) GO TO 702
  700 CONTINUE
  702 WRITE(6,710) NS
      RETURN
  710 FORMAT(*    NUMBER OF STEPS=*,I10)
      END
C
C
C
```

```
      SUBROUTINE BEGIN(X,Y,DER,H,ERROR,ERL,N1,N2)
      LOGICAL L
      DIMENSION Y(6),DER(6),YLAST(6)
C
C     CALCULATES INITIAL STEP SIZE, STARTS PLOTTING
C
C
      REAL I
      COMMON P,Z
      COMMON /FIELD/  OMEGA,BZ,I
      COMMON /COEF/ AK(5,5)
      L=.TRUE.
      H=1.0E-8
      X=0.
      ITEST=0
C
C
C
      XLAST=X
      DO 1 J=1,6
      YLAST(J)=Y(J)
    1 CONTINUE
      L=.TRUE.
      ITEST=ITEST+1
      CALL DERIV(X,Y,DER)
      CALL INTRPO(X,Y,H,6,DER,AK)
      CALL CHECK(H,AK,ERROR,ERL,L)
      IF(ITEST.EQ.30) STOP
      IF(L) GO TO 3
      X=XLAST
      DO 2 J=1,6
      Y(J)=YLAST(J)
    2 CONTINUE
      GO TO 1
C
C
C    IF ACCURACY INSUFFICIENT, TRY AGAIN
C    WITH H HALVED.
C
C
    3 CONTINUE
```

```
C
C     DO THE INITIAL PLOTTING,SET ORIGIN , AXIS
C      LEGENDS
C
      IF(N.EQ.1.AND.NZ.EQ.1) CALL START(2)
      IF(N.EQ.1.AND.NZ.EQ.1) CALL PLOTS(2)
      IF(NZ.EQ.1)GO TO 900
      IF (N.NE.1) CALL NEWPAGE
      CALL PLOT(0.3,0.3,-3)
      IF(N.EQ.1) CALL PLOT(-1.5,-1.0,-3)
      CALL POINT(0.3,0.1)
      CALL CHECK(0.3,0.1,+2)
      CALL SYMBOL(-5.1,-5.5,.5,18HR-THETA PROJECTION,0.0,18)
C
C
      CALL PLOT(-5.0,0.0,-3)
      CALL NUMBER(0.3,0.3,0.3,12HB13826-0/Z00,0.0,12)
      CALL SYMBOL(1.0,0.3,0.3,12HB,0.0,1)
      CALL SYMBOL(0.3,0.3,0.3,4HI = ,0.0,4)
      CALL NUMBER(0.3,0.3,0.3,XY=Y60,0.0,3)
C
C
      DO2=1.0E-3*I
      CALL NUMBER(2.3,3.5,0.5,DZ,0.0,3)
      CALL NUMBER(2.3,7.3,0.3,DO2,0.0,2)
      CALL NUMBER(2.3,6.3,0.3,OMEGA,0.0,-1)
C
C
      CALL NUMBER(7.0,1.5,0.5,14H817B2SOL 60,0.0,11)
      CALL NUMBER(7.0,1.2,0.3,3HSK=,0.0,3)
      CALL NUMBER(7.0,5.5,0.5,15H82SED 4-87-18),0.0,13)
      CALL PLOT(5.3,0.0,-3)
C
C     AXIS SET
C
      CALL INTENSE(10)
      CALL AXIS(0.0,0.0,6HR AXIS,6,5.0,0.0,0.0,1.0)
      CALL AXIS(0.5,-4.0,6HZ AXIS,6,14.0,90.0,-1.0,1.0)
      CALL AXIS(0.5,5.0,5HR AXIS,6,5.0,0.0,0.0,1.0)
      CALL INTENSE(15)
C
C
C     SET INITIAL PLOTTING COORDINATES
C
C
      CALL SYMBOL(7.3,-5.5,0.5,19HR-Z PROJECTION,0.0,14)
  900 CONTINUE
C
C
      XPOINT=10.0+Y(1)*COS(Y(2))
      YPOINT=10.0+Y(1)*SIN(Y(2))
      CALL PLOT(XPOINT,YPOINT,3)
      X=10.0+Y(1)*COS(Y(2))+0.5
      Y=7.0+10.0*Y(3)
C
C
C     WRITE INITIAL CONDITIONS AND
C     HEADINGS
C
      WRITE(6,778) OMEGA,DZ,I
  778 FORMAT(4X,*OMEGA=  *,E12.3,3X,*DZ= *,E12.3,
     1  4X,*I= *,E12.3)
C
      WRITE(6,776)
      WRITE(6,777) XLAST,4,YLAST
  777 FORMAT(8E14.3)
  776 FORMAT(4X,*TIME*,4X,*ERROR*,4X,*RADIUS*,4X,*THETA*,4X,
     1  *VR*,5X,*VTHETA*,6X,*VZ*)
      RETURN
      END
C
C
```

```
      SUBROUTINE MOND(X,H,Y,ITIME,NWRL)
      DIMENSION Y(6)
C
C     PLOTTING IS DONE HERE
C
      COMMON R,Z
      IF(NWRI.EQ.1) ITIME=ITIME+1
      XPOINT=1000.*(Y(1)*COS(Y(3))
      YPOINT=1000.*(Y(1)*SIN(Y(3))
      CALL PLOT(XPOINT,YPOINT,2)
      CALL PLOT(R,Z,3)
      R=1000.*(Y(1)*COS(Y(2))+3.5
      Z=1000.*Y(3)
      IF(Z.GT.10.0) Z=Z-7.0
      IF(Z.LT.-10.0) Z=Z+7.0
      IF(Z.GT.4.0) Z=Z-14.0
      IF(Z.LT.-11.0) Z=Z+14.0
      IF(Z.GT.24.0) Z=Z-21.0
      IF(Z.LT.-18.0) Z=Z+21.0
      CALL PLOT(R,Z,2)
      CALL PLOT(XPOINT,YPOINT,3)
      IF(NWRI.EQ.1) NWRI=1(3,775) X,H,Y
  775 FORMAT(3E10.3)
      RETURN
      END
C
C
C
C
C
C
C
      SUBROUTINE RHS(X,Y,DER)
      REAL MASS
      DIMENSION E(3),B(3)
      DIMENSION Y(6),DER(6)
      DATA Q,MASS/1.6E-19,66.32E-27/
C
C     C
C     C   CALCULATES RIGHT HAND SIDE OF Y'=F(X,Y)
C     C   FOR A PARTICLE SUBJECT TO ELECTRIC AND MAGNETIC
C     C   FIELDS, USING CYLINDRICAL POLAR COORDINATES.
C     C
C
      ZR=3.1
      RHOM=ZR*Q/MASS
      DER(4)=Y(4)
      IF(Y(1).NE.0.0) DER(2)=Y(5)/Y(1)
      DER(3)=Y(6)
      CALL BFIELD(X,Y,B)
      CALL EFIELD(X,Y,E)
C
C
      DER(4)=RHOM*(E(1)+Y(5)*B(3)-Y(6)*B(2))
     1    +Y(5)*Y(5)/Y(1)
      DER(5)=RHOM*(E(2)+Y(6)*B(1)-Y(4)*B(3))
     1    -Y(4)*Y(5)/Y(1)
      DER(6)=RHOM*(E(3)+Y(4)*B(2)-Y(5)*B(1))
      IF(Y(1).EQ.0.0) DER(2)=DER(5)/DER(1)
      RETURN
      END
C
C
C
C
C
C
C
      SUBROUTINE BFIELD(X,Y,B)
      DIMENSION Y(6),B(3),XQ(12),YQ(12)
      COMMON /FIELD/ OMEGA,BZ,I
      REAL I
C
C     C
C     C   CALCULATES THE MAGNETIC FIELD PRODUCED BY
C     C   A SET OF SIX PARALLEL AND INFINITE CURRENT
C     C   CARRYING RODS, PARALLEL TO THE Z AXIS,LOCATED
C     C   ON THE VERTICES OF A HEXAGON WITH CURRENTS OF
C     C   THE SAME MAGNITUDE AND FLOWING IN OPPOSITE
C     C   WAYS IN NEIGHBOURING RODS.
C
```

```
C
C
      PIO3=3.1416/6.0
      ITER=0
      DO=1.0E-7*I
C
CC
C
      B(1)=0.0
      B(2)=0.5
      B(3)=0.2*SIN(OMEGA*X)
C
CC
C
      SIGMU=1.0
      STHETA=SIN(Y(2))
      CTHETA=COS(Y(2))
      XCOORD=Y(1)*STHETA
      YCOORD=Y(1)*CTHETA
      DO 111 J=1,12
      XJ(J)=A*COS(FLOAT(J)*PIO3)
      YJ(J)=A*SIN(FLOAT(J)*PIO3)
      RSQ=((XJ(J)-XCOORD)**2+(YJ(J)-YCOORD)**2)
     1   +(YJ(J)-YCOORD)**2)
      SQR=RSQ**1.5
C
CC
C
      SIGNO=-SIGNO
      B(1)=B(1)+SIGNU*SIGNO*(XJ(J)*STHETA
     1     -Y(J)*CTHETA)
      B(2)=B(2)+SIGNO*SIGNO*((XJ(J)-XCOORD)*
     1   CTHETA+(YJ(J)-YCOORD)*STHETA)
  111 CONTINUE
      RETURN
      END
C
C
C
C
C
C
      SUBROUTINE EFIELD(X,Y,E)
      DIMENSION Y(6),E(3)
      COMMON /FIELD/ OMEGA,BZ,I
      REAL I
C
CCCCC
CCCCC CALCULATES THE ELECTRIC FIELD INDUCED INSIDE
CCCCC AN INFINITELY LONG SOLENOID.  Y(1) IS R
CCCCC Y(2) IS THETA, Y(3) IS Z
CCCCC
C
      RH=Y(1)*0.5
      EMAX=OMEGA*RH*BZ
C
C
      E(1)=0.0
      E(2)=-EMAX*COS(OMEGA*X)
      E(3)=0.0
      RETURN
      END
C
C
C
      SUBROUTINE MERSON (X,Y,H,N,DER,AK)
      DIMENSION Y(N),DER(N),AK(5,N),YSUB(6)
      X=X+H+H
      DO 1 I=1,N
      AK(1,I)=H*DER(I)
    1 YSUB(I)=Y(I)+AK(1,I)+AK(1,I)
      CALL EVAL(X,YSUB,DER)
      DO 2 I=1,N
    2 AK(2,I)=H*DER(I)
```

```
      2       YSUB(I)=Y(I)+ AK(1,I)*AK(2,I)
              CALL FUN(X,YSUB,DER)
              X=X+H
              DO 3 I=1,N
              AK(3,I)=      H*DER(I)
      3       YSUB(I)=Y(I)+.75*AK(1,I)+2.25*AK(3,I)
              CALL FUN(X,YSUB,DER)
              X=X+1+H+H
              DO 4 I=1,N
              AK(4,I)=H*DER(I)
      4       YSUB(I)=Y(I)+1*AK(1,I)+AK(1,I)-9.*AK(3,I)+12.*AK(4,I)
              CALL FUN(X,YSUB,DER)
              DO 5 I=1,N
              AK(5,I)=H*DER(I)
      5       Y(I)=Y(I)+AK(1,I)+4.*AK(4,I)+AK(5,I)
              CALL FUN(X,YSUB,DER)
              RETURN
              END


              SUBROUTINE CHECK(H,AK,ERROR,ERL,L)
              DIMENSION AK(5,6),Y(6)
              LOGICAL L
              I3=0
              DO 2 I=1,6
              AB=.2*ABS(AK(1,I)+AK(1,I)+4K(4,I)*3.-9.*AK(3,I)-AK(5,I))
              IF(I.GT.3) AB=11/2.E-7
              IF(I.EQ.2) AB=.01*AB
              IF(AB.LT.ERROR) GO TO 2
              H=H/2.
              L=.FALSE.
              RETURN
      2       IF(AB.LT.ERL) I3=I3+1
              IF(I3.LT.6) RETURN
              H=H+1
              RETURN
              END
```

APPENDIX B: Listing of program used to calculate plasma displacement.

```
      PROGRAM DATA(INPUT,OUTPUT,TAPE5=INPUT,TAPE6=OUTPUT)
      DIMENSION Y(4),Y2(4)
      COMMON/VERT/ BV
      COMMON /B/ BO,RP
      COMMON /C/ CN(40)
      COMMON /V/ VT(40)
      DATA M,CN/15,0.,3.6,5.,6.,7.2,7.7,8.1,7.9
     1 ,7.2,6.2,5.4,4.3,3.6,2.9,2.4/
      DATA VT/0,.5,1.,1.58,2.21,3.62,5.32,
     1 5.59,5.12,3.07,4.61,4.,3.,2.,1./
9     CONTINUE
      WRITE(6,12)
12    FORMAT(*CURRENT,VELOC*)
      DO 1 I=1,40
      N=I
      READ(5,*) CN(I),VT(I)
      IF(EOF(5)) 2,1
1     CONTINUE
2     WRITE(6,13)
      READ(5,*) RO
      ILOOP=1
13    FORMAT(*INITIAL POS*)
      WRITE(6,15)
15    FORMAT(*PLASMA RAD*)
      READ(5,*) RP
      WRITE(6,10)
10    FORMAT(*CUSP*)
      READ(5,*) BO
      BO=BO*BO
      WRITE(6,11)
11    FORMAT(*VERT*)
      READ(5,*) BV
      DO 6 J=M,40
      CN(J)=0.0
      VT(J)=0.0
6     CONTINUE
      KK=-1
      DO 3 J=1,4
      Y(J)=RO
      Y2(J)=0.0
3     CONTINUE
      Y2(4)=RHS(RO,0.)
      H=0.1E-7
      X=0.0
      ERR=1.0E-5
      DO 4 I=1,1000
      CALL MILNE(X,Y,Y2,H,ERR,ILOOP)
      IF(ILOOP.EQ.0) GO TO 5
      K=2.E6*X
      IF(K.NE.KK) WRITE(6,21) 100.*Y(4),1.E6*X
21    FORMAT(2F8.2)
      KK=K
      IF(X.GT.6.5E-6) GO TO 5
      X=X+H
4     CONTINUE
5     CONTINUE
      WRITE(6,14)
14    FORMAT(*AGAIN*)
      READ(5,20) A
20    FORMAT(A10)
      IF(EOF(5)) 7,8
8     IF(A.EQ.1HN) GO TO 9
      IF(A.NE.1HN) GO TO 2
7     CONTINUE
```

```
      STOP
       END
C
C
C
C
      SUBROUTINE MILNE(X,Y,Y2,H,ERR,ILOOP)
      DIMENSION Y(4),Y2(4)
      IS=0
 2    CONTINUE
      IS=IS+1
      H2=H*H
      HP=4.*H2/3.
      HC=H2/12.
      YP=2.0*Y(3)-Y(1)+HP*(Y2(3)+Y2(2)+Y2(1))
      Y2P=RHS(YP,X+H)
      YC=2.0*Y(4)-Y(3)+HC*(Y2P+10.0*Y2(4)+Y2(3))
      YT=ABS(YP-YC)
      IF(YT.LT.ERR) GO TO 3
      H=H/2.0
      IF(IS.GT.20) GO TO 40
      GO TO 2
 3    CONTINUE
      Y(1)=Y(2)
      Y(2)=Y(3)
      Y(3)=Y(4)
      Y(4)=YC
      Y2(1)=Y2(2)
      Y2(2)=Y2(3)
      Y2(3)=Y2(4)
      Y2(4)=RHS(YC,X+H)
 40   IF(IS.GT.20) ILOOP=0
      RETURN
      END
C
C
C
C
      REAL FUNCTION IO(X)
      DIMENSION COE(7)
      DATA COE/1.,3.5156229,3.0899424,1.2067492,
     1    .2659732,.0360768,.0045813/
      DATA CA /70.86614173/
      T=CA*X/3.75
      T2=T*T
      IO=0.0
      T1=1.0
      DO 1 I=1,7
      IO=IO+T1*COE(I)
      T1=T1*T2
 1    CONTINUE
      RETURN
      END
C
C
C
C
      FUNCTION RHS(R,T)
      COMMON /B/ BO,RP
      REAL MASS,IO
      MASS=4.E20*1.6726E-27*40.*3.1416*RP*RP
      CUR=CURR(T)
      VPH=VPHI(T)
      RS=R-.248
```

```
      RS1=RS+RP
      RS2=RS-RP
      BE1=IO(RS1)
      BE2=IO(RS2)
      CUSP=1777.77*RP*BO*(BE2*BE2-BE1*BE1)
      SELF=1.0E-7/R*(ALOG(800.*R)-0.75)*CUR*CUR
      VERT=-BZ(R,T)*CUR
      CENT=VPH*VPH/R
      RHS=(SELF+VERT+CUSP)/MASS
     1    +CENT
      RETURN
      END
C
C
C
C
      FUNCTION CURR(T)
      COMMON /C/ CN(40)
      J=INT(2.E6*T)
      P=2.E6*(T-FLOAT(J)*.5E-6)-1.0
      CURR=1.E3*(.5*P*(P-1.)*CN(J+1)+(1.-P*P)*CN(J+2)
     1   +.5*P*(P+1.)*CN(J+3))
      RETURN
      END
C
C
C
C
      FUNCTION BZ(R,T)
      DATA OMEGA/1.9039955E5/
      COMMON /VERT/ BV
      BZ=BV*(.0225+.0083*EXP(-150.*R))*
     1     SIN(OMEGA*T)*4.44444E-3
      RETURN
      END
C
C
C
C
      FUNCTION VPHI(T)
      COMMON /V/ VT(40)
      J=INT(2.E6*T)
      P=2.E6*(T-FLOAT(J)*.5E-6)-1.0
      VPHI=1.E4*(.5*P*(P-1.)*VT(J+1)+(1.-P*P)*VT(J+2)
     1    +.5*P*(P+1.)*VT(J+3))
      RETURN
      END
```

ACKNOWLEDGEMENTS

It is a great pleasure to express my gratitude for the assistance of the individuals and institutions which made this work possible. Amongst the many I am indebted to, I would like to mention:

Professor M.G. Haines, the originator of the Polytron idea and my supervisor.

Mr A.E. Dangor, for help, guidance and invaluable comments.

Dr J.D. Kilkenny, for useful comments.

Dr A. Folkierski, particularly for careful revision of the manuscript.

Messrs P. Choi, A.K.L. Dymoke-Bradshaw and P. Slade, for the development of the computer program used to generate some of the graphs presented in this thesis.

Messrs J. Westlake and A. Cobley, for technical assistance.

Mr N.D. Jackson and Mrs B. Bolt of the Photographic Department, Blackett Laboratory, for help with photographic work.

The staff of the Mechanical and Glass Blowing workshops, for technical assistance.

Miss F. Mawer, for the typing of the manuscript, and especially her patience.

Universidad de Chile, Santiago, Chile and the British Council, for financial support during the first part of this work.

Imperial College, for financial support during the latter part of this work.

Culham Laboratories, for the loan of the STL image converter camera.

The Applied Optics group, Blackett Laboratory, for the loan of the "Imacon" image converter camera.

Lastly, and by no means least, to Ana Maria, my wife, for her help, support, encouragement and understanding, without which this work would not have been possible.

REFERENCES

Andrews, J.G. and Allen, J.E., Proc. Roy. Soc. Lond. A320 (1971), 459.

Bakulin, E.A., Stepin, E.V. and Shcherbinina, V.V., Sov. Phys. Tech. Phys. 14 (1969), 77.

Berezin, A.B., Zaidel', A.N., Malysher, G.M., Sov. Phys, Tech. Phys. 8 (1963), 213.

Berkowitz, J., Grad., M., Rubin, H., in Peaceful Uses of Atomic Energy (Proc. 2nd Int. Conf. Geneva, 1958), UN, New York, 31 (1958), 177.

Bobeldijk, C., Hoekzema, J.A., Mimura, M., Oepts, D. and Oomens, A.A.M., Nuclear Fusion Supplement, Vol I (1977), 493.

Bohm, D., Burhop and Massey, in The Characteristics of Electrical Discharges in Magnetic Fields (A. Guthrie and R.K. Wakeling, Eds.) McGraw Hill (1949).

Boozer, A.H., Levine, M.A., Phys. Rev. Lett. 31 (1973), 1287.

Born, M., and Wolf, E., Principles of Optics, Fourth Edition, Pergamon Press (1970).

Braginskii, S.I., in Reviews of Plasma Physics, Vol I (M.A. Leontovich, Ed.) Consultants Bureau (1965).

Brown, M.G., private communication (1978).

Buneman, O., Phys. Rev. 115 (1959), 503.

Buneman, O., Plasma Physics 4 (1962), 270.

Carlqvist, P. and Jacobsen, C., Icarus 3 (1964), 270.

Chen, F.F., in Plasma Diagnostic Techniques (Huddlestone and Leonard, Eds.) Academic Press (1965).

Coensgen, F.H., Cummins, W.F., Gormezano, C., Logan, B.G., Molvik, A.W., Nexsen, W.E., Simonen, T.C., Stallard, B.W. and Turner, W.C., Phys. Rev. Letters 37 (1976), 143.

Cole, H.C., PhD Thesis, London University (1970).

Dangor, A.E., Parkinson, G.J., Dunnett, R.M., Haines, M.G. and Latham, R., Conf. on Plasma Physics and Controlled Nuclear Fusion, 1968 (IAEA, Vienna, 1969) Vol I, 255.

Dreicer, H., Phys. Rev. 115 (1959), 238.

Dunnett, R.M., PhD Thesis, London University (1968).

Durand, E., Magnetostatique, Masson et Cie. (1968).

Evans., D.E., Katzenstein, J., Rep. Prog. Phys. 32 (1969), 207.

Fainberg, Ya. B., J. Nucl. Energy, Pt.C, 4 (1962), 203.

Furth, H.D., Nuclear Fusion 15 (1975).

Gallagher, C.C., Combes, L.S., Levine, M.A., Phys. Fluids 13 (1970), 1617.

Gary, S.P., J. Plasma Phys. 6 (1971), 262.

Gierke, G.V., Hofmann, F.W., Lotz, W., Rav, F., Remy, E., Wobig, H. and Wolf, G.H., Conf. on Plasma Physics and Controlled Nuclear Fusion Research, Vienna, 1966, Vol I, 331.

Griem, H.R., Plasma Spectroscopy, McGraw Hill (1964).

Haines, M.G., Conf. on Plasma Physics and Controlled Nuclear Fusion Research, Salzburg, 1961 , p 1162 (abstract only).

Haines, M.G., Imperial College Internal Report (1962).

Haines, M.G., 6th Int. Conf. on Ionization Phenomena in Gases, Paris 1963, 4, 477.

Haines, M.G., Phys. Letters (1963), 313.

Haines, M.G., Nuclear Fusion 17 (1977), 811.

Hamberger, S.M. and Jancarik, J., Phys. Rev. Lett. 25 (1970), 999.

Humphries, S., 2nd Int. Conf. on High Energy Ion and Electron Beams, Cornell, 1977.

Junker, J. and Lotz, W., Z. Physik 238 (1970), 148.

Kaye, G.W.C., Laby, T.H., Tables of Physical and Chemical Constants, Longmans (1956).

Kilkenny, J.D., PhD Thesis, London University (1972).

Kilkenny, J.D., Dangor, A.E. and Haines, M.G., Plasma Phys. 15 (1973), 1197.

Kilkenny, J.D., J. Plasma Phys. 15 (1976), 253.

Krall, N.A. and Liewer, P.C., University of Maryland Technical Report, 71-106 (1971).

Kulsrud, R.M., Yung-Chiun Sun, Winsor, N.K. and Fallon, H.A., Phys, Rev. Lett. 31 (1973), 690.

Lance, G.N., Numerical Methods for High Speed Computers, Illife (1961).

Leontovich, M.A., 1951, published in Plasma Physics and the Problem of Controlled Thermonuclear Reactions, Vol I (M.A. Leontovich, Ed.) Pergamon Press (1961).

Levine, M.A., Boozer, A.H., Kalman, G. and Bakshi, P., Phys. Rev. Lett. 28 (1972), 1323.

Lomas, P., PhD Thesis, London University (1975).

Milne, W.E., J. Res. Nat. Bur. Stand., Wash., 43 (1949), 537.

Miyamoto, K., Nuclear Fusion 18 (1978), 243.

Monro, D.M., ICCC Bulletin 4.8/2 (1977)

Morozov, A.I., 1968

Morozov, A.I., Kislov, A.Ya. and Zubkov, I.P., CTO/516 (1969).

Parkinson, G.J., PhD Thesis, London University (1968).

Post, R.F., Int. Conf. on Nuclear Fusion Reactors, Culham (1969).

Reynolds, P., Millward, P. and Hunt, P.R., Conf. on Plasma Physics and Controlled Nuclear Fusion Research, Tokyo, 1974.

Rostoker, N., 2nd Int. Conf. on High Energy Ion and Electron Beams, Cornell, 1977.

Seidl, M. and Sunka, P., Nuclear Fusion 7 (1967), 237.

Smythe, W.R., Static and Dynamic Electricity, McGraw Hill (1950).

Spitzer, L., Physics of Fully Ionized Gases, 2nd Edition, Interscience (1967).

Trubnikov, B.A. and Bazhanova, A.E., in Plasma Physics and the Problem of Controlled Thermonuclear Reactions, Vol III (M.A. Leontovich Ed.) Pergamon Press (1959).

Watkins, M.L., PhD Thesis, London University (1974).

From the Eighth European Conference on Controlled Fusion and Plasma Physics, Prague, 1977

PLASMA DRIFTS IN THE POLYTRON

H. Chuaqui

Blackett Laboratory, Imperial College, London SW7 2BZ

Abstract: The outward toroidal drift in the Polytron has been suppressed by the addition of a vertical magnetic field, none the less vertical drifts are present which prevent further Hall acceleration.

Previous results (1) have shown that the plasma column in the Polytron has a toroidal outward drift. The addition of a vertical field prevents this drift. Nonetheless, a decrease in the reaction force on the cusp coils and toroidal velocities is observed, probably due to a vertical shift of the plasma.

The Polytron is a toroidal Hall accelerator with 36 cusps. A schematic of the apparatus is shown in Figure 1. The accelerating electric field is provided by discharging a capacitor bank through a set of induction rods. This set of rods also provides the vertical magnetic field which prevents the radial outward toroidal drift (2). Ions are preferentially accelerated as the ion Larmor radius is larger than the cusp separation (for argon is the present device), where electron Larmor radius is small, except near the cusp magnetic axis where they can flow freely. Off axis the electrons are tied to the magnetic field lines. For perfect conductivity, the magnetic field lines are effectively equipotentials. Thus, the electric field can exist only in the ring cusp region. (3)

The radial and vertical motion of the plasma in the minor cross section have been investigated by measurements of the distribution of line emission from AII, AIII, and AIV and by external magnetic probes. The line emission measurements show a well defined narrow channel (1.cm diameter) that stays centered on the major radius, but show a vertical drift of up to 8mm at late times. Figure 2 is a typical plot of plasma position with respect to time. Within the margin of experimental accuracy the vertical shift does not seem to depend on the direction of either the toroidal electric field or cusp magnetic field. Also shown in the figure is the reaction force on the cusp coil. From these measurements the decrease of the reaction force on the cusp coils seems to be associated with the vertical shift, presumably due to the fact that the Hall currents in the ring cusp can no longer close.

Figure 3 shows the ion toroidal velocity as a function of time. The ion velocity measurement was obtained by a differential Doppler shift method (2). Note that the ion velocity changes only after the reaction force begins to decrease. At this time there appears to be a reduction in the ion number density on axis, as inferred from the AIII and AIV line emission, shown in Figure 3. This seems to be consistent with the vertical drift shown in Figure 2.

Line profile measurements show that there is a Doppler broadening which is larger near the ring cusp region than at the point cusps. This indicates that the broadening is not wholly thermal, but that there is a large contribution due to directed ion motion in the ring cusp region, in agreement with particle trajectory calculations (4).

Loss of particles through the ring cusp and thickness of the loss region have been investigated by a faraday cup probe positioned near the wall. These measurements show that after an initial loss (1.5 to 3 μs) there is little further loss. The loss width is between 3 and 8 mm, which is between an electron and ion Larmor radii and is consistent with resistive sheath calculations (3).

The measurements indicate that the radial outward motion has been suppressed by a vertical magnetic field. However, there is a vertical shift which limits further Hall acceleration. The observed shifts are comparable with the radius of the plasma. column.

References:

1. Kilkenny, J.D., Dangor, A.E., Haines, M.G., Plasma Physics, 15, pp 1197-1220 (1973)
2. Chuaqui, H., Ph.D Thesis, London University (to be submitted)
3. Kilkenny, J.D., Proc. 5th Conf. on Controlled Fusion and Plasma Physics, Grenoble, 1, 101, (1972)
4. Kilkenny, J.D., (1972) PhD. Thesis, London University

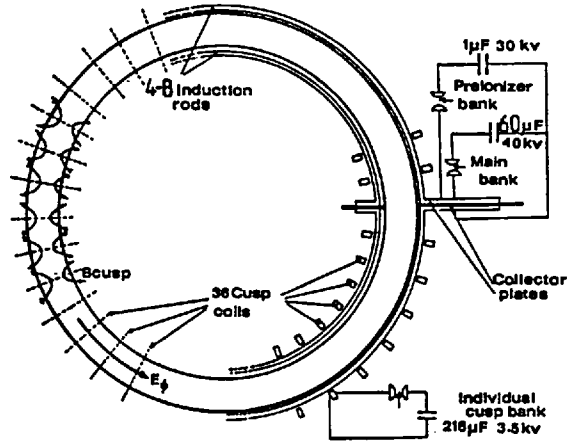

FIGURE 1. SCHEMATIC OF THE POLYTRON

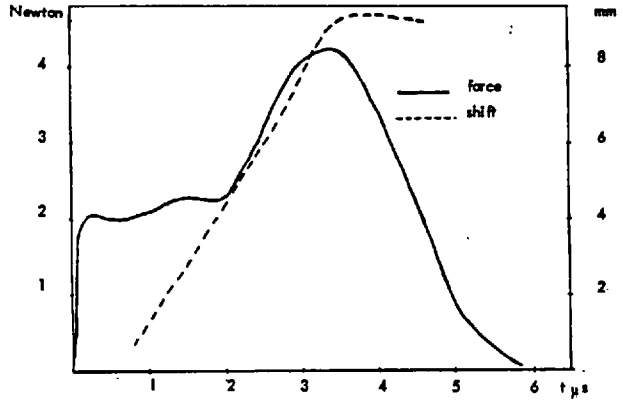

FIGURE 2. REACTION FORCE ON COIL AND VERTICAL SHIFT FROM INITIAL POSITION

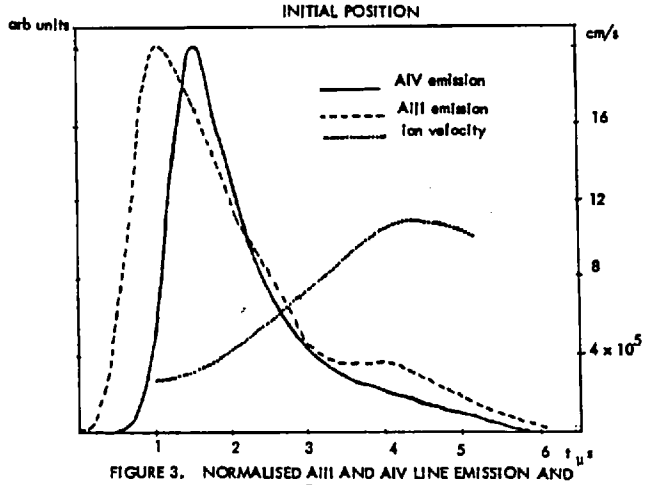

FIGURE 3. NORMALISED AIII AND AIV LINE EMISSION AND ION VELOCITY